ΠΟΛΥΤΕΧΝΕΙΟ ΚΡΗΤΗΣ
TECHNICAL UNIVERSITY OF CRETE

School of Mineral Resources Engineering

BSc Thesis

Exploring the potential of Hospital Medical Waste Incinerator (HMWI) bottom ash (BASH) as a promising raw material for the production of autoclaved bricks

Konstantina Maria Bekiari

Examination committee

Dr. Platon N. Gamaletsos, Assistant Professor, School of Mineral Resources Engineering (SMRE), Technical University of Crete (TUC), Chania, Greece (supervisor)

Dr. Yiannis Pontikes, Associate Professor, Department of Materials Engineering (MTM), Sustainable Materials Processing and Recycling (SeMPeR), KU Leuven (Belgium)

Dr. Evangelos Petrakis, Assistant Professor, School of Mineral Resources Engineering (SMRE), Technical University of Crete (TUC), Chania, Greece

Chania, 2025

Prologue

This thesis delves into a critical environmental challenge faced by developed nations. The improper disposal of a hazardous material, such as the bottom ash (BASH) derived from hospital and/or medical waste incinerators (HMWI), may pose significant risks to soil and groundwater quality, ultimately threatening public health. In response to this pressing issue, researchers around the globe tried to solidify and stabilize such hazardous waste during the past. To the best to our knowledge, it is the first time in the literature that a sustainable valorization of HMWI BASH is being proposed herein. To meet this need, Hospital Medical Waste Incineration (HMWI) Bottom Ash (BASH) from the Hospital Medical Waste Incineration Plant / HMWIP (a.k.a. "APOTEFROTIRAS S.A.") operated by the joint venture HELECTOR S.A. – ARSI S.A. (ELLACTOR Group) has been utilized, applying innovating recipes for such hazardous material, in order to transform it into a non-hazardous building material. The owner of the entire project is the Association of Communities and Municipalities in the Attica Region (ACMAR) in Attica, Greece (a.k.a. Special Inter-Collective Association of the Prefecture of Attica / "EDSNA"). The present study focuses on the potential of utilizing HMWI BASH toward to the production of pressed autoclaved bricks, offering a sustainable solution to mitigate environmental hazards. Through a mineralogical and chemical analysis of the studied HMWI BASH, and rigorous testing of the resulting bricks' mechanical and leaching properties, this diploma thesis is an attempt to provide novel insights that could lead to the development of sustainable construction materials.

The experimental part of the present work was partially at the school of Mineral Resources Engineering / SMRE (Technical University of Crete / TUC, Crete Island, Greece), and at the Department of Materials Engineering / MTM (KU Leuven, Belgium) under the guidance of Assoc. Prof. Dr. Yiannis Pontikes. It is important to mention that Ms. Konstantina Maria Bekiari (SMRE/TUC) has been benefited by the Erasmus+ traineeship program of the European Union in order to visit MTM of KU Leuven (KUL). During her stay at MTM she conducted experiments and valorized the HMWI BASH samples under the assistance of Mr. Nikolaos Athanasakis (PhD student, MTM, KU Leuven). Especially, for the Laser Ablation Inductively Coupled Plasma Mass Spectrometry (LA-ICP-MS) analytical measurements Konstantina established a collaboration with the Institute for Mineralogy of the Westfälische Wilhelms-

Universität Münster (University of Münster, Münster, Germany) under the guidance of Prof. Dr. Stephan Klemme and assistance by Prof. Dr. Jasper Berndt, co-coordinated by Assoc. Prof. Dr. Ioannis Baziotis (Agricultural University of Athens / AUA, Athens, Greece). The present diploma thesis was designed and supervised by Asst. Prof. Dr. Platon N. Gamaletsos (SMRE/TUC).

Acknowledgments

First and foremost, I am grateful to Asst. Prof. Dr. Platon N. Gamaletsos (SMRE/TUC) who mentored me during my undergraduate studies, encouraging to study the HMWI BASH material in respect to its sustainable valorization, and, especially, for his valuable guidance during the present diploma thesis. “HELECTOR S.A.” member of ELLACTOR Group and its subordinate “APOTEFROTIRAS S.A.” are acknowledged for supplying the HMWI BASH samples from the “APOTEFROTIRAS S.A.”. Many thanks are due to Mr. Nikolaos Kothris (“APOTEFROTIRAS S.A.”) as well as to Mr. George Arvanitis (Deputy Head of the EDSNA Heat Treatment Division) for the collaboration and sample provision.

I want to express my sincere gratitude to Assoc. Prof. Dr. Yiannis Pontikes for accepting me in his research group “Sustainable Materials Processing and Recycling / SeMPeR” and for giving me the great opportunity to work and collaborating with his group at the MTM of the KU Leuven (Belgium), under the frame of the Erasmus+ traineeship program of the EU, and, accordingly, for his participation in the examination committee of my BSc Thesis. Moreover, I do thank Asst. Prof. Dr. Evangelos Petrakis (SMRE/TUC) for his assistance during mineral processing and his participation in the examination committee. Many thanks for allowing LA-ICP-MS measurements at the Institute for Mineralogy of the University of Münster (Germany) to Prof. Dr. Stephan Klemme, Prof. Dr. Jasper Berndt and Assoc. Prof. Dr. Ioannis Baziotis (AUA, Greece). Moreover, I would like to express my appreciation to Asst. Prof. Dr. Emmanouil Varouchakis for sharing his thoughts about the statistical evaluation of the chemical analysis. Finally, Mr. Nikolaos Athanasakis (MTM, KU Leuven) is gratefully acknowledged for his patience and feedback as well as for his valuable assistance and support during the experimental procedure carried out at KU Leuven.

Finally, this thesis is fully dedicated to my family. I do want to express my deepest appreciation to my beloved parents for encouraging me and their support throughout my undergraduate studies.

Abstract

In developed countries, the abandonment and uncontrolled disposal of bottom ash from hazardous medical and other (bio)-waste incinerators are the major cause of soil and groundwater contamination, which can endanger both the environment and public health. The present diploma thesis provides a detailed characterization and novel insights into the valorization of Hospital Medical Waste Incineration Bottom Ash (HMWI BASH) towards the production of pressed autoclaved bricks (a.k.a. “dense monoliths”). The HMWI BASH was provided by Hospital Medical Waste Incineration Plant / HMWIP (a.k.a. “APOTEFROTIRAS S.A.”) operated by the joint venture HELECTOR S.A. – ARSI S.A. (ELLACTOR Group). “APOTEFROTIRAS S.A.” is located near Athens, Greece. The raw material received by the incineration facility was classified into seven (7) granulometric fractions (i.e., +8mm, -8+4mm, -4+2mm, -2+1mm, -1+0.500mm, -0.500+0.250mm and -0.250mm) and characterized separately to identify mineralogical and chemical variations among the fractions which may affect their valorization potential.

Powder X-ray diffraction data (PXRD) of the HMWI BASH raw sample and its individual fractions revealed a high amorphous content, especially in the raw one and its coarser fractions, gradually decreasing towards the finer fractions. The raw sample and its fractions consisted of high temperature crystalline phases, namely gehlenite ($Ca_2Al(AlSi)O_7$), perovskite ($CaTiO_3$) and cristobalite (SiO_2), encapsulated by the amorphous matrix. Bulk chemical analysis by means of wavelength dispersive X-ray fluorescence (WD-XRF) along with inductively coupled plasma optical emission spectroscopy (ICP-OES) and Laser Ablation Inductively Coupled Plasma Mass Spectrometry (LA-ICP-MS) showed that the studied samples contain a variety of heavy metals and metalloids, some of them being present at relatively higher concentrations (e.g., Cr, Ni, Cu, etc.), and others accumulated in smaller quantities (e.g., Co, Sn, V, As, etc.). Lead is present in all the studied samples (~3-9 ppm), while cadmium has been detected in some of the fraction (~1-3 ppm) by LA-ICP-MS. As it has been revealed by ICP-OES, it is noteworthy to mention the presence of gold (Au) in the studied raw material (15 ppm). It seems that gold is preferably accumulated in the coarser fraction (13 ppm) and less in the finest ones (8-10 ppm). Besides, rare earth elements (including 15 lanthanides, Sc and Y) content was found to be significantly increased in the finer fractions. The SEM-EDS observations revealed the presence of various metals-containing (sub)-micro-sized particles -

also containing heavy metals such as Cr and Cu- embedded in a Si-Na-containing amorphous matrix, such as Ca-Ti-oxides (perovskites according to PXRD), etc.

For the production of the pressed autoclaved bricks, the HMWI BASH material was used in its initial form (i.e., HMWI BASH raw sample), along with a 1:1 mixture of its -0.500+0.250mm and -0.250mm fractions, due to their lower amorphous and higher gehlenite content resulting in six different formulations, for comparison. Three mix designs were employed for the production of the bricks. The mix designs incorporated the aforementioned two HMWI BASH samples (IP100 mix design), the metakaolin MK (IP_MK mix design) and an ordinary Portland cement OPC (BLD mix design). Different dense monoliths were produced from each formulation. All the dense monoliths were cured for 24 hours under the same hydrothermal conditions in an autoclave. The produced autoclaved bricks were subjected to mineralogical investigation, compressive strength test assessment, and finally were undergone leaching process according to the EN 12457/2 standard. The mechanical performance and leaching properties of the bricks containing the HMWI BASH raw sample, were superior to the mixture of finer fractions, making the sieving process unnecessary for this application. The addition of metakaolin proved detrimental to the strength of the bricks. Among the six formulations used in the thesis, the IP-based bricks, being produced using the HMWI BASH raw sample, are more preferable. The IP-100-based dense monoliths were found to contain Sb and As both exceeding the EN 12457/2 limits by 14% and 15%, respectively. In contrast, the BLD-based bricks showed the best performance in immobilizing potentially toxic elements as the amount of heavy metals and metalloids is ranged within the EN 12457/2 limits. The latter might be attributed to the solidification facilitated by the OPC.

Περίληψη

Στις ανεπτυγμένες χώρες, η εγκατάλειψη και η ανεξέλεγκτη διάθεση της τέφρας πυθμένα από τους αποτεφρωτήρες επικίνδυνων ιατρικών, νοσοκομειακών και άλλων βιο-αποβλήτων θεωρείται μία εκ των κύριων αιτιών μόλυνσης του εδάφους και των υπόγειων υδάτων, η οποία μπορεί να θέσει σε κίνδυνο τόσο το περιβάλλον όσο και τη δημόσια υγεία. Η παρούσα διπλωματική εργασία παρέχει νέες γνώσεις σχετικά με το χαρακτηρισμό και τις δυνατότητες αξιοποίησης της τέφρας πυθμένα αποτέφρωσης νοσοκομειακών ιατρικών αποβλήτων (Hospital Medical Waste Incinerator bottom ash / HMWI BASH) προς την κατεύθυνση της παραγωγής πρεσαριστών αυτοκλείστων τούβλων (γνωστά και ως “πυκνοί μονόλιθοι” / “dense monoliths”). Η τέφρα παραχωρήθηκε από το εργοστάσιο αποτέφρωσης επικίνδυνων ιατρικών αποβλήτων (γνωστό και ως “ΑΠΟΤΕΦΡΩΤΗΡΑΣ Α.Ε.”) που διαχειρίζεται η κοινοπραξία (Κ/Ξ) μίσθωσης αποτεφρωτήρα “ΗΛΕΚΤΩΡ Α.Ε. – ΑΡΣΗ Α.Ε.” του ομίλου “ΕΛΛΑΚΤΩΡ Α.Ε.”, υπό την επίβλεψη του Ειδικού Διαβαθμιδικού Συνδέσμου Νομού Αττικής (ΕΔΣΝΑ) στα Άνω Λιόσια (Αθήνα, Ελλάδα). Η πρώτη ύλη (ακατέργαστο δείγμα HMWI BASH) που παραλήφθηκε από την εγκατάσταση αποτέφρωσης ταξινομήθηκε σε επτά (7) κλάσματα (granulometric fractions). Ακολούθως, τα οκτώ (8) δείγματα χαρακτηρίστηκαν λεπτομερώς για τον προσδιορισμό πιθανών ορυκτολογικών ή/και χημικών διαφοροποιήσεων μεταξύ των παραγόμενων κλασμάτων που ενδέχεται να επηρεάζουν τη δυνατότητα αξιοποίησής τους.

Τα δεδομένα περίθλασης ακτίνων Χ κόνεως (PXRD) τόσο του ακατέργαστου δείγματος HMWI BASH όσο και των επιμέρους 7 κλασμάτων (ήτοι: +8mm, -8+4mm, -4+2mm, -2+1mm, -1+0,500mm, -0,500+0,250mm και -0,250mm) του κατέδειξαν υψηλή περιεκτικότητα σε άμορφο υλικό κυρίως στο ακατέργαστο και στα αδρόκοκκα κλάσματα, η οποία σταδιακά μειώνεται προς τα λεπτόκοκκα κλάσματα. Η ορυκτολογική σύσταση του ακατέργαστου δείγματος και των κλασμάτων του αποτελείτο από κρυσταλλικές φάσεις υψηλής θερμοκρασίας, όμοιες με εκείνες των ορυκτών γκελενίτη ($Ca_2Al[AlSi_2O_7]$), περοβσκίτη ($CaTiO_3$) και χριστοβαλίτη (SiO_2), εντός της αμόρφου μάζα του υλικού. Σύμφωνα με τις αναλυτικές μετρήσεις με χρήση WD-XRF και LA-ICP-MS, όλα τα δείγματα περιείχαν βαρέα μέταλλα και μεταλλοειδή, ορισμένα από αυτά παρόντα σε σχετικά υψηλότερες συγκεντρώσεις (πχ. Cr, Cu, Ni, Zn, κλπ.), και άλλα σε μικρότερες περιεκτικότητες (πχ. Co, Sn, V, As, κλπ.). Ο μόλυβδος συγκεντρώνεται σε πολύ μικρή ποσότητα σε όλα τα δείγματα (~3-9

ppm), ενώ το κάδμιο ανιχνεύτηκε σε ορισμένα από τα λεπτόκοκκα δείγματα μόνον με χρήση LA-ICP-MS. Σύμφωνα με τις μετρήσεις με χρήση ICP-OES, το αρχικό ακατέργαστο υλικό περιέχει χρυσό (Au) της τάξεως των 15 ppm. Αξίζει να τονιστεί ότι το σπάνιο αυτό μέταλλο απαντά κυρίως στο αδρόκοκκο κλάσμα (13 ppm) και λιγότερο στα λεπτόκοκκα κλάσματα (8-10 ppm) του υλικού. Επιπλέον, η περιεκτικότητα των δειγμάτων σε σπάνιες γαίες (συμπεριλαμβανομένων των 15 λανθανιδών, του Sc και του Y) βρέθηκε να αυξάνει από τα αδρόκοκκα προς τα λεπτόκοκκα κλάσματα. Η μικροσκοπική παρατήρηση των δειγμάτων με χρήση SEM/EDS αποκάλυψε την παρουσία σωματιδίων που περιέχουν μέταλλα, μεταξύ άλλων και βαρέων μετάλλων όπως Cr και Cu, πχ. οξειδίων του Ca και του Ti (περοβσκίτης) εντός μίας "πολυμεταλλικής" άμορφης μάζας.

Για την παραγωγή των πρεσαριστών αυτόκλειστων τούβλων χρησιμοποιήθηκε το ακατέργαστο δείγμα HMWI BASH, καθώς κι ένα μίγμα 1:1 των λεπτόκοκκων κλασμάτων (-0,500+0,250mm και -0,250mm), λόγω της χαμηλότερης περιεκτικότητάς τους σε άμορφο και της υψηλότερης ποσοστιαίας συμμετοχής του γκελενίτη, έχοντας ως αποτέλεσμα έξι διαφορετικές συνθέσεις (formulations) για λόγους σύγκρισης. Για την παραγωγή των αυτόκλειστων τούβλων χρησιμοποιήθηκαν τρεις διαφορετικές συνταγές (mix designs), δύο ανόργανα πολυμερή χρησιμοποιώντας τα προαναφερόμενα δείγματα HMWI BASH (IP100 mix design) είτε αναμειγνύοντάς τα με εμπορικό μετακαολίνη (IP_MK mix design), καθώς και ένα μίγμα τσιμέντου τύπου Portland (BLD mix design). Όλοι οι παραγόμενοι πυκνοί μονόλιθοι σκληρύνθηκαν υπό ίδιες υδροθερμικές συνθήκες σε αυτόκλειστο. Εν συνεχεία, προσδιορίστηκε η ορυκτοχημική τους σύσταση, ενώ για την αξιολόγησή τους έλαβαν χώρα δοκιμές αντοχής σε μονοαξονική θλίψη, και δοκιμές έκπλυσης σύμφωνα με το πρότυπο EN 12457/2. Οι μηχανικές αντοχές και οι ιδιότητες έκπλυσης των παραγόμενων μονολίθων από το ακατέργαστο δείγμα ήταν σαφώς ανώτερες συγκρινόμενες με εκείνες που διαμορφώθηκαν με χρήση του μείγματος των λεπτών κλασμάτων, καθιστώντας εν τέλει τη διαδικασία κοσκίνισης μάλλον περιττή για τη συγκεκριμένη εφαρμογή. Η προσθήκη υλικού μετακαολίνη αποδείχθηκε συγκριτικά μη ωφέλιμη ως προς την αντοχή των δοκιμίων σε μονοαξονική θλίψη. Από όλες τις εφαρμοζόμενες συνταγές, προτιμητέα ήταν εκείνη που είχε ως αποτέλεσμα την παραγωγή πρεσαριστών αυτόκλειστων δοκιμίων με χρήση μείγματος ακατέργαστου δείγματος. Τα πρεσαριστά αυτόκλειστα τούβλα που παρήχθησαν μέσω της συνταγής IP100 mix design περιείχαν μικρά ποσά Sb και As κατά 14% και 15% περισσότερο

σε σχέση με τις τιμές βάσει του προτύπου EN 12457/2, αντιστοίχως. Σε αντίθεση, τα αυτόκλειστα τούβλα που παρήχθησαν μέσω της συνταγής BLD mix design έδειξαν ότι δεσμεύουν τα δυνητικά τοξικά βαρέα μέταλλα και μεταλλοειδή σε αποδεκτές τιμές σύμφωνα με το πρότυπο EN 12457/2.

Keywords

Bottom Ash (BASH); Hospital Medical Waste Incineration (HMWI); stabilization; solidification; autoclaved bricks; hydrothermal curing; inorganic polymers (IPs); blended cement (BLD)

Λέξεις κλειδιά

Τέφρα πυθμένα, νοσοκομειακά απόβλητα, αποτέφρωση, σταθεροποίηση/στερεοποίηση, αυτόκλειστα τούβλα, υδροθερμική ωρίμανση, ανόργανα πολυμερή, ανάμικτα τσιμέντα

CONTENTS

Images

Figures

Tables

Appendix

Figures A

1 INTRODUCTION

1.1 Definitions, subject matter and scientific background

1.1.1 Sustainable Materials and Circular Economy

Sustainable materials are those that are sourced, produced and utilized in a way that minimizes the negative environmental and social impacts of their use, while maximizing the benefits throughout their life cycle (e.g., Taylor et al*.,* 2016). These materials help advance sustainability goals by reducing resource depletion, pollution and greenhouse gas emissions (e.g., Taylor et al*.,* 2016).

The transformation of wastes into sustainable materials is a key strategy in order to promote circularity and to reduce the environmental impact of waste disposal (e.g., MacArthur et al., 2015). This process involves converting waste materials into valuable resources that can be used as inputs in various industries, thereby minimizing the extraction of primary resources, and reducing waste generation (e.g., Silva et al., 2017).

Accordingly, the term "sustainable construction materials" refers to building materials produced by utilizing environmentally friendly practices either from raw materials and/or wastes streams (e.g., Saravanan & Rao, 2023 and references therein). Current environmental concerns dictate the adoption of sustainable practices in the construction industry, which assess different pathways to reduce energy consumption, CO_2 emissions and to promote waste valorization. Some representative approaches for sustainable construction materials manufacturing are summarized below:

- Recycled materials: Sustainable construction materials can be produced by industrial waste, such as fly ash, metallurgical slags, glass, construction and demolition wastes, etc. These materials are diverted from landfills and introduced in the production lines of brick, cement and pre-fabricated concrete elements, reducing the demand for primary resources and, therefore, to minimize waste generation (e.g., Silva et al., 2019 and references therein).

- Low-carbon manufacturing: Traditional brick and cement production processes often involve high energy consumption and significant carbon emissions caused by the calcination processes (e.g., Tautorat et al., 2023). Sustainable brick production focuses on less energy-intensive processes leading to lower greenhouse gas emissions through energy-efficient kilns, alternative fuel sources, and carbon capturing technologies (e.g., Silva et al., 2019 and references therein).
- Alternative binders: The construction industry utilizes high amounts of cement and concrete, the production of which is a significant source of carbon dioxide emissions. Sustainable bricks can be produced using alternative binders, such as metallurgical slags or bauxite residue (BR) and various ashes, which have lower carbon footprints and, therefore, contribute to the reduction of greenhouse gas emissions (e.g., Pontikes & Angelopoulos, 2013; Paixão et al., 2023).
- Modular and interlocking designs: Modular and interlocking brick designs allow for easy assembly and disassembly, facilitating reuse and reducing waste generation during construction and demolition activities (e.g., Silva et al., 2019 and references therein).
- Local sourcing: Locally sourced materials reduce transportation emissions associated to brick production and support local economies, also inspiring the model of industrial symbiosis (e.g., Napp et al., 2014 and references therein; Lu et al., 2020; Sourmelis et al., 2024). The utilization of locally available materials also reduces the environmental impact of extraction and processing (e.g., Taylor et al*.,* 2016).
- Waste to energy: Some types of wastes, such as the organic fraction of municipal solid wastes, can be converted into energy through incineration, anaerobic digestion, and gasification. This energy can be used to produce electricity, heat or biofuels, displacing the need for fossil fuels and reducing greenhouse gas emissions as well (e.g., Hoornweg et al*.*, 2013).
- Closed-loop systems: Implementing closed-loop systems, where waste materials are continuously recycled and reused within the economy, can further improve the sustainability of waste-to-material processes. By closing the loop, industry and community can minimize waste generation, conserve resources, and promote circularity in a symbiotic point of view (e.g., MacArthur, 2014; Sourmelis et al., 2024).

- Certifications and standards: Various certifications and standards, such as LEED (Leadership in Energy and Environmental Design) and BREEAM (Building Research Establishment Environmental Assessment Method), provide guidelines and set criteria for evaluating the sustainability of building materials, including bricks (e.g., Doan et al., 2017).

Transforming waste into a sustainable material is essential to achieve a circular economy and to reduce the environmental impact of waste disposal. According to the EU action plan, it requires cooperation among businesses, governments, and consumers to develop innovative solutions, invest in infrastructure, and promote sustainable consumption and production practices (European Commission, 2020).

Circular Economy (CE) is considered as a sustainable economic system in which economic growth is decoupled from resource use through the reduction and recirculation of natural resources (Kirchherr et al., 2023). In order to apply policies and business strategies, and to prioritize sustainable solutions based on evidence, it is crucial to quantify the circularity of products and services (or their contribution to the CE). New circularity metrics are being developed for this purpose, but they are often contradictory in form and content, contributing to confusion and misunderstanding of the concept of CE (Sauvé et al., 2016). Sustainable materials play a crucial role in advancing the goals of the circular economy. Industry can reduce resource consumption, minimize waste, and promote circularity throughout the product lifecycle by incorporating sustainable materials into product design and manufacturing processes (Silva et al., 2017).

1.1.2 Hospital Medical Waste

Hospital waste (a.k.a. medical waste or hospital medical waste or healthcare waste) refers to any waste generated during diagnosis, treatment, or immunization of human beings and/or animals, and in research activities pertaining to healthcare. Such a waste may include a wide range of hazardous and non-hazardous materials, such as (e.g., Kougemitrou et al., 2011; Anastasiadou et al., 2012; Bakkali et al., 2013):

- *Infectious Waste*: Waste contaminated with blood, bodily fluids, or other potentially infectious materials. This includes used needles, syringes, bandages, dressings, and cultures from laboratory work.
- *Pathological Waste*: Human or animal tissues, organs, body parts, or fluids removed during surgery, autopsy, or medical procedures.
- *Pharmaceutical Waste*: Expired or unused medications, drugs, vaccines, and other pharmaceutical products.
- *Chemical Waste*: Hazardous chemicals used in medical procedures, such as disinfectants, solvents, and laboratory reagents.
- *Radioactive Waste*: Materials contaminated with radioactive substances used in medical imaging, radiation therapy, or nuclear medicine procedures.
- *Sharps Waste*: Needles, syringes, lancets, scalpels, and other sharp objects used in medical procedures.
- *Non-hazardous Waste*: General waste generated in healthcare facilities, such as paper, cardboard, plastic packaging, and food waste.

Proper management of hospital waste is crucial to prevent the spread of infections, protect healthcare workers, patients and the environment, and comply with regulatory requirements. (e.g., Alvim-Ferraz & Afonso, 2005; Bdour et al*.,* 2007). Healthcare facilities are typically required to segregate, store, transport, and dispose of different types of medical waste safely and appropriately. This often involves using specialized containers, labeling, and treatment methods, such as autoclaving, incineration, or chemical disinfection, depending on the nature of the waste and local regulations (Kougemitrou et al., 2011).

In Greece, national regulations and guidelines are in place to govern hospital waste management. The main objective is to ensure that the handling, treatment, and disposal of medical waste are achieved safely. These regulations often require waste segregation, storage, transport, treatment, and final disposal methods to be followed.

Healthcare facilities in Greece are responsible for managing their own medical waste. They can do so by either using an in-house waste management system or by hiring licensed waste management companies. Special containers and vehicles are used to collect and transport the waste to prevent any spillage or contamination.

1.1.3 The "APOTEFROTIRAS S.A." Hospital Medical Waste Incineration Plant (HMWIP)

The Hospital Medical Waste Incineration Plant / HMWIP (a.k.a. "APOTEFROTIRAS S.A.") is currently being operated by the joint venture HELECTOR S.A. – ARSI S.A. of the ELLACTOR Group (**Image 1**). The owner of the entire project is the Association of Communities and Municipalities in the Attica Region (ACMAR) in Attica, Greece (a.k.a. Special Inter-Collective Association of the Prefecture of Attica / "EDSNA"). "APOTEFROTIRAS S.A." is a Greek company specializing in medical waste management and maintenance of the ACMAR medical waste incinerator located to Ano Liossia, near Athens Metropolitan Area (Kougemitrou, 2008; Kougemitrou et al., 2011).

Image 1: The hospital medical waste incinerator plant (HMWIP) operated by the "APOTEFROTIRAS S.A." located to Ano Liossia, near Athens Metropolitan Area, Greece (Kougemitrou, 2008).

The HMWIP has been established since 2002 by the ACMAR and had been operated by the joint venture "ANSALDO TECNITALIA S.P.A. – ERGOKAT S.A. – TOMI S.A.". During the last decades, the management of the plant and the medical waste transport network was taken over by the joint venture joint venture HELECTOR S.A. – ARSI S.A. (henceforth referred to as "APOTEFROTIRAS S.A.") of the ELLACTOR Group (personal communication with the

HMWIP administration; internal report). Article 37591/2031/2003 of the Greek Constitution, entitled as "Measures and Terms for the Management of Medical Waste from Sanitary Units", outlines the procedures to be followed for the proper management of the hazardous medical waste. The main objective of the law is to ensure that the environment and public health are protected.

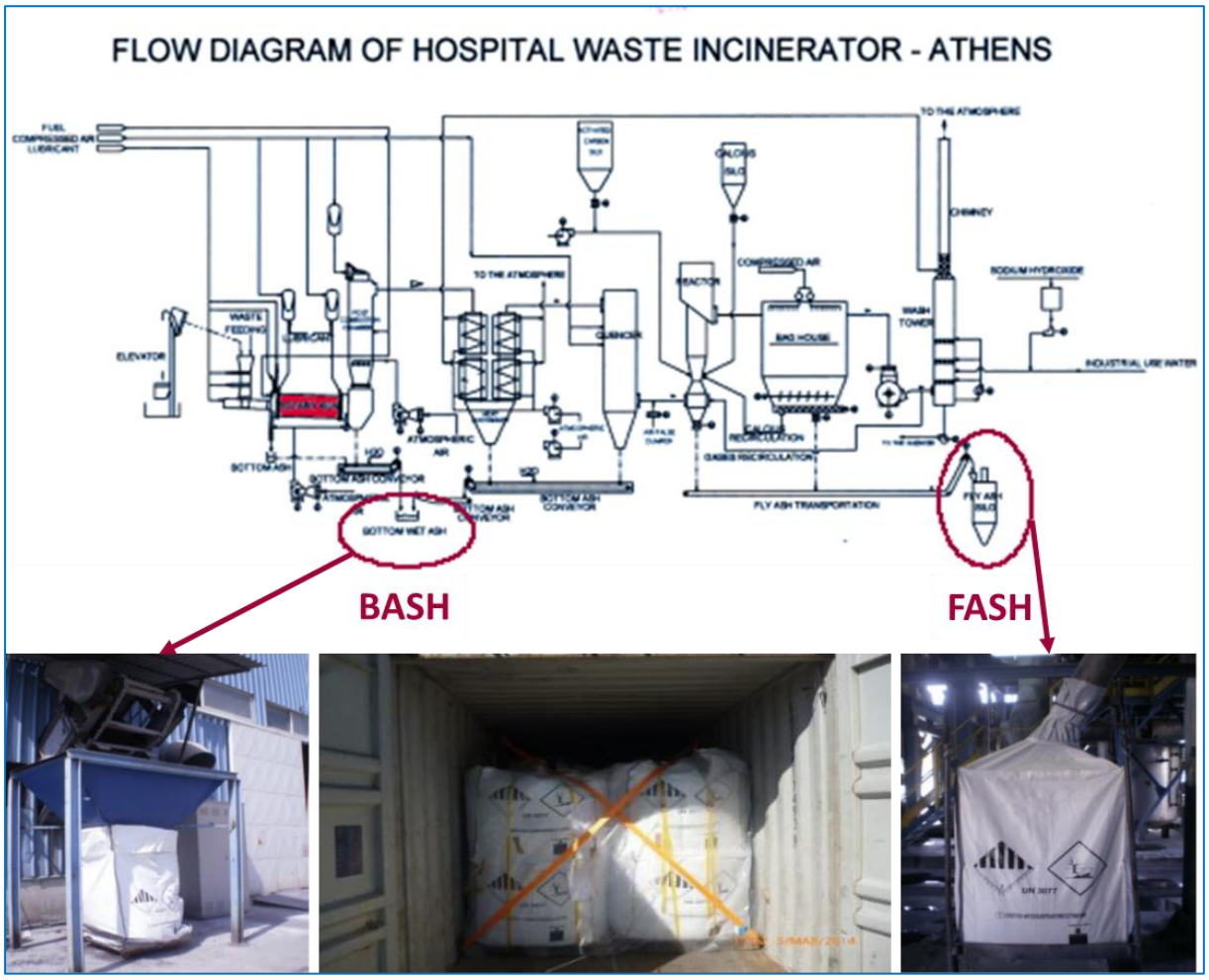

Image 2: The flow diagram of the HMWIP operated by "APOTEFROTIRAS S.A.". The bottom (BASH) and fly (FASH) ashes collected in appropriate bags and their final disposal storage place in the plant (Kougemitrou, 2008; Kougemitrou et al., 2011; HMWIP internal report)

More than 14,000 tonnes of medical waste is generated annually, 53% of which originating from Athens' metropolitan area (Attica, Greece), which has a population of approximately 4 million people. The need for management of this hazardous waste is therefore a driving force in the field of collection, transport and treatment of this waste. The main activity of "APOTEFROTIRAS S.A." is the implementation of a public contract with ACMAR for the operation and maintenance of the HMWIP, as well as the collection and transport of

medical waste to the facility. “APOTEFROTIRAS S.A.” follows an internal protocol for the collection and transport of medical waste, as well as an ISO 14001:2015 Environmental Management Certification, complying with safety and environmental regulations. The waste handling process involves weighing of the medical waste on a weighbridge and disposal into the facility's cold chambers for storage. The waste remains in storage for a maximum of 2-3 days and are then unloaded on a first-in, first-out basis. There are then two independent lines for high temperature incineration (>1100 °C). The time spent outside the cold store does not exceed 48 hours and 24 hours during the winter and the summer, respectively. There are two types of waste from the incineration process (**Image 2**): (a) effluent, which is evaporated to produce distilled water; (b) fly ash (FASH), which is collected in large bags and sent abroad for storage, and (c) bottom ash (BASH), which is collected into drums and temporarily stored at the plant (Kougemitrou, 2008; Kougemitrou et al., 2011; HMWIP internal report).

1.1.4 Geopolymers (GPs)

Geopolymers (GPs) are a category of binders that is formed through a process called geopolymerization, which takes place among cementitious aluminosilicate raw materials ad/or other binders (such as Metakaolin / MK) acting both as Supplementary Cementing Materials (SCMs) and concentrated activating solutions as “alkali activators”, through a process so-called “geopolymerization” involving an exothermic reaction between the former and the latter (e.g., Luhar et al., 2019 and references therein; Cai et al., 2023). Geopolymerization results in a charge-balanced structure by cations or supervalent phosphate, formed under highly alkaline conditions without requiring high-temperature processing (e.g., Luhar et al., 2019 and references therein; Kriven et al., 2024 and references therein). Geopolymers are typically based on mixtures of aluminosilicate powders combined with alkali-silicate solutions, resulting in the formation of a three-dimensional tecto-aluminosilicate matrix (Matsimbe et al., 2022 and references therein). GPs are considered as a sub-set of inorganic polymers (IPs), analogous to aluminosilicate glasses, because of their similar structure characteristics (e.g., Hertel & Pontikes, 2020 and references therein).

The synthesis of geopolymers involves the alkaline or alkali-silicate activation of solid alumina- and silica-containing precursor materials at ambient (room) or elevated temperatures (up to 100 °C) and at atmospheric condition (e.g., Provis et al., 2005; Luhar et

al., 2019 and references therein). These materials exhibit amorphous microstructures and are considered to be precursors of zeolites (Król & Rożek, 2018). Geopolymers are known for their high temperature stability, making them advantageous over conventional cement binders (e.g., Luhar et al., 2019 and references therein), especially in applications requiring fire resistance (Guerrieri & Sanjayan, 2010). Geopolymers have gained attention as sustainable alternatives to traditional cement-based materials due to their lower carbon footprint and potential for utilizing industrial waste materials like fly ash, blast furnace slag, rice husk ash etc. (e.g., Luhar et al., 2019 and references therein; Wan-En et al., 2021). The properties of geopolymers, such as their compressive strength and durability, can be tailored by adjusting the processing conditions and the composition of constituent materials (e.g., Aldawsari et al., 2022 and references therein). Additionally, the workability and mechanical properties of geopolymers have been found to be superior to those of conventional concrete, highlighting their potential for use as full or partial replacements for Ordinary Portland Cement / OPC (Ali et al., 2020).

1.1.5 Blended cement systems

A promising way to reduce the environmental impact of the Ordinary Portland Cement (OPC) production is through the utilization of blended cement systems. These systems typically consist of a combination of OPC and supplementary cementitious materials (SCMs), such as fly ash, metallurgical slags or natural primarily calcined clays (e.g., natural clayey argillaceous materials so-called “Metakaolin / MK”), both as binders. Blended cements exhibit lower environmental impact, even when using SCMs with lower grindability, highlighting their potential for sustainable construction practices (Boesch & Hellweg, 2010).

The incorporation of SCMs in blended cement systems influences the pore structure and hydration characteristics of the resulting mixture. Blended systems tend to have a higher total porosity at early ages due to the slower reaction of SCMs compared to OPC (Berodier & Scrivener, 2015). However, it has been shown that the incorporation of Ca-rich SCMs, such as ground granulated blast furnace (GGBFS), in blended cements can achieve comparable mechanical strength to OPC (e.g., Marchon & Flatt, 2016). The hydration reactions of a blended cement system initiates by the pozzolanic reactions between the OPC and water leading to the dissolution of SCMs (He et al., 2021). Ultimately, the primary binding phases of

(blended)-cement-/cementitious systems, such as calcium silicate hydrate (C-S-H) and calcium aluminum silicate hydrate (C-A-S-H) are crystallized (e.g., Borno et al., 2023), which are responsible for the strength development (e.g., Chen et al., 2004; Arora et al., 2016; Rakhimbaev et al., 2020).

The use of blended cements can lead to improvements in the durability and mechanical performance of concrete structures. Blended cements have maintained superior mechanical performance in chemically harsh environments, while reducing their cost and carbon dioxide emissions compared to the OPC (Jacobsen et al., 2013).

1.1.6 Hydrothermal curing of building materials

Hydrothermal curing involves the brief exposure of a building material (e.g., autoclaved aerated concrete, sand-lime bricks, etc.) to moderate temperatures, high pressures, and high relative humidity utilizing an autoclave (e.g., Shi & Hu, 2003; Ranjbar et al., 2020; Ramadan et al., 2023; Djobo & Tome, 2024). This process promotes pozzolanic reactions, enhancing the early hydration of cementitious materials (e.g., Hanehara et al., 2001). Rapid precipitation of crystalline compounds densifies the microstructure of the material, minimizing drying shrinkage while enhancing modulus and compressive strength (e.g., Xiong et al., 2023).

Curing in an autoclave typically involves subjecting materials to specific conditions of temperature, pressure, and humidity within the sealed chamber of the autoclave. These conditions are carefully controlled to facilitate the curing process effectively. The typical conditions found in autoclave curing are summarized below (e.g., Shatat et al., 2016; Ray, 2002):

- Temperature: Hydrothermal curing exposes materials to elevated temperatures, typically between 120 °C and 250 °C (250 °F to 480 °F), depending on the materials being cured and the requirements of the curing conditions.
- Pressure: The pressure development is closely related to the temperature of the process. The higher the temperature settings, the higher the pressure development in the autoclave chamber. Pressure levels can range between 1 and 12 bars (175 psi to 1750 psi), depending on the curing process. The pressure accelerates the chemical

reactions taking place in the material eliminating the porosity and promoting better bonding between particles or fibers.

- Humidity: Humidity is introduced or maintained in the autoclave chamber to facilitate hydration reactions or to prevent excessive drying of the materials being cured. Moisture levels may vary depending on the curing requirements.
- Time: The duration of the hydrothermal curing varies depending on several factors, such as the type of materials, their thickness, the desired material properties and the curing process. Curing times typically range from several hours to several days, with temperature, pressure and humidity conditions being monitored consistently throughout the curing period.
- Cooling rate: At the end of the curing process, the autoclave is gradually depressurized by lowering the temperature until ambient levels. The cooling rate is controlled to prevent thermal shock to the cured materials and to ensure their stability.

Hydrothermal conditions facilitate the formation of diverse crystalline compounds influenced by the chemical composition of the incorporated SCMs. Calcium-enriched SCMs yield various hydrated calcium silicate crystalline compounds, such as tobermorite ($Ca_5Si_6(O,OH)_{18}•5H_2O$; Merlino et al., 1999) and xonotlite ($Ca_6Si_6O_{17}(OH)_2$; Hejny & Armbruster, 2001). The structural features of both the peculiar crystalline phases, also known as C-S-H phases, classify them in the phyllosilicate and the double chain inosilicate group, respectively (Merlino et al., 1999 and references therein; Hejny & Armbruster, 2001 and references therein). The lath-shaped (needle-like) structure of xonotlite improves thermal insulation, chemical resistance (Hartmann et al., 2015), and the ductility of autoclaved materials (Javaid et al., 2022). However, its morphology and low density can compromise the compressive strength (Javaid et al., 2022). Tobermorite, owing to its platelet-like morphology, benefits the compressive strength of the materials (Çiçek & Tanriverdi, 2007; Różycka & Kotwica, 2022). The formation of these C-S-H minerals is influenced by several parameters such as temperature, Ca/Si ratio, and curing time (Merodio-Perea et al., 2022). Tobermorite formation is promoted at a temperature range of 160-200 °C, a Ca/Si ratio of 0.83, and curing times up to 15 hours (Merodio-Perea et al., 2022; Cai et al., 2023).

C-S-H phases precipitate directly from the aqueous solution in the pores of the material (Galvánková et al., 2016). The process is divided into three main stages (Aretxabaleta

et al., 2023; Shen et al., 2023). During the first stage, the dissolution of the raw materials initiates to form a C-S-H gel. The second stage involves the crystallization of calcium silicate hydrate gel forming C-S-H crystallites. The last stage includes the crystalline growth of the C-S-H crystalline phases, which contribute to the compressive strength of the material. The structure densification also contributes to the immobilization of heavy metals and metalloids (Lu & Li 2019; Miao et al., 2022).

The most representative example of autoclaved building materials is the Autoclaved Aerated Concrete (AAC). AAC usually consists of a mixture of sand (SiO_2), cement, lime (CaO), gypsum ($Ca(SO)_4 \bullet 2H_2O$), and alumina (Al_2O_3). Alumina reacts with the lime and water to produce hydrogen gas, which creates tiny air bubbles throughout the material (e.g., Narayanan & Ramamurthy, 2000 and references therein). The mixture is casted into molds and then cured in an autoclave, a high-pressure vessel, under steam. The high-pressure steam curing process results in the formation of a cellular structure to the material's surface, similar to that of a sponge. AAC offers many advantages over traditional building materials, such as low weight, which facilitates their handling and transportation (e.g., Rossi et al., 2022). Their cellular structure provides excellent thermal and sound insulation, improving energy efficiency and reducing operational costs (e.g., Walczak, 2023). In addition, AAC construction elements are fire resistant ensuring safety and comfort within the built environment (Rathore, 2018 and references therein).

Sand-lime brick is another example of autoclaved building material becoming increasingly popular in various European nations including Poland, Germany, Spain and Slovakia (e.g., Jasińska et al., 2021). These bricks are usually produced by autoclaving a mixture of sand, lime and water, which undergoes a hydrothermal treatment to accelerate the maturation of the material, resulting in an artificial stone as the final product (Kostrzewa & Stępień, 2017). The composition of sand-lime bricks plays a crucial role in their structural integrity and performance, with factors such as autoclave conditions, temperature, steam pressure and quality of constituents affecting the crystalline phases produced in the bricks (Kostrzewa & Stępień, 2017).

Research has also explored the use of sand-lime bricks in environmental applications, such as the use of them as low-cost adsorbents for the removal of copper (II) from water, demonstrating their potential for water treatment applications (Zhang et al., 2019). In

addition, the modification of sand-lime bricks with additives, such as bentonite, has been proved to improve their mechanical properties and workability in fresh condition (Owsiak & Kostrzewa, 2017). Furthermore, Owsiak & Kostrzewa (2017) compared sand-lime bricks with common bricks, highlighting the high environmental impact of energy-intensive clay sintering in common brick production. Besides, Mollaei et al. (2022) demonstrated that sand-lime bricks use medium-temperature, high-pressure hydrothermal curing, resulting in lower energy consumption. Therefore, sand-lime bricks offer a sustainable and durable alternative in construction, with ongoing research focusing on improving their properties, exploring environmental applications and promoting environmentally friendly practices in brick production.

1.2 Purpose & targets of the thesis

Applying the hydrothermal curing mentioned above, this diploma thesis examines the possibility of valorization of the bottom ash (BASH) as a Supplementary Cementitious Material (SCM) for autoclaved, pressed bricks (dense monoliths). It deals with the scientific knowledge to the sustainable brick manufacturing sector, in terms of waste valorization and shaping and curing processes. To this trajectory, it focuses on the production of hydrothermally cured, inorganic polymer and OPC-based, pressed bricks, incorporating Hospital Medical Waste Incineration Bottom Ash (HMWI BASH). The crystalline phases formed post-curing are influenced by the original mineral-chemistry of the HMWI BASH and the additional Ordinary Portland Cement (OPC), SCMs (metakaolin / MK), and activating solutions (Na-silicate solution) incorporated in the mixture. Additionally, the effectiveness of the brick production process in encapsulating heavy elements is evaluated.

The mineral-chemistry and the properties of the initial HMWI BASH sample (henceforth referred to as “raw sample”) and its seven (7) granulometric fractions (i.e., +8mm, -8+4mm, -4+2mm, -2+1mm, -1+0.500mm, -0.500+0.250mm and -0.250mm) were assessed as potential raw materials for the production of inorganic polymer and blended cement, autoclaved, pressed bricks. The suitability of HMWI BASH as a building material was evaluated based on its mineralogical and chemical composition, both in its raw form and across the corresponding seven granulometric fractions. Additionally, the end products (autoclaved

bricks) were subjected to mineralogical analysis, micro-textural observation, mechanical and leaching assessments. The mix designs used in this BSc thesis serve as a "proof of concept," demonstrating that large quantities of HMWI BASH can be incorporated into autoclaved bricks, achieving high strength, while complying with environmental policies (EN 12457/2) regarding the leaching of hazardous elements.

A future work for the improvement of the HMWI BASH valorization may include:

- ✓ Optimization of the mix designs to maximize the compressive strength of the pressed bricks while minimizing the leaching of heavy metals.
- ✓ Durability assessment (e.g., freeze-thaw cycles, water solubility, durability in chemically harsh environments).

2 MATERIALS AND METHODS – MIXED DESIGNS

The experimental part of the present work was partially at the school of Mineral Resources Engineering / SMRE (Technical University of Crete / TUC) and at the Department of Materials Engineering / MTM (KU Leuven). The characterization and evaluation of the studied material was performed at the SMRE/TUC and the MTM/KUL, while the production and the assessment of the dense monoliths were performed at the facilities of MTM/KUL.

2.1 Sample preparation

The HMWI BASH raw sample was collected from the "APOTEFROTIRAS S.A." hospital medical waste incinerator plant. The studied inhomogeneous material had a brownish-black color and exhibiting a glassy-like appearance. All the visible and relatively large pieces of metal, needles and glasses, that were incorporated into HMWI BASH, were carefully separated by hand. For the preparation of the studied material, the raw sample was dried at 105 °C. Then, a Jones riffle sample splitter was used to separate the material into representative sub-samples. Afterwards, almost 11.7 kg of the homogeneous raw sample was classified into certain particle size fractions using a series of ASTM Test sieves, following methodology described by Gidarakos et al. (2009). In our case, the corresponding fractions were: +8mm, -8+4mm, -4+2mm, -2+1mm, -1+0.500mm, -0.500+0.250mm, and -0.250mm (**Image 3**). For the production of the pressed autoclaved bricks (dense monoliths) the HMWI BASH raw sample and a 1:1 mixture of its 0.500+0.250mm and -0.250mm fractions were used, due to their lower amorphous and higher gehlenite content, for comparison (see: **Chapter 3**). A detailed chemical and mineralogical analysis of the raw sample and its fractions will clarify the distribution of crystalline compounds, heavy metal partitioning, and reactivity, determining whether sieving is necessary for improved building material performance.

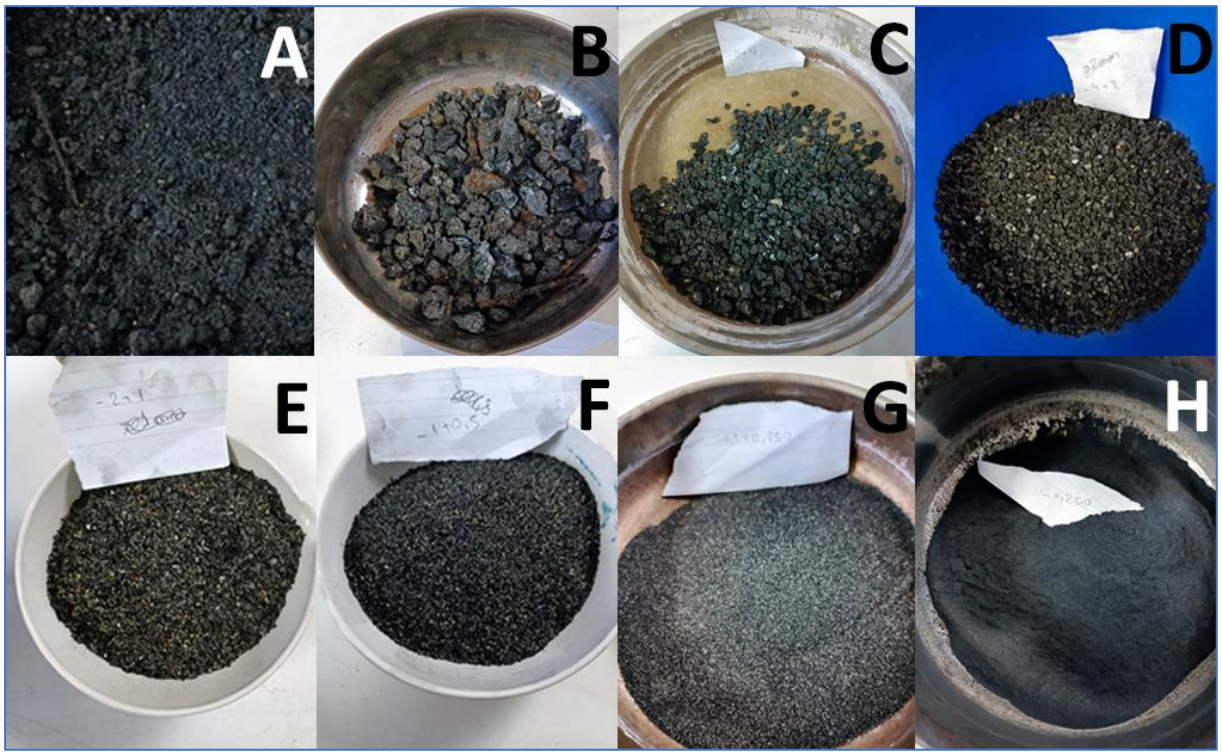

Image 3: The investigated HMWI BASH raw sample (A) and its separated fractions by a series of ASTM Test sieves, i.e. the +8mm fraction (B), the -8+4mm fraction (C), the -4+2mm fraction (D), the -2+1mm material (E), -1+0.500mm fraction (F), the -0.500+0.250mm fraction (G) and the -0.250mm fraction (H).

2.2 Specific Surface Area (SSA) – Particle Size Distribution (PSD) & Blain test (EN 196-6)

The HMWI BASH raw sample and the specific fractions (-0.500+0.250mm and -0.250mm) were initially homogenized via disc milling using a FRITSCH Pulverisette-13 device, and then milled for 40 minutes in a WIENER 1S ball-mill attritor with zirconia balls, using a material-to-balls ratio of 1:6. Power consumption was monitored to assess the energy efficiency of the milling process.

The specific surface area (SSA) was measured using the Blaine test (EN 196-6), while particle size distribution (PSD) and bulk density analyses provided data on the physical properties and homogeneity of the milled materials (**Image 4**). PSD was analyzed through laser diffraction on diluted suspensions, using approximately 250 mg of milled HMWI BASH in a sonicated, distilled water bath within a Beckman Coulter LS13 320 laser diffraction device with an ALM module. Bulk density was measured using a Micromeritics AccuPyc 1330 pycnometer.

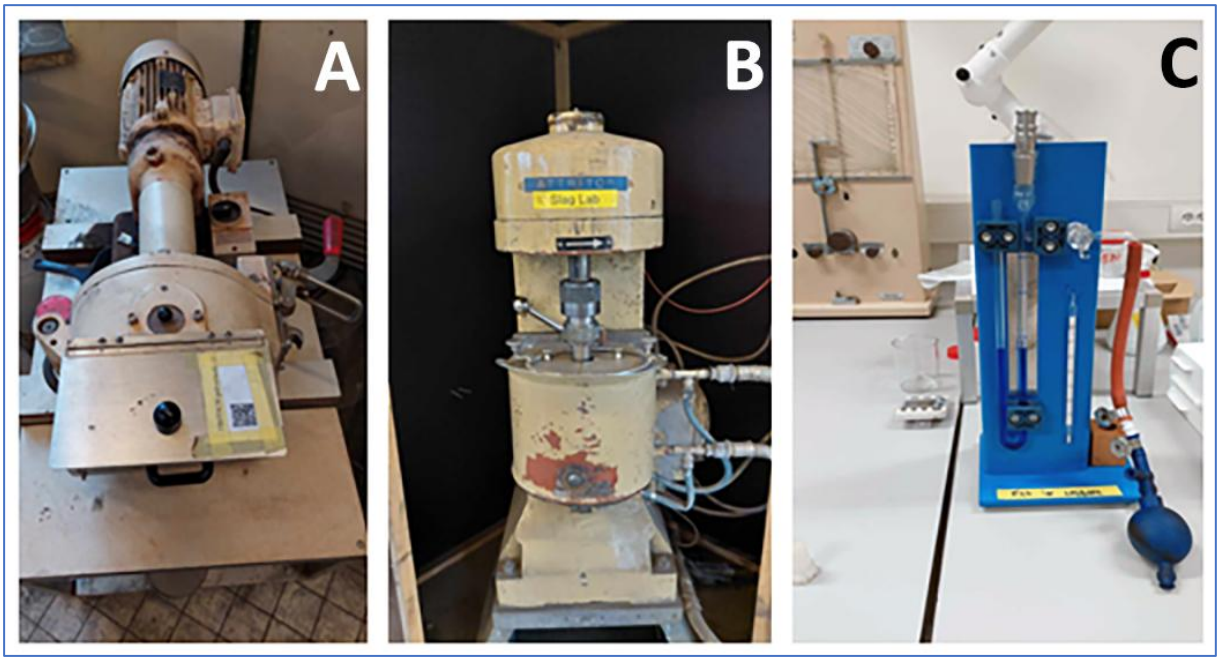

Image 4: Mechanical equipment for the mineral processing: (A) the Fritsch disk milling machine, (B) the Wiener 1S attritor using 10 mm steel or zirconia milling balls, and (C) the SSA measurement device for Blaine test (ASTM C204).

The applied methodology (**Figure 1**) allowed for a detailed comprehension of the physical properties of the studied raw material and its particular fractions (-0.500+0.250mm, -0.250mm), aiding in informed decision-making for various applications.

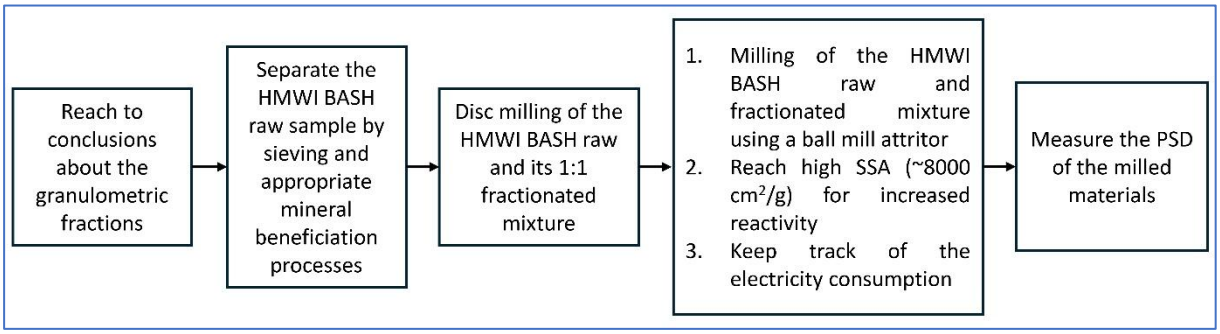

Figure 1: The mineral processing flowchart in the frame of the present BSc thesis.

2.3 Powder X-ray Diffraction (PXRD)

Bulk mineralogical composition of all the studied HMWI BASH raw and size fractions samples was determined by powder X-ray diffraction (PXRD) using a Bruker D2 Phaser Diffractometer (CuK_α radiation, scan range: 5-70° with a step of 0.02°) at the Laboratory of Applied Mineralogy of the Department of Materials Engineering, KU Leuven. The studied

samples were homogeneously powdered using agate mortar and carefully loaded onto the XRD holders avoiding particles' orientation. An anti-scatter slit of 1 mm was utilized. Phase identification was initially obtained using the database from ICDD (International Centre for Diffraction Data) and was conducted using EVA® software (Bruker).

For the quantitative XRD analysis (QXRD) of the studied samples a pure rutile (TiO_2) external standard was utilized. The TOPAS® software package (Faddegon et al., 2020) was employed for quantifying the identified mineralogical phases.

Besides, qualitative PXRD measurements on the grounded dense monoliths were applied in order to check their bulk mineralogical composition, the formation of additional mineralogical phases during the mix design processes and to detect any differences in the mineralogy between the produced autoclaved bricks and the raw and fractionated HMWI BASH materials.

2.4 Thermo gravimetric analysis/Differential Scanning Calorimetry (TGA/DSC)

For the thermal characterization of the HMWI BASH studied material (raw sample and its fractions), a Thermo-Gravimetric – Differential Scanning Calorimetry (TGA-DSC) simultaneous analysis was performed by a Netzsch STA 449 F1 using a temperature range of 25-900 °C, with a heating rate of 10 °C/min. The measurements were performed in a N_2 atmosphere. The device carries a precision micro scale, with a 25 ng detection limit, able to detect minor mass changes during the heating of the investigating sample. After powdering in agate mortar in order to reach a mean grain size of 20 μm, samples of 80 mg each were placed in alumina crucibles. Prior to the TGA-DSC analysis, a background measurement (without the sample) was carried out using an empty alumina crucible under the same conditions, in order to eliminate the mass changes caused by buoyancy in the gas atmosphere, and to establish a baseline for the thermobalance. The loss on ignition (L.O.I.) of the samples was calculated as follows:

$$\textbf{L.O.I.} = \frac{(\text{sample weight})25 - (\text{sample weight})950}{(\text{sample weight})25} * \mathbf{100}$$

2.5 Wavelength Dispersive X-ray Fluorescence (WD-XRF) Spectrometry

The bulk chemical composition for major elements of the HMWI BASH was determined by a Bruker S8 Tiger wavelength dispersive X-ray fluorescence (WD-XRF) spectrometer utilizing fused glass beads. Before the fusion, the HMWI BASH samples were dried at 105 °C. The glass beads were prepared by precisely weighing and homogenizing 1.4 g of HMWI BASH sample with a 50:50 Li-tetraborate:Li-metaborate X-ray flux. For enhanced binding, 1 mL of LiBr solution was added in the mixture. The samples underwent fusion at 1050 °C for 16 minutes. To calibrate the spectrometer, ten (10) calibration standards were prepared based on the average bulk chemical composition of various HMWI BASH samples reported in the literature (**Image 5**).

Image 5: The ten (10) calibration standards (left image) and the Bruker S8 Tiger WD-XRF spectrometer (right image).

2.6 Inductively Coupled Plasma Optical Emission Spectrometry (ICP-OES)

Inductively coupled plasma optical emission spectrometry (ICP-OES) serves as a multi-element source, capable of exciting numerous elements simultaneously within an inert argon atmosphere. Spectroscopic analysis in emission mode necessitates the identification and selection of appropriate analysis lines. However, this task is intricate in ICP-OES due to the availability of numerous emission lines from both neutral atoms (10%) and ions (90%), each varying in relative intensity leading to potential spectral interferences.

A real sample analysis typically yields average relative standard deviations ranging from 1 to 10%. To enhance accuracy, a blank solution of nitric acid (HNO_3) and hydrochloric acid (HCl) in a 3:5 ratio was prepared, along with standard solutions to create the calibration curve of the instrument. ICP-OES detection limits typically range from 1 to 100 parts per billion (ppb), akin to those of flame atomic absorption spectroscopy (AAS). Notably, ICP-OES boasts the lowest detection limits for numerous refractory elements such as boron and titanium.

With respect the bulk chemistry of the raw sample, its fractionated HMWI BASH samples and the leachates of the produced dense monoliths, major and trace elements analyses were performed using a Varian 720 ES. The analytical instrument is an axial simultaneous ICP-OES, equipped with a cooled cone interface and oxygen-free optics, enabling measurements in the low UV range, particularly useful for elements such as sulfur, phosphorus, and aluminum.

For the digestion procedure of the raw and fractionated HMWI BASH, the materials were prepared by carefully weighing between 0.500 g and 0.800 g of sample into designated digestion tubes. The following acids were sequentially added: 5 mL of hydrochloric acid (HCl), 3 mL of nitric acid (HNO_3), and 5 mL of hydrofluoric acid (HF). The tubes were securely sealed to minimize fume exposure and placed in a microwave digestion system. The samples were digested at 200 °C for 15 minutes with controlled rotation, followed by a cooling phase. When the temperature dropped below 80 °C, the program was terminated, and the tubes were left to cool for an additional 15 minutes before opening. This initial digestion process, specifically designed for slag samples, took approximately 45 minutes.

Each time, in order to prepare the final replicates appropriate for ICP-OES analysis, 6 g of boric acid was dissolved in 25 mL of water. Each digestion tube was cautiously loosened to release pressure and prevent agitation, and the boric acid solution was then gradually added to neutralize any residual HF. The tubes were resealed and subjected to a second microwave digestion program at a maximum temperature of 170 °C for 45 minutes, optimized for boric acid neutralization.

After this second digestion, the tubes were opened slowly, and the contents were rinsed with ultrapure water. The solution was then transferred to a sampler tube, with additional ultrapure water used to rinse any remaining residue and to dilute the final solution to a total volume of 100 mL. Once cooled, the sampler tube was sealed with laboratory tape, thoroughly mixed, and stored in sample bottles, ready for ICP-OES analysis.

2.7 Laser Ablation Inductively Coupled Plasma Mass Spectrometry (LA-ICP-MS)

Focusing on the trace element distribution in the studied HMWI BASH samples, a bulk chemical analysis was conducted by means of Laser Ablation Inductively Coupled Plasma Mass Spectrometry (LA-ICP-MS) at the WWU Münster (Germany). Sample ablation for trace elements analysis has been done using a 193 nm ArF excimer laser (Analyte G2, Photon Machines) with a repetition rate of 10 Hz and energy of up to 15 J/cm^2 and a laser beam with a maximum diameter of ~250 µm throughout the measurements.

According to the literature (Kurosawa et al., 2017), a small amount of each powdered material from the HMWI BASH raw sample and its seven (7) fractions was taken in order to prepare the fused whole-rock glasses using exactly the same process followed during the WD-XRF fused beads preparation (see: **Chapter 2.5**). Afterwards, the eight (8) fused whole-rock glasses were carefully cracked. One fragment from each glass was then embedded into an epoxy resin. The resin was left to harden overnight. The surface of the resin was grounded and polished (**Image 6**) in the grinding and polishing laboratory of the MTM/KUL, similar to the process that is mentioned in the following chapter (see: **Chapter 2.8**).

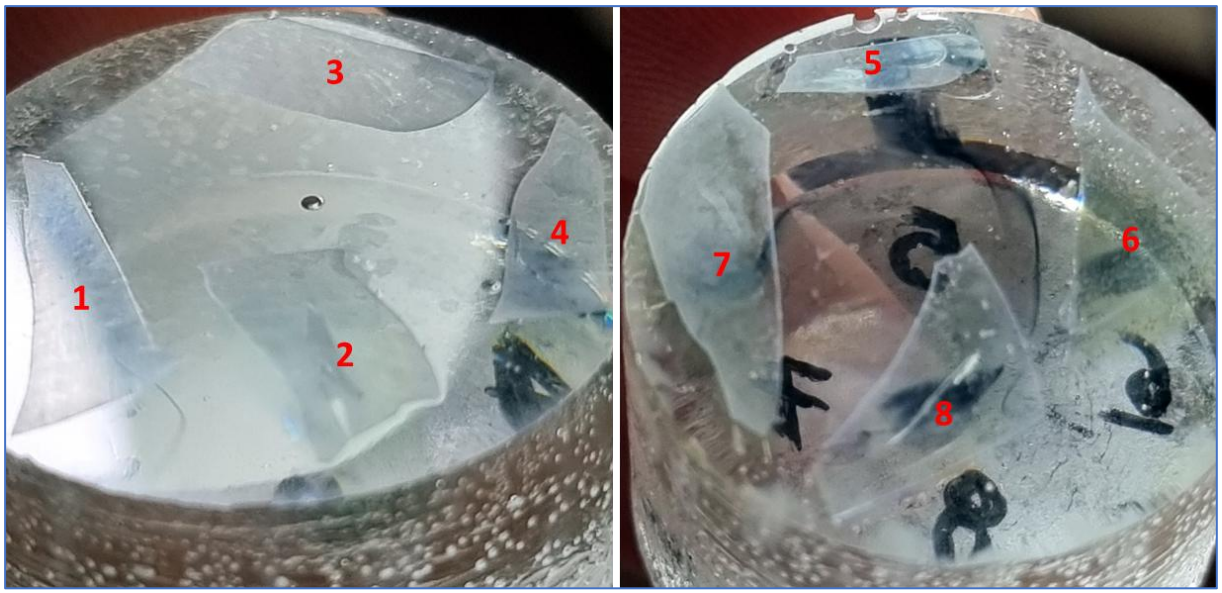

Image 6: The eight (8) fused whole-rock glasses that were carefully cracked embedded into epoxy resin. Numbers 1, 2, 3, 4, 5, 6 ,7 and 8 stand for the raw and its size fraction samples (i.e., +8mm, -8+4mm, -4+2mm, -2+1mm, -1+0.500mm, -0.500+0.250mm and -0.250mm), respectively.

Three (3) point analysis were conducted; one (1) at the core and two (2) on the rim on each fused bead fragment. Including the major elements that were previously measured using WD-XRF, a total of fifty-three (53) elements were analyzed. The following masses were monitored: ^{45}Sc, ^{49}Ti as internal standard, ^{51}V, ^{59}Co, ^{60}Ni, ^{65}Cu, ^{66}Zn, ^{69}Ga, ^{73}Ge, ^{75}As, ^{77}Se, ^{85}Rb, ^{88}Sr, ^{89}Y, ^{90}Zr, ^{93}Nb, ^{95}Mo, ^{111}Cd, ^{115}In, ^{118}Sn, ^{121}Sb, ^{131}Cs, ^{137}Ba, ^{139}La, ^{140}Ce, ^{141}Pr, ^{146}Nd, ^{147}Sm, ^{151}Eu, ^{157}Gd, ^{159}Tb, ^{163}Dy, ^{165}Ho5, ^{166}Er, ^{169}Tm, ^{172}Yb, ^{175}Lu, ^{178}Hf, ^{181}Ta, ^{182}W, ^{195}Pt, ^{208}Pb208, ^{232}Th and ^{238}U. Representative reference materials were used as external standards (Jochum et al., 2007). In particular, for the trace elements in glass the SRM-612 standard from the National Institute of Standards & Technology (NIST) of the Department of Commerce (USA) was used. All the LA-ICP-MS data throughout the run products were calculated and monitoring using the GLITTER software (van Achterbergh et al., 2001, Griffin et al., 2008). The LA-ICP-MS measurements of the studied samples were achieved using QA/QC procedure that is summarized in the following **Table 1**.

Table 1: QA/QC data concerning bulk chemical analysis of the studied HMWI BASH samples by LA-ICP-MS. The STD1 (corresponding to the NIST SRM-612; Jochum et al., 2007) is the external standard, while ^{49}Ti has been measured as an internal standard.

Analyte Unit	Sc 45	Ti 49	V 51	Co 59	Ni 60	Cu 65	Zn 66	Ga 69	Ge 73	As 75	Se 77	Rb 85	Sr 88	Y 89	Zr 90	Nb 93	Mo 95	Cd 111	In 115	Sn 118	Sb 121	Cs 133
	ppm	*ppm*	*ppm*		*ppm*	*ppm*	*ppm*	*ppm*	*ppm*	*ppm*	*ppm*	*ppm*	*ppm*	*ppm*	*ppm*	*ppm*	*ppm*	*ppm*	*ppm*	*ppm*	*ppm*	*ppm*
STD1	39.41	42.25	39.28	34.80	37.99	36.69	40.49	38.29	36.26	36.14	15.07	31.31	78.69	37.63	36.61	39.26	36.78	28.02	38.78	38.15	35.42	42.31
1 sigma error	*1.47*	*4.27*	*1.87*	*1.46*	*4.62*	*2.00*	*3.35*	*6.87*	*2.59*	*2.25*	*2.19*	*1.24*	*3.06*	*1.46*	*1.87*	*1.61*	*1.67*	*1.56*	*1.22*	*2.04*	*2.10*	*1.66*
MDL (99% confidence)	*0.11*	*0.70*	*0.05*	*0.20*	*0.23*	*0.25*	*0.43*	*0.04*	*0.19*	*0.44*	*<0.00*	*0.04*	*0.03*	*0.01*	*0.20*	*<0.00*	*<0.00*	*0.34*	*0.01*	*0.05*	*0.08*	*0.01*
STD1	39.44	44.35	37.25	36.02	37.42	37.08	40.10	37.15	35.34	36.44	17.69	31.56	79.53	38.15	38.30	38.83	37.11	28.36	38.65	37.86	34.25	42.62
1 sigma error	*1.48*	*4.51*	*1.78*	*1.51*	*4.55*	*2.04*	*3.37*	*6.64*	*2.57*	*2.29*	*2.59*	*1.25*	*3.09*	*1.48*	*1.96*	*1.59*	*1.70*	*1.62*	*1.22*	*2.03*	*2.04*	*1.67*
MDL (99% confidence)	*0.14*	*0.76*	*0.33*	*0.21*	*0.27*	*0.24*	*0.45*	*0.06*	*0.24*	*0.16*	*<0.00*	*0.05*	*0.03*	*0.01*	*0.20*	*0.01*	*<0.00*	*0.25*	*0.02*	*0.04*	*0.10*	*0.02*
STD1	40.24	46.92	39.72	36.25	38.54	39.26	39.47	37.58	37.18	34.81	17.56	31.30	77.62	38.77	37.83	38.74	38.57	27.10	39.29	38.81	34.23	42.34
1 sigma error	*1.51*	*4.75*	*1.89*	*1.52*	*4.70*	*2.15*	*3.32*	*6.70*	*2.68*	*2.18*	*2.58*	*1.24*	*3.02*	*1.50*	*1.94*	*1.59*	*1.76*	*1.54*	*1.24*	*2.08*	*2.04*	*1.66*
MDL (99% confidence)	*0.13*	*0.82*	*0.07*	*0.20*	*0.26*	*0.21*	*0.73*	*0.04*	*0.34*	*0.13*	*1.20*	*0.04*	*0.04*	*<0.00*	*0.19*	*<0.00*	*0.05*	*0.29*	*0.01*	*0.07*	*0.09*	*0.02*
STD1	40.13	45.19	37.42	34.71	37.30	39.46	38.17	34.31	35.01	35.56	17.48	30.71	76.93	37.73	40.10	38.29	36.66	28.78	38.85	38.74	33.87	42.47
1 sigma error	*1.65*	*5.55*	*2.07*	*1.65*	*5.69*	*2.57*	*3.97*	*7.37*	*3.06*	*2.62*	*3.08*	*1.36*	*3.33*	*1.63*	*2.42*	*1.79*	*1.90*	*1.81*	*1.25*	*2.44*	*2.43*	*1.86*
MDL (99% confidence)	*0.11*	*0.82*	*0.05*	*0.21*	*0.29*	*0.39*	*0.92*	*0.03*	*0.23*	*0.31*	*1.01*	*0.04*	*0.03*	*0.02*	*0.19*	*<0.00*	*0.06*	*0.24*	*0.01*	*0.05*	*0.05*	*0.02*
STD1	41.13	42.67	39.93	36.35	38.45	38.62	38.09	36.79	38.33	37.61	16.04	32.61	80.47	39.11	38.60	40.33	37.61	29.22	39.17	41.10	37.18	44.35
1 sigma error	*1.70*	*5.34*	*2.24*	*1.75*	*5.99*	*2.55*	*4.02*	*8.05*	*3.39*	*2.80*	*2.95*	*1.46*	*3.52*	*1.71*	*2.37*	*1.91*	*1.97*	*1.85*	*1.27*	*2.63*	*2.72*	*1.97*
MDL (99% confidence)	*0.15*	*0.66*	*0.06*	*0.23*	*0.37*	*0.31*	*0.73*	*0.06*	*0.35*	*0.23*	*1.86*	*0.05*	*0.13*	*<0.00*	*0.20*	*<0.00*	*<0.00*	*<0.00*	*0.02*	*0.09*	*0.08*	*0.02*
STD1	39.86	42.36	38.89	34.82	46.79	36.80	35.84	34.82	34.32	33.68	14.46	31.09	76.85	39.06	37.61	37.85	37.69	28.05	38.69	38.16	33.46	43.13
1 sigma error	*1.66*	*5.39*	*2.21*	*1.69*	*7.43*	*2.47*	*3.85*	*7.76*	*3.09*	*2.56*	*2.63*	*1.41*	*3.40*	*1.72*	*2.35*	*1.81*	*1.99*	*1.79*	*1.25*	*2.48*	*2.49*	*1.94*
MDL (99% confidence)	*0.14*	*0.91*	*0.06*	*0.21*	*0.27*	*0.29*	*<0.00*	*0.06*	*<0.00*	*0.42*	*<0.00*	*0.04*	*0.03*	*0.04*	*0.17*	*<0.00*	*<0.00*	*0.42*	*0.02*	*0.05*	*0.10*	*0.02*
STD1	39.50	48.95	38.73	35.82	37.90	37.03	41.93	46.85	37.85	35.91	16.02	31.45	79.41	37.66	37.07	39.07	38.44	28.09	39.01	39.13	35.41	42.54
1 sigma error	*1.98*	*8.36*	*2.84*	*2.19*	*8.34*	*3.30*	*6.19*	*13.89*	*4.60*	*3.57*	*3.93*	*1.76*	*4.32*	*2.05*	*3.04*	*2.37*	*2.56*	*2.23*	*1.34*	*3.34*	*3.55*	*2.37*
MDL (99% confidence)	*0.11*	*0.61*	*0.05*	*0.20*	*0.25*	*0.29*	*0.78*	*0.04*	*<0.00*	*0.31*	*1.05*	*0.04*	*0.04*	*<0.00*	*0.20*	*0.01*	*<0.00*	*0.48*	*0.01*	*0.09*	*0.05*	*0.02*
STD1	39.64	41.05	38.90	35.50	36.95	37.99	39.57	32.75	35.11	35.89	17.30	31.30	78.10	38.35	37.62	38.97	36.52	27.42	38.80	37.29	34.11	42.02
1 sigma error	*2.01*	*7.15*	*2.89*	*2.20*	*8.29*	*3.44*	*5.96*	*9.87*	*4.35*	*3.62*	*4.26*	*1.78*	*4.30*	*2.11*	*3.14*	*2.40*	*2.47*	*2.19*	*1.33*	*3.23*	*3.48*	*2.37*
MDL (99% confidence)	*0.11*	*0.62*	*0.07*	*0.19*	*0.27*	*0.24*	*0.79*	*0.02*	*0.24*	*0.16*	*<0.00*	*0.03*	*0.03*	*0.01*	*0.20*	*<0.00*	*0.06*	*0.24*	*0.02*	*0.07*	*0.04*	*0.02*
STD1	39.25	40.34	37.40	36.22	37.38	37.94	37.66	31.62	34.54	34.60	13.55	32.17	75.52	38.05	46.07	38.44	36.61	30.43	37.92	38.95	35.20	43.11
1 sigma error	*2.02*	*7.16*	*2.83*	*2.28*	*8.54*	*3.50*	*5.80*	*9.68*	*4.37*	*3.56*	*3.49*	*1.85*	*4.22*	*2.12*	*3.91*	*2.41*	*2.51*	*2.46*	*1.31*	*3.43*	*3.66*	*2.47*
MDL (99% confidence)	*0.12*	*0.82*	*0.06*	*0.21*	*0.27*	*0.27*	*1.21*	*0.13*	*0.42*	*0.45*	*1.06*	*0.04*	*0.04*	*0.02*	*0.29*	*<0.00*	*<0.00*	*<0.00*	*0.02*	*0.07*	*0.08*	*0.02*

Analyte Unit	Ba 137	La 139	Ce 140	Pr 141	Nd 146	Sm 147	Eu 151	Gd 157	Tb 159	Dy 163	Ho 165	Er 166	Tm 169	Yb 172	Lu 175	Hf 178	Ta 181	W 182	Pt 195	Pb 208	Th 232	U 238
	ppm	*ppm*	*ppm*	*ppm*	*ppm*	*ppm*	*ppm*	*ppm*	*ppm*	*ppm*	*ppm*	*ppm*	*ppm*	*ppm*	*ppm*	*ppm*	*ppm*	*ppm*	*ppm*	*ppm*	*ppm*	*ppm*
STD1	38.33	35.27	37.90	37.52	35.66	36.95	34.84	37.00	37.60	35.52	37.89	37.56	35.77	39.38	36.83	36.37	37.59	38.12	2.64	38.65	37.69	37.64
1 sigma error	*1.90*	*1.45*	*1.46*	*1.52*	*1.62*	*1.58*	*1.43*	*1.67*	*1.28*	*1.23*	*1.41*	*1.29*	*1.60*	*1.53*	*1.45*	*1.68*	*1.71*	*1.72*	*0.19*	*1.53*	*1.37*	*1.32*
MDL (99% confidence)	*0.09*	*0.00*	*<0.00*	*<0.00*	*0.02*	*<0.00*	*0.01*	*0.04*	*<0.00*	*<0.00*	*<0.00*	*<0.00*	*0.09*	*<0.00*	*<0.00*	*0.02*	*<0.00*	*<0.00*	*<0.00*	*0.01*	*<0.00*	*<0.00*
STD1	38.52	36.63	38.63	37.88	35.51	38.69	35.64	37.11	37.70	35.46	38.67	38.08	37.45	39.82	36.85	35.48	38.20	37.72	2.42	37.95	37.67	36.98
1 sigma error	*1.92*	*1.51*	*1.49*	*1.53*	*1.62*	*1.66*	*1.47*	*1.68*	*1.29*	*1.23*	*1.44*	*1.31*	*1.67*	*1.56*	*1.45*	*1.65*	*1.73*	*1.71*	*0.18*	*1.51*	*1.37*	*1.30*
MDL (99% confidence)	*0.05*	*<0.00*	*<0.00*	*0.01*	*<0.00*	*<0.00*	*<0.00*	*<0.00*	*0.00*	*<0.00*	*<0.00*	*<0.00*	*0.00*	*<0.00*	*0.00*	*<0.00*	*<0.00*	*<0.00*	*<0.00*	*0.01*	*<0.00*	*<0.00*
STD1	39.44	36.57	38.71	38.20	35.64	37.97	36.11	37.48	37.32	35.57	38.75	38.44	37.62	38.06	37.36	38.19	37.14	38.75	2.53	39.01	37.56	37.33
1 sigma error	*1.96*	*1.51*	*1.49*	*1.55*	*1.63*	*1.63*	*1.49*	*1.70*	*1.28*	*1.23*	*1.44*	*1.32*	*1.68*	*1.49*	*1.47*	*1.77*	*1.69*	*1.76*	*0.18*	*1.55*	*1.36*	*1.31*
MDL (99% confidence)	*0.08*	*0.00*	*<0.00*	*0.00*	*<0.00*	*0.02*	*<0.00*	*0.04*	*<0.00*	*<0.00*	*0.00*	*<0.00*	*0.00*	*<0.00*	*<0.00*	*<0.00*	*<0.00*	*<0.00*	*<0.00*	*<0.00*	*<0.00*	*<0.00*
STD1	40.70	34.97	37.79	37.49	34.40	36.82	34.75	36.69	37.42	34.73	37.36	37.52	35.47	38.85	35.98	36.35	36.33	36.37	2.52	38.20	37.43	36.76
1 sigma error	*2.38*	*1.64*	*1.63*	*1.72*	*1.80*	*1.80*	*1.62*	*1.90*	*1.37*	*1.28*	*1.54*	*1.37*	*1.83*	*1.70*	*1.59*	*1.98*	*1.93*	*1.93*	*0.22*	*1.70*	*1.49*	*1.39*
MDL (99% confidence)	*<0.00*	*<0.00*	*0.03*	*0.01*	*<0.00*	*<0.00*	*<0.00*	*0.03*	*<0.00*	*<0.00*	*<0.00*	*<0.00*	*0.00*	*<0.00*	*<0.00*	*<0.00*	*<0.00*	*0.03*	*<0.00*	*0.01*	*<0.00*	*<0.00*
STD1	40.40	36.86	39.61	39.50	37.03	38.54	36.54	39.28	38.47	36.16	39.15	38.60	37.67	40.07	38.31	37.86	39.34	39.11	2.53	39.83	39.09	38.23
1 sigma error	*2.39*	*1.75*	*1.73*	*1.84*	*1.97*	*1.91*	*1.72*	*2.06*	*1.41*	*1.34*	*1.63*	*1.42*	*1.97*	*1.77*	*1.72*	*2.10*	*2.12*	*2.11*	*0.22*	*1.80*	*1.57*	*1.46*
MDL (99% confidence)	*0.05*	*0.01*	*<0.00*	*<0.00*	*<0.00*	*<0.00*	*0.01*	*0.03*	*<0.00*	*<0.00*	*<0.00*	*<0.00*	*0.00*	*<0.00*	*0.00*	*<0.00*	*<0.00*	*<0.00*	*<0.00*	*0.01*	*0.01*	*<0.00*
STD1	40.35	35.75	38.02	37.19	34.61	37.32	36.31	36.78	37.31	35.55	37.90	37.92	36.92	39.43	36.79	36.29	37.19	37.53	2.35	37.94	37.82	37.45
1 sigma error	*2.42*	*1.72*	*1.68*	*1.75*	*1.86*	*1.87*	*1.73*	*1.95*	*1.38*	*1.32*	*1.59*	*1.40*	*1.96*	*1.76*	*1.67*	*2.04*	*2.03*	*2.06*	*0.21*	*1.73*	*1.53*	*1.44*
MDL (99% confidence)	*0.05*	*<0.00*	*0.01*	*<0.00*	*<0.00*	*<0.00*	*<0.00*	*0.04*	*<0.00*	*<0.00*	*<0.00*	*<0.00*	*<0.00*	*<0.00*	*<0.00*	*<0.00*	*0.02*	*<0.00*	*<0.00*	*0.01*	*<0.00*	*<0.00*
STD1	38.34	36.40	38.82	37.85	35.80	37.16	35.49	37.47	37.87	35.53	38.36	38.26	36.93	39.40	37.09	36.32	37.31	37.74	2.64	38.03	37.67	37.03
1 sigma error	*3.03*	*2.21*	*2.12*	*2.25*	*2.46*	*2.35*	*2.13*	*2.53*	*1.61*	*1.52*	*1.96*	*1.63*	*2.52*	*2.18*	*2.10*	*2.69*	*2.65*	*2.71*	*0.32*	*2.16*	*1.84*	*1.68*
MDL (99% confidence)	*0.07*	*<0.00*	*<0.00*	*<0.00*	*<0.00*	*<0.00*	*0.01*	*0.04*	*<0.00*	*<0.00*	*<0.00*	*<0.00*	*<0.00*	*<0.00*	*0.00*	*<0.00*	*<0.00*	*<0.00*	*<0.00*	*0.01*	*<0.00*	*<0.00*
STD1	38.61	35.80	37.94	37.80	35.53	38.38	35.25	36.83	37.22	35.49	38.46	37.73	36.76	38.71	36.89	36.86	37.89	38.71	2.48	39.01	37.48	37.56
1 sigma error	*3.10*	*2.21*	*2.10*	*2.28*	*2.48*	*2.46*	*2.15*	*2.52*	*1.60*	*1.53*	*1.99*	*1.62*	*2.55*	*2.17*	*2.11*	*2.77*	*2.74*	*2.83*	*0.30*	*2.25*	*1.85*	*1.72*
MDL (99% confidence)	*<0.00*	*<0.00*	*<0.00*	*<0.00*	*<0.00*	*<0.00*	*<0.00*	*0.03*	*0.00*	*<0.00*	*0.01*	*<0.00*	*<0.00*	*<0.00*	*0.00*	*<0.00*	*<0.00*	*<0.00*	*<0.00*	*0.02*	*<0.00*	*<0.00*
STD1	38.86	35.36	38.19	38.30	35.12	38.65	34.82	35.77	37.01	34.73	38.27	38.41	36.58	38.94	36.50	36.52	37.82	38.94	2.40	37.45	37.99	36.87
1 sigma error	3.18	2.21	2.14	2.34	2.49	2.51	2.15	2.49	1.61	1.51	2.01	1.67	2.58	2.22	2.12	2.80	2.78	2.89	0.30	2.19	1.90	1.71
MDL (99% confidence)	*0.10*	*0.01*	*<0.00*	*<0.00*	*0.03*	*<0.00*	*<0.00*	*0.02*	*<0.00*	*<0.00*	*<0.00*	*0.01*	*<0.00*	*0.03*	*0.00*	*<0.00*	*<0.00*	*<0.00*	*0.02*	*0.01*	*<0.00*	*<0.00*

2.7.1 A statistical approach of the LA-ICP-MS data collection

The correlation analysis of the LA-ICP-MS data collection along with the WD-XRF dataset for the major elements, the ICP-OES in the case of Au concentration (see: **Chapter 3.2.3**) and the QXRD results (see: **Chapter 3.2.1**), was applied to study the relationship among different datasets. In particular, despite the relatively low number of the studied HMWI BASH samples (*n*=8) potentially yielding uncertainties, the principal was to determine the degree to which an element might be positively or negatively correlated with another or, even, with the amorphous matrix (e.g., Saravanan & Ramesh, 2024 and references therein). The statistical analysis was performed using the MS Excel software package.

2.8 Scanning Electron Microscopy – Energy Dispersive X-ray Spectroscopy (SEM-EDS)

Details back-scattered imaging (BSE) for the textural and morphological observation and the chemical composition in microscale, were obtained by means of scanning electron microscopy (SEM) on samples' surfaces. For the SEM-BSE observations and the EDS analysis, of the HMWI BASH raw sample and its size fraction samples, a PHILIPS XL30 FEG SEM equipped with an EDAX energy dispersive X-ray spectroscopy (EDS) detector was utilized. The instrument is located in the electron microscopy laboratory of KU Leuven, Department of Materials Engineering. The SEM-EDS experiments were performed under high vacuum (15 and 20 kV) and a working distance of 10 mm. Point analyses on specific micro-domains, previously observed by BSE, were done (i.e., standardless analysis). A small amount of each powdered sample was embedded into an epoxy resin. The resin was left to harden overnight. The surface of the resin was grounded and polished in the grinding and polishing laboratory of the MTM/KUL. All the specimens were carbon coated in order to reduce e-beam damage due to charging effects, making the surface electrically conductive.

2.9 Mix designs towards the production of the autoclaved bricks

The valorisation of the studied HMWI BASH material has been performed by applying six (6) different formulations following three (3) mix design (**Table 2**) toward to the production of sustainable pressed autoclaved bricks (**Figure 2**). Each formulation refers to the incorporation of a different sample from the HMWI BASH material provided by "APOTEFROTIRAS SA", i.e. (a) the HMWI BASH raw sample and (b) the 1:1 mixture of the HMWI BASH finest fractions of -0.500+0.250mm and -0.250mm. The finest fractions were used due to their relatively lower amorphous and higher gehlenite content (see: **Chapter 3**), for comparison. Two sets of autoclaved bricks per formulation were produced.

As much as HMWI BASH material was utilized each time (i.e., 60 wt.%); same for all formulations compared. The **IP100** mix design refers to an inorganic polymer (IP) that contains

HMWI BASH material (60 wt.%) as a supplementary cementitious material (SCM), acting as binder. The **IP_MK** mix design refers to an IP that contains HMWI BASH material (60 wt.%) and metakaolin / MK (10 wt.%), both as SCM, acting as binders, too. The **BLD** mix design refers to a blended cement, containing HMWI BASH material (60 wt.%) as SCM and ordinary Portland cement / OPC (10 wt.%), both as binders. All the aforementioned mix designs incorporate M31 and M34 grade quartz sand as aggregates. A Na-silicate solution, with a Na/Si molar ratio of 1.6 and a water content of 65%, was used as an activator for both inorganic polymers (IPs). For the **BLD** mix design, tap water was used (**Table 2**).

Table 2: Six different formulations, following the three mix design, utilizing a different sample each time from the HMWI BASH material (i.e., the raw sample and the 1:1 mixture of its finest fractions of -0.500+0.250mm & -0.250mm). Two sets of cubic bricks per formulation were produced.

			Inorganic Polymer				Blended Cement	
Mix Design →			**IP100**		**IP_MK**		**BLD**	
Formulation →			**IP100_R**	**IP100_F**	**IP_MK_R**	**IP_MK_F**	**BLD_R**	**BLD_F**
Binders	**SCMs**	**HMWI BASH**	*raw sample*	*1:1 mixture finest fractions*	*raw sample*	*1:1 mixture finest fractions*	*raw sample*	*1:1 mixture finest fractions*
			60	60	60	60	60	60
		MK	-	-	10	10	-	-
		OPC	-	-	-	-	10	10
	Aggregates	**M31**	20	20	15	15	15	15
		M34	20	20	15	15	15	15
Total			*100*	*100*	*100*	*100*	*100*	*100*
Liquids (L/S=0.175)			Na-silicate (1.65NS65)		Na-silicate (1.65NS65)		Tap Water	

The binders and aggregates of the mix designs and related formulations were mixed with the respective solutions (liquids) in an EIRICH EL1 mixer to produce a compressible wet powder (see: left photo of **Image 7**). The wet powder was then inserted in the 4x4x4 cm metallic mold of a PAUL WEBER hydraulic press (see: central photo of **Image 7**). The pressing force applied on the wet powder was 35 kN (~21 MPa) for 60 seconds.

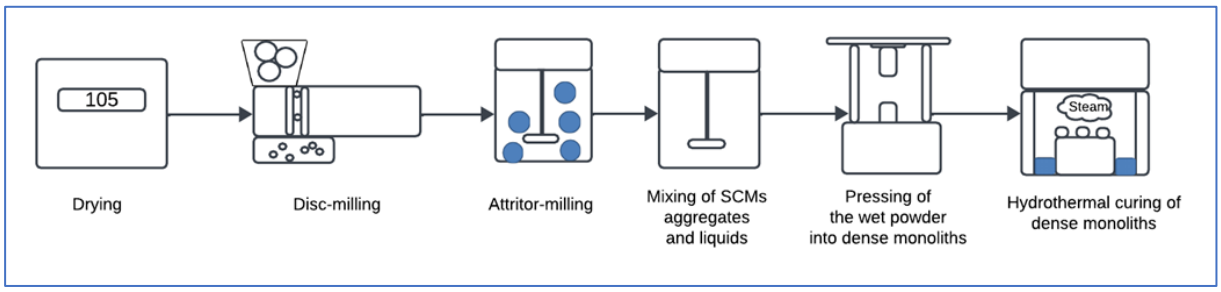

Figure 2: A typical flowchart for the autoclaved bricks production process during the present thesis.

The pressed cubic bricks were placed in a PARKER AUTOCLAVE ENGINEERS autoclave for 24 hours to be cured in hydrothermal conditions (see: right photo of **Image 7**). The temperature was set at 220 ^{o}C corresponding to an internal steam pressure of 23.2 bars. After the completion of the curing, the dense monoliths were placed in a MEMMERT drying oven at 70 ^{o}C for 24 hours. The final products were assessed in terms of their compressive strength using an INSTRON 5985 hydraulic press. The pressing rate applied to its 250 kN load cell was 2 mm/min. The crystalline components of the produced dense monoliths were studied by means of PXRD in order to understand their mechanical properties.

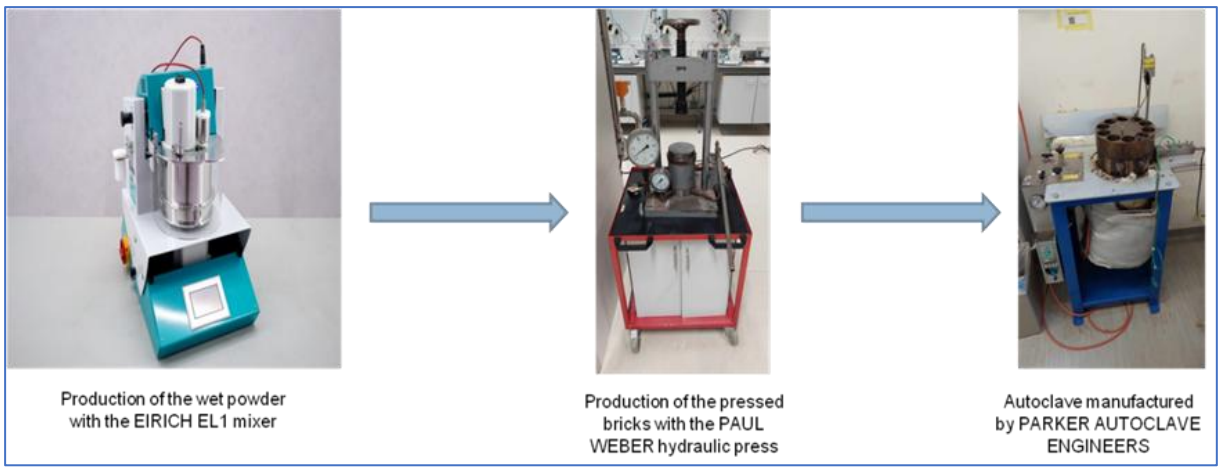

Image 7: Process for the production of autoclave bricks.

2.10 Leaching experiments for the autoclaved bricks (EN 12457/2)

According to EN 12457/2 standards, leaching tests on the autoclaved bricks were carried out, in order to study any leakage of heavy metals from the material toward to the environment. During this process, 1 g of dried material with a particle size <4 mm was immersed in small bottles with 10 g of nano-pure water. The bottles were left to shake on a shaking table for 24 hours. The leachates were filtered by a 10 μm filter and analyzed by ICP-OES to determine the potential release of heavy metals to the environment.

3 RESULTS & DISCUSSION

3.1 Determination of particle size distribution of HMWI BASH samples

Using a series of ASTM Test sieves, the studied HMWI BASH raw sample was sieved in order to create significant fractions of +8mm, -8+4mm, -4+2mm, -2+1mm, -1+0.500mm, -0.500+0.250mm and -0.250mm, respectively. The reason was to study whether or not sieving is a necessary tool for improved building material performance. To this trajectory, the mass distribution (see: **Table 3** and left diagram of **Figure 3**) and the particle size analysis (see: **Table 3** and right diagram of **Figure 3**) of the HMWI BASH material after sieving and before milling (see: **Chapter 3.4**) were studied. Furthermore, a detailed chemical and mineralogical analysis of the raw sample and its fractions was applied (see: **Chapters 3.2 & 3.3**), in order to investigate the distribution of crystalline compounds, the heavy metals partitioning, and reactivity throughout the fractionated samples.

Table 3: Mass distribution of the HMWI BASH raw sample among sieving fractions using ASTM Test sieves.

Sieve *(mm)*	Sieve size *(mm)*	Mean size *(mm)*	Mass *(g)*	Mass *(%)*	Mass passing *(%)*
+8	8	12	1394,2	11,9	88,1
-8+4	4	6	2381,0	20,3	67,8
-4+2	2	3	2764,4	23,6	44,2
-2+1	1	1,5	1778,4	15,2	29,0
-1+0.500	0,5	0,75	1034,4	8,8	20,2
-0.500+0.250	0,25	0,375	794,3	6,8	13,4
-0.250		0,125	1572,6	13,4	0,0
		Total:	**11719,3**	**100,0**	

According to the left diagram of **Figure 3**, the highest mass of the studied HMWI BASH sample concentrated in the coarser fractions with a particle size of >2 mm. In particular, the highest retained mass percentages are observed in the -4+2 and -8+4 fractions, indicating that almost half of the material (i.e., 43.9%) is within the mean size range of 3-6 mm. Nevertheless,

finer particles (mean size of 0.125 mm) contribute a significant mass percentage (13.4%), highlighting the presence of this size range material in the studied HMWI BASH sample. The mass is distributed over a wide range sizes, signifying a broad particle size distribution rather than a uniform one.

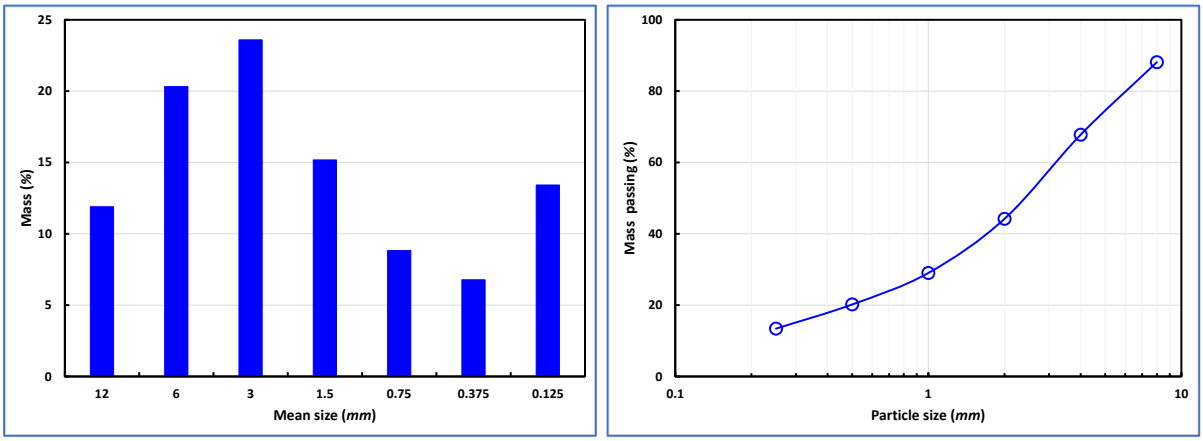

Figure 3: Mass distribution (*left diagram*) and particle size (*right diagram*) of the HMWI BASH raw sample among sieving fractions (**Table 3**), before milling (see: **Chapter 3.4**).

Moreover, the right diagram of **Figure 3** provides insights into the particle size distribution (PSD) of the material. The curve demonstrates a continuous increase, indicating that the material is well-graded and contains both fine and coarse particles. By the largest sieve size (8 mm), close to 90% of the material has passed through, meaning that the material contains no excessively large particles. The characteristic particle sizes are d_{80} = 6.2 mm and d_{50} = 2.4 mm, where d_{80} represents the 80% passing size and d_{50} the 50% passing size.

3.2 Bulk mineral-chemistry of HMWI BASH samples

3.2.1 Powder quantitative X-ray diffraction (QXRD) results

According to the powder XRD patterns (**Figures 4 & 5**), the studied HMWI BASH raw sample and its fractions (i.e., +8mm, -8+4mm, -4+2mm, -2+1mm, -1+0.500mm, -0.500+0.250mm and -0.250mm) contain both amorphous and crystalline phases. Moreover, the quantitative XRD analysis / QXRD (see: **Table 4**) revealed the distribution of different crystalline phases across the fractions, offering insights into the compositional variability

within the waste material, which is crucial for selecting the optimal fractions for further processing and application in dense monolith production.

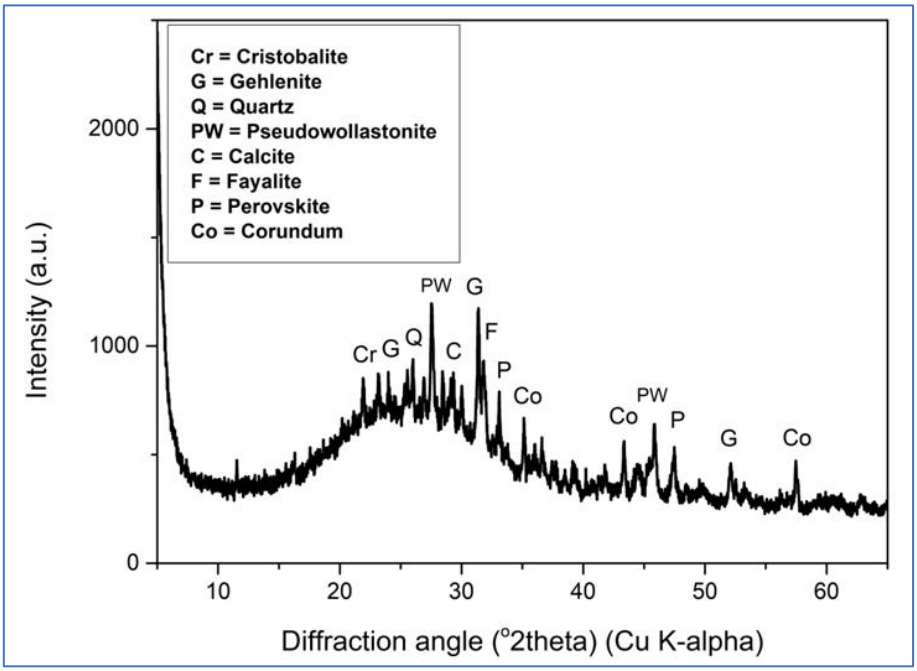

Figure 4: PXRD pattern of the HMWI BASH raw sample (for the abbreviations, see: **Table 4** below).

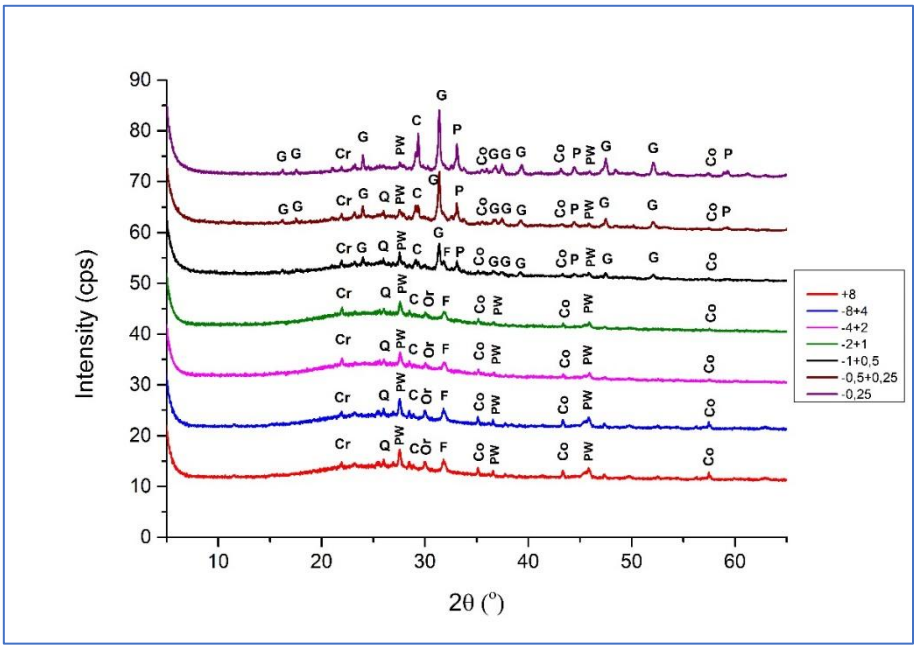

Figure 5: PXRD patterns of the HMWI BASH fractions (i.e., +8mm, -8+4mm, -4+2mm, -2+1mm, -1+0.500mm, -0.500+0.250mm and -0.250mm; for the abbreviations, see: **Table 4** below).

Table 4: Quantitative XRD results of the HMWI BASH raw and fractionated samples using the TOPAS® software package (Faddegon et al., 2020).

Phase (%)	Chemical Formula*[1]	HMWI BASH Abbr*[2]	raw	FRACTIONS						
				+8	+8-4	-4+2	-2+1	-1+0.5	-0.5+0.25	-0.25
Quartz	SiO_2	**Q**	0.53	0.89	0.84	1.02	0.71	1.86	1.79	*nd*
Cristobalite	SiO_2	**Cr**	1.03	1.83	1.77	1.80	2.09	1.26	1.29	1.41
Calcite	$CaCO_3$	**C**	0.76	0.77	0.72	0.70	0.76	1.84	3.68	6.67
Gehlenite	$Ca_2Al(AlSi)O_7$	**G**	5.12	*nd*	*nd*	*nd*	*nd*	9.37	11.31	12.35
Perovskite	$CaTiO_3$	**P**	2.79	*nd*	*nd*	*nd*	*nd*	4.86	7.74	8.23
Pseudo-wollastonite	$CaSiO_3$	**PW**	4.88	8.01	8.19	8.58	7.92	3.79	3.46	2.57
Fayalite	$Fe_2^{2+}SiO_4$	**F**	2.03	0.78	0.64	0.51	0.32	0.25	*nd*	*nd*
Orthoclase	$KAlSi_3O_8$	**Or**	*nd*	4.20	4.89	5.32	4.71	*nd*	*nd*	*nd*
Corundum	Al_2O_3	**Co**	2.16	5.24	5.39	5.35	4.74	3.25	0.98	3.35
Total of crystalline phases			**19.30**	**21.72**	**22.44**	**23.28**	**21.25**	**26.48**	**30.25**	**34.58**
Amorphous	**-**	**-**	**80.70**	**78.28**	**77.56**	**76.72**	**78.75**	**73.52**	**69.75**	**65.42**

Comments

***[1]:** https://rruff.geo.arizona.edu/AMS/amcsd.php

***[2]:** Abbreviations

nd : *not detected*

The amorphous phase is attributed to the rapid cooling after water quenching of the bottom ash melt. A high amorphous content provides a relative larger surface area and higher accessibility of reactive sites, promoting more extensive interactions with surrounding substances (Gartner et al., 2017). This increased reactivity is advantageous under hydrothermal curing conditions, which favor the dissolution and precipitation processes necessary for mineralogical transformation (Wang et al., 2018). Furthermore, as confirmed by mineral processing observations (see: **Chapter 3.1** above), the relatively low crystalline content leads to more effective milling, benefiting both energy consumption and processing time.

The amorphous matrix envelops primarily high-temperature crystalline compounds such as cristobalite (SiO_2), corundum (Al_2O_3), pseudo-wollastonite ($CaSiO_3$), perovskite ($CaTiO_3$) and fayalite ($Fe_2^{2+}SiO_4$). Based on the QXRD analysis (**Table 4**), the grain size of the studied materials seems to dictate the crystalline and amorphous contents. In particular, the distribution of the identified crystalline compounds differs through the individual HMWI BASH fractions. Perovskite and gehlenite are mostly accumulated in the two finest fractions (i.e., -0.500+0.250mm and -0.250mm). Higher amount of fayalite was detected in the raw sample, while its concentration is getting decreased towards the finer fractions of the studied material (see: **Figure 6** below). It is noteworthy to mention that fayalite could not been detected to the two finest fractions (i.e., -0.500+0.250mm and -0.250mm). Based on the bulk chemical analysis by means of WD-XRF (see: **Chapter 3.2.3** below), the total iron content varies throughout the studied material regardless the grain size of the fractions, indicating that iron might also be present in the structure of other phases. The latter can be supported by the following SEM observations and EDS spectral results (see: **Chapter 3.3** and relative figures in the **Appendix**, below), revealing the existence of various (sub)-micro-sized metals-containing particles -also containing heavy metals such as Cr and Cu- embedded into a Si-Na-containing amorphous matrix, that were not previously detected by PXRD. Pseudo-wollastonite seems to be accumulated at higher concentrations in the raw material and the coarser fractions (i.e., +8mm, -8+4mm, -4+2mm and -2+1mm). On the other hand, quartz is present in minor concentrations in most of the fractions, while it was not detected in the finest one. Calcite is mostly accumulated in the finer fractions (i.e., -1+0.500mm and -0.500+0.250mm), but not in the finest one (i.e., -0.250mm).

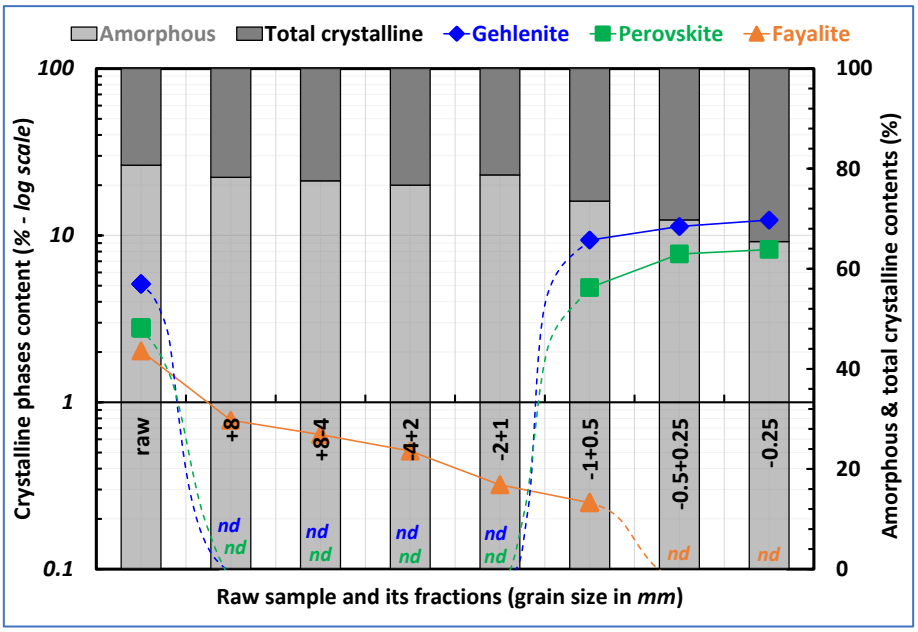

Figure 6: Spider diagram for the total crystalline and amorphous contents (in secondary Y axis) of the HMWI BASH raw and fractionated samples, also showing the distribution of different crystalline phases (i.e., gehlenite, perovskite and fayalite in primary Y axis) across the fractions.

In addition to the amorphous matrix, certain crystalline compounds can contribute to the reactivity of a material in cementitious and/or inorganic polymer systems. The presence of fayalite and pseudo-wollastonite may enhance the reactivity of HMWI BASH, especially under hydrothermal curing conditions. According to Onisei et al. (2015), the reactivity of fayalite in inorganic polymer systems is limited. However, Wang et al. (2024) observed that fayalite ($Fe_2^{2+}SiO_4$) contributes to the formation of C-A-S-H phases, such as ettringite ($Ca_6Al_2(SO_4)_3(OH)_{12}\bullet 26H_2O$), which are responsible for the early strength of cementitious systems.

Wollastonite ($CaSiO_3$) is a calcium silicate phase formed under high temperatures and/or pressures. According to Winnefeld et al. (2023), it facilitates cement hydration due to its filler effect, even though this crystalline phase itself does not exhibit reactivity in an alkaline environment. Wollastonite contributes to the formation of C-S-H crystalline phases, such as tobermorite ($Ca_5Si_6(O,OH)_{18}\bullet 5H_2O$), when it interacts with cement, thereby enhancing the mechanical performance of building materials (Rakhimbaev et al., 2020). Wollastonite also holds potential for carbon sequestration (Yadav & Mehra, 2019). Upon carbonation, it produces quartz and various calcium carbonate polymorphs, e.g. calcite, aragonite, vaterite, etc. (Huijgen et al., 2006). Consequently, the pseudo-wollastonite present in the HMWI BASH

studied material can act as a carbon-sequestering material, while simultaneously improving the mechanical properties of the dense monoliths.

The QXRD results revealed the presence of Al_2O_3 crystals in the form of corundum in the HMWI BASH studied material. Alumina contributes to the formation of C-A-S-H phases in cementitious systems, offering enhanced strength and setting properties. The Al_2O_3 content influences the dissolution rate, with a fraction of Al_2O_3 acting as a network modifier in addition to being a network-forming oxide (Skibsted & Snellings, 2019). Moreover, Al_2O_3 has been identified as a component of Al_2O_3-Fe_2O_3-mono (AFm) phases, which exhibit high sorption capacity for certain ions within the cementitious matrix (e.g., Nedyalkova et al., 2020).

Gehlenite has not been extensively investigated regarding its reactivity in cementitious systems, but it can be present as a minor phase in clinkers, with its abundance varying based on the cooling regime applied during clinker production (Dolenec et al., 2020). Additionally, the interaction of gehlenite with other components in the cement matrix, such as amorphous silica from fly ash, has been suggested to lead to the formation of gismondine / $Ca_2Al_4Si_4O_{16}•9H_2O$ (Vichan et al., 2013).

Perovskite does not exhibit reactivity but holds potential as a heavy metal carrier, contributing to the immobilization of potentially hazardous elements and acting as a secondary source for metal recovery (Gamaletsos et al., 2016). The SEM-EDS investigation (see: **Chapter 3.3** and related figures in the **Appendix**, below) confirmed that perovskite crystals are enveloped in the amorphous matrix of HMWI BASH and accumulate heavy metals.

In conclusion, the studied HMWI BASH raw sample and its coarser fractions contain a greater proportion of amorphous material, while crystalline phases -mainly gehlenite- are mainly concentrated in the finer fractions. The aforementioned compositional differentiation illustrated in the above spider diagram (**Figure 6**) was crucial in selecting suitable fractions for dense monolith manufacturing. Specifically, the HMWI BASH raw sample and its 1:1 mixture of the -0.500+0.250mm and -0.250mm finest fractions were utilized to assess whether this variation in mineralogy affects the resulting mechanical properties of the monoliths.

3.2.2 Thermal behavior (TGA-DSC) results

The thermal characterization of the studied HMWI BASH raw material and its fractions (i.e., +8mm, -8+4mm, -4+2mm, -2+1mm, -1+0.500mm, -0.500+0.250mm and -0.250mm), by means of TGA-DSC simultaneous analysis was performed at a temperature range of 25-900 °C. The calculated loss on ignition (LOI) of the studied materials is presented in **Table 5**. The finer fractions present higher LOIs, due to their higher content in calcite, which slightly decomposes after 600 °C and rapidly above 750 °C into CaO and CO_2 (e.g., Karunadasa et al. 2019).

Table 5: Loss on ignition (LOI) of the studied HMWI BASH raw sample and its fractions.

Samples	**Raw**	**Fractions** *(in mm)*						
		+8	**-8+4**	**-4+2**	**-2+1**	**-1+0.5**	**-0.5+0.25**	**-0.25**
LOI (%)	1.41	0.91	0.11	0.41	0.77	2.73	4.32	7.37

The TGA-DSC results of the HMWI BASH (**Figure 7**) confirmed the PXRD data, even though some data cannot be confirmed due to the extensive background noise of the PXRD patterns, originating from the high amorphous content. According to Essam et al. (2023), the endothermic peaks between 200-300 °C can correspond to the thermal disintegration of calcium and aluminum silicate phases -in this case- gehlenite. The endothermic peaks just above the 600 °C confirm the presence of carbonated phases (Agioutanti et al., 2019).

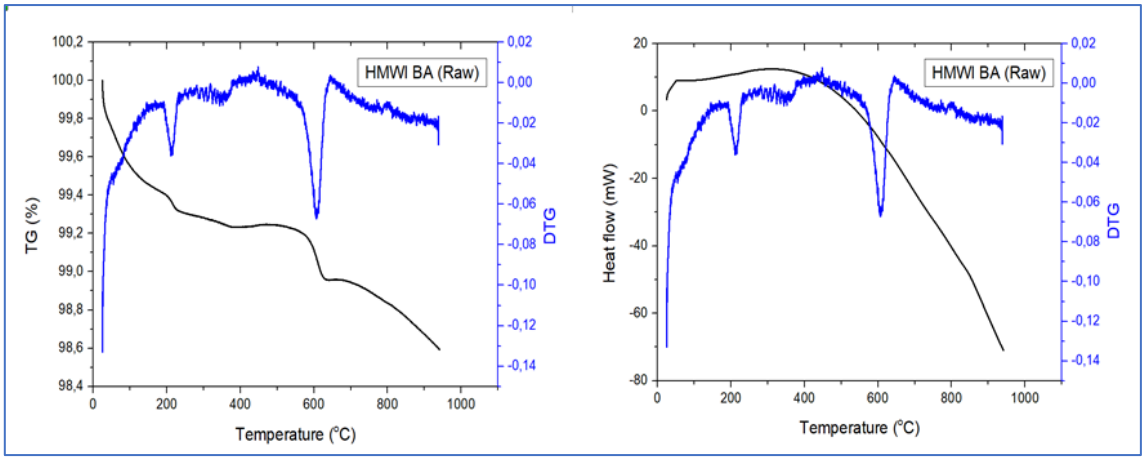

Figure 7: Simultaneous TG-DTG (left image) and the heat flow (right image) curves of the studied HMWI BASH raw material.

The TGA-DSC curves of the studied fractionated samples (**Figures 8-14**) are in line with the PXRD data mentioned above. It is noteworthy that the corresponding curves (**Figures 8-14**) differ from the TGA-DSC curve of the raw sample (**Figure 7**). This might be affected by the elemental and/or organic carbon content due to the HMWI BASH origin (e.g., Kougemitrou et al. 2011; Anastasiadou et al. 2012), and also influenced by the presence of the Ca- and/or Al-containing phases (e.g., Rocca et al. 2013). In particular, the exothermic peaks at above 600 °C that were found in some of the TGA-DSC curves of the coarser fractions (see: **Figures 8-11**), especially in the -4+2 and less in the -8+4mm and -2+1mm fractions (**Figures 9-11**), may correspond to a phase transformation that emit heat, even if PXRD data do not provide further information about the existence of such phase. According to the literature (e.g., Marinkovic et al. 2009), such exothermic peaks might be attributed to the unburned elemental and/or organic carbon combustion incorporated either in amorphous matrix and/or in crystalline compounds. The higher carbon incorporation in the amorphous matrix the lower temperature exothermic peaks can be yielded. Besides, the observed differences in the shape of the exothermic peaks between the studied fractions (i.e., +8mm, -8+4mm, -4+2mm and -2+1mm; see: **Figures 8-11**), most probably might be ascribed to the variation of the amorphous-to-crystalline phase ratio (Marinkovic et al. 2009). On the other hand, the absence of such intense exothermic peaks and, at the same time, the presence of a small endothermic peak at around 600 °C in the finest fractions (-1+0.500mm, -0.500+0.250mm and -0.250mm; see: **Figures 12-14**), most probably is due to the existence of carbonates and less amorphous content, in line with the QXRD results (see: **Table 4** above).

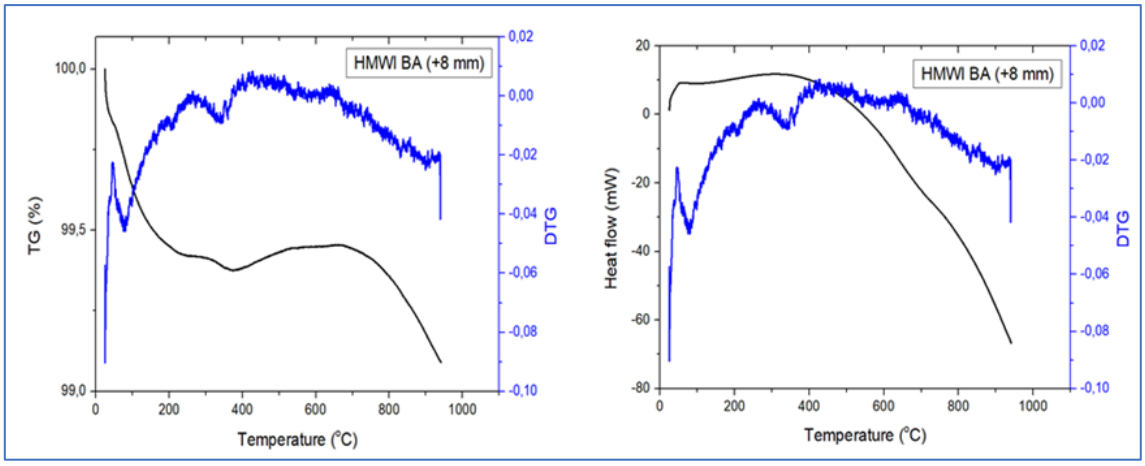

Figure 8: Simultaneous TG-DTG (left image) and the heat flow (right image) curves of the studied +8mm fraction (mean grain size of 12 mm) of the HMWI BASH material.

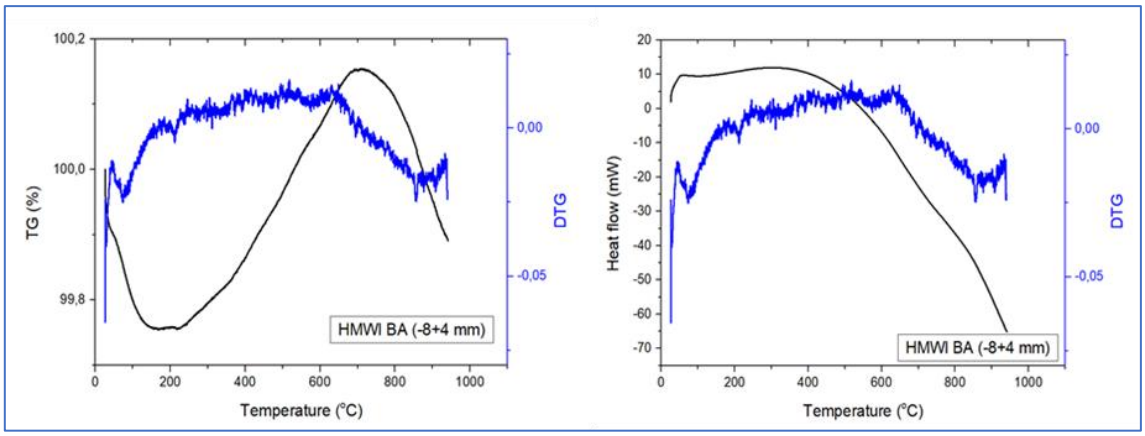

Figure 9: Simultaneous TG-DTG (left image) and the heat flow (right image) curves of the studied -8+4mm fraction (mean grain size of 6 mm) of the HMWI BASH material.

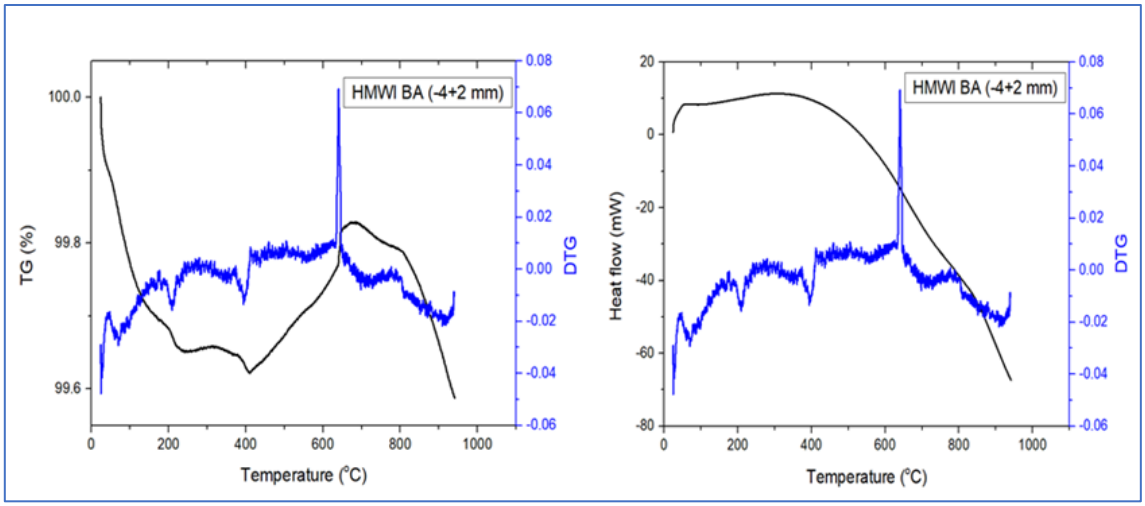

Figure 10: Simultaneous TG-DTG (left image) and the heat flow (right image) curves of the studied -4+2mm fraction (mean grain size of 3 mm) of the HMWI BASH material.

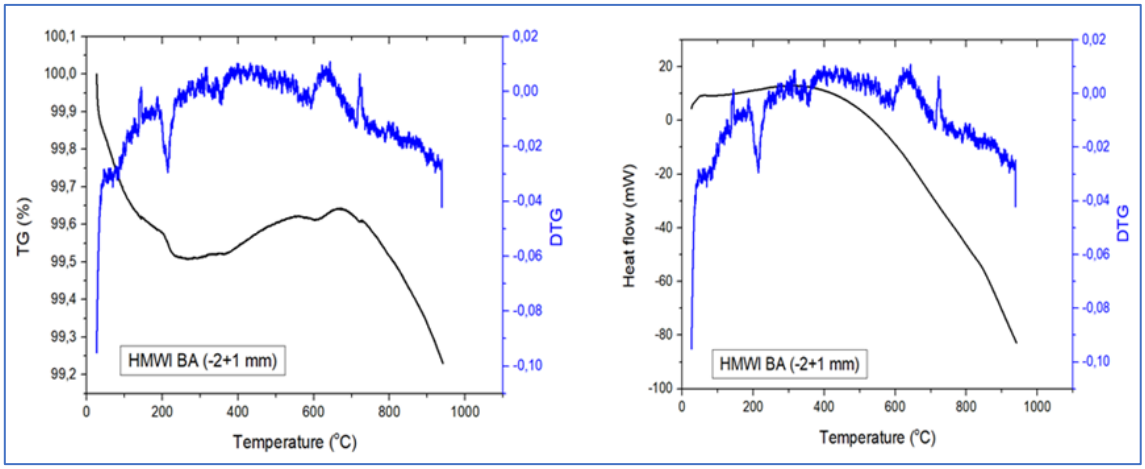

Figure 11: Simultaneous TG-DTG (left image) and the heat flow (right image) curves of the studied -2+1mm fraction (mean grain size of 1.5 mm) of the HMWI BASH material.

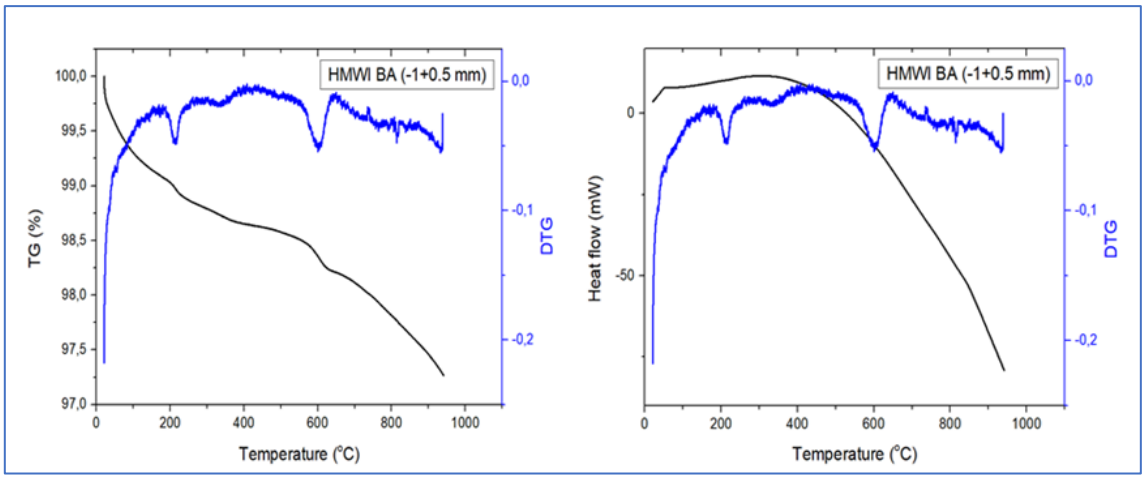

Figure 12: Simultaneous TG-DTG (left image) and the heat flow (right image) curves of the studied -1+0.500mm fraction (mean grain size of 0.5 mm) of the HMWI BASH material.

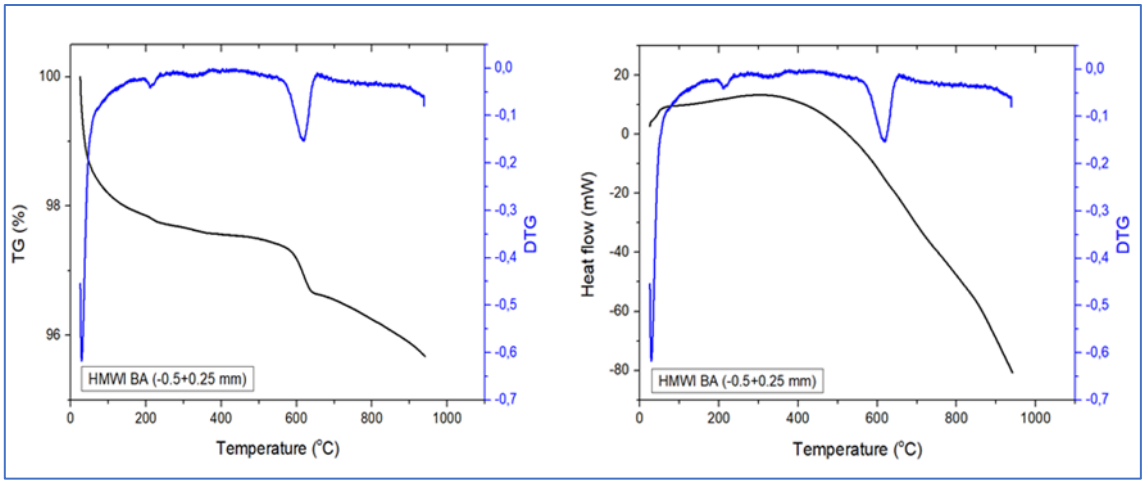

Figure 13: Simultaneous TG-DTG (left image) and the heat flow (right image) curves of the studied -0.500+0.250mm fraction (mean grain size of 0.375 mm) of the HMWI BASH material.

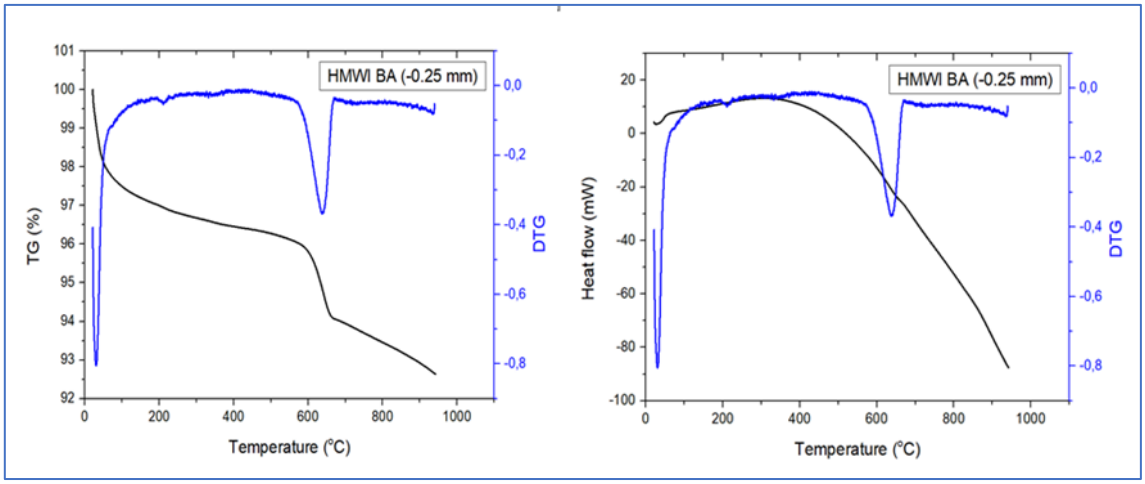

Figure 14: Simultaneous TG-DTG (left image) and the heat flow (right image) curves of the studied -0.250mm fraction (mean grain size of 0.125 mm) of the HMWI BASH material.

3.2.3 Whole-rock major & trace elements analysis

The chemical analysis for major and trace elements by means of WD-XRF, ICP-OES and Laser Ablation ICP-MS (LA-ICP-MS) are shown in the **Table 6**. The bulk chemical composition of the studied HMWI BASH raw sample is predominantly composed of Si, Ca, Al, and Na. These elements are the main constituents of certain crystalline compounds found by QXRD, such as gehlenite ($Ca_2Al(AlSi)O_7$), pseudo-wollastonite ($CaSiO_3$), corundum (Al_2O_3) and other silicate phases, while Si and Na are strongly correlated with the amorphous matrix, as well.

Table 6: Major and trace element concentrations of the HMWI BASH raw sample and its corresponding fractions.

Analyte Unit	RAW	FRACTIONS *(in mm)*						
		+8	-8+4	-4+2	-2+1	-1+0.5	-0.5+0.25	-0.25
wt.%								
SiO_2	53.08	59.18	62.62	61.81	62.67	51.35	42.16	30.11
Al_2O_3	13.80	11.84	9.35	10.44	8.04	11.34	13.05	13.08
Fe_2O_3(T)	1.41	3.03	1.35	1.57	1.66	1.90	2.41	3.92
MnO	0.20	0.00	0.09	0.04	0.05	0.02	0.03	0.04
MgO	1.70	1.40	1.45	1.19	1.18	2.16	2.51	3.37
CaO	18.52	14.26	15.73	15.01	16.65	20.77	26.02	31.17
Na_2O	6.44	7.24	7.26	7.62	6.99	5.50	4.12	3.29
K_2O	0.51	0.50	0.65	0.59	0.66	0.44	0.74	0.31
TiO_2	1.54	0.99	0.88	0.92	1.04	1.65	3.24	4.70
P_2O5	0.47	0.36	0.30	0.21	0.19	0.53	0.77	1.15
Cr_2O_3	0.12	0.23	0.11	0.13	0.12	0.31	0.10	0.21
LOI	1.41	0.91	0.11	0.41	0.77	2.73	4.32	7.37
Total	**99.20**	**99.94**	**99.90**	**99.94**	**100.02**	**98.70**	**99.47**	**98.72**
ppm								
Sc	3.0	2.6	6.7	4.9	3.5	bdl	3.9	8.2
V	288.2	41.9	34.0	29.5	30.6	56.5	53.0	54.5
Co	15.8	25.3	7.1	9.9	8.5	19.2	23.8	36.6
Ni	226.1	762.0	185.8	248.0	232.8	377.5	446.0	695.7
Cu	571.4	1825.1	660.9	834.4	493.8	446.4	665.8	1191.8
Zn	448.2	341.4	239.6	249.9	238.4	725.6	1137.5	1421.7
Ga	61.4	62.1	62.4	51.1	52.2	60.8	63.6	74.1
Ge	8.1	2.6	bdl	6.1	5.3	bdl	4.7	13.4
As	21.1	20.1	29.8	22.7	16.2	8.1	11.4	22.0
Se	10.6	bdl	bdl	2.7	7.0	8.0	bdl	27.0
Rb	14.6	9.6	7.3	7.4	6.2	10.0	7.9	7.3
Sr	262.0	219.8	211.0	240.4	204.6	336.6	430.9	578.7
Y	12.4	10.0	7.5	8.3	7.7	10.7	14.4	18.2
Zr	250.1	249.4	274.2	323.6	196.7	345.3	340.2	410.9
Nb	427.9	25.9	15.2	11.6	11.4	18.1	29.1	39.1
Mo	409.2	45.8	28.2	23.2	23.7	26.7	31.4	39.7
Cd	bdl	2.0	2.8	bdl	1.2	bdl	1.9	2.7
In	0.6	7.1	7.7	1.8	0.7	2.5	2.1	0.3
Sn	34.6	83.5	28.4	103.2	19.0	18.3	32.4	88.1
Sb	30.0	25.8	14.7	15.8	13.1	28.4	32.2	73.8

Table 6: continued.

Analyte Unit	RAW	FRACTIONS *(in mm)*						
		+8	-8+4	-4+2	-2+1	-1+0.5	-0.5+0.25	-0.25
ppm								
Cs	2.8	0.9	1.8	0.5	0.7	0.7	0.7	0.8
Ba	3009.6	3288.4	3130.2	3172.2	2614.0	3534.1	3344.0	3677.9
La	8.7	7.5	5.7	6.6	5.6	11.4	19.3	28.7
Ce	96.6	85.4	91.8	86.0	86.3	95.1	90.3	85.8
Pr	1.7	1.4	1.3	1.4	1.2	2.6	3.4	5.4
Nd	7.7	5.6	4.5	5.1	4.6	13.6	15.3	22.1
Sm	1.1	1.1	0.7	0.9	0.8	1.5	3.2	3.3
Eu	0.4	0.2	2.6	0.5	0.2	0.3	0.5	0.6
Gd	76.5	81.2	44.7	37.7	42.7	85.2	166.0	284.2
Tb	0.2	0.1	0.3	0.1	0.1	0.2	0.6	0.6
Dy	0.9	1.3	0.8	0.6	0.7	1.5	2.1	2.6
Ho	0.3	0.2	0.1	0.1	0.2	1.0	0.4	1.7
Er	2.2	1.3	1.1	0.6	0.4	0.9	0.9	1.5
Tm	0.1	0.1	0.1	0.1	0.1	0.1	0.3	0.3
Yb	3.2	1.6	0.7	1.5	0.6	1.3	1.6	1.6
Lu	0.3	1.0	0.1	0.2	0.3	0.1	0.4	0.2
Hf	6.0	6.8	7.1	9.7	8.7	6.9	10.0	12.4
Ta	4.8	4.9	2.2	2.2	2.3	2.1	3.4	3.6
W	942.6	26.1	18.4	11.7	10.7	16.3	28.4	37.6
Pt	5.6	7.6	5.3	6.3	2.9	5.3	2.4	4.5
Pb	9.0	4.6	5.3	4.5	3.3	5.1	3.8	7.9
Th	3.7	2.8	2.8	2.3	2.1	5.1	8.0	10.6
U	1.1	5.0	1.1	0.7	1.2	1.6	2.2	4.7
ppm								
Au	15.0	13.0	13.0	10.0	11.0	9.0	10.0	8.0
ppm								
ΣLREE [(1)]	192.8	182.4	151.3	138.2	141.3	209.7	298.0	430.2
ΣHREE [(1)]	19.4	15.6	10.6	11.5	10.1	16.0	20.8	26.7
ΣREE [(1)]	215.2	200.6	168.6	154.5	155.0	225.6	322.8	465.1

Note:

[(1)] The elements comprise the LREE and HREE groups are arbitrary defined (Mariano & Mariano, 2012; Gambogi, 2013; Zepf, 2013). The ΣLREE group includes the lanthanide elements from La through Gd (Gambogi, 2013; Zepf, 2013); The ΣHREE group includes the lanthanide elements from Tb through Lu, including Y (Gambogi, 2013; Zepf, 2013); The ΣREE group comprises of the 15 lanthanide elements including Sc, and Y (Gambogi, 2013; Zepf, 2013).

In particular (**Table 6**), the correlation analysis among different datasets (i.e., LA-ICP-MS, ICP-OES, WD-XRF, QXRD data collections; e.g., Saravanan & Ramesh, 2024 and references therein) revealed that, apart from Si-bearing crystals, silicon is strongly correlated with the amorphous matrix ($R_{(Si,amorphous)}$ of 0.89). This trend is shown in the left diagram of **Figure 15**. Besides, in the case of Na and amorphous relationship, a high positive correlation coefficient was obtained ($R_{(Na,amorphous)}$ of 0.91), revealing that sodium is strongly correlated with the amorphous matrix (see: right diagram of **Figure 15**).

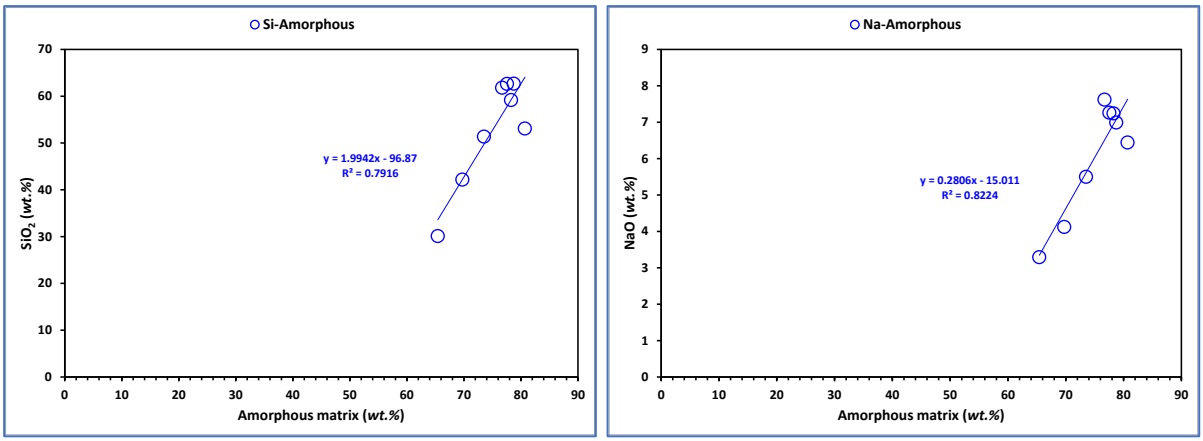

Figure 15: The trendline and the corresponding R^2 value showing the variation of the Si (*left diagram*) and Na (*right diagram*) concentrations (*wt.%*) along with the amorphous content (*wt.%*) in the HMWI BASH raw sample and its fractions (i.e., +8mm, -8+4mm, -4+2mm, -2+1mm, -1+0.500mm, -0.500+0.250mm and -0.250mm).

The correlation analysis revealed that the concentrations of calcium (see: left diagram of **Figure 16**) and aluminium (see: see: right diagram of **Figure 16**) are inversely proportional to amorphous content ($R_{(Ca,amorphous)}$ of -0.92 and $R_{(Al,amorphous)}$ of -0.40, respectively). Moreover, the Ca content is significantly elevated in the finer fractions of the HMWI BASH studied material (see: left diagram of **Figure 17**), while these fractions exhibit less Si content. Sodium is accumulated preferably in the coarser fraction of the material. Low Al content has been measured in the -2+1mm fraction, while both the raw sample and the finest fraction (-0.250mm) contain the highest aluminium amount (see: left diagram of **Figure 17**). This compositional variation, along with the crystallinity of the studied material (see: **Chapter 3.2.1** above), influences the selection process of the HMWI BASH fractions utilized in the production of autoclaved bricks. Moreover, Ca, Al and Si are apparently present in significant Ca-bearing aluminosilicates, Ca-carbonates and Ca-Ti-oxides crystalline phases that have been identified as the abundant phases, such as gehlenite, calcite and perovskite, respectively. None of these crystalline phases are correlated with sodium ($R_{(Na,\ gehlenite)}$ of -0.95, $R_{(Na,\ calcite)}$ of -0.94 and $R_{(Na,\ perovskite)}$ of -0.99, respectively), meaning that Na content decreases while the amount of the aforementioned crystalline phases increases. This is in line with the $R_{(Na,amorphous)}$ value finding, implying that sodium is strongly correlated with the amorphous matrix, only (see: right diagram of **Figure 15**).

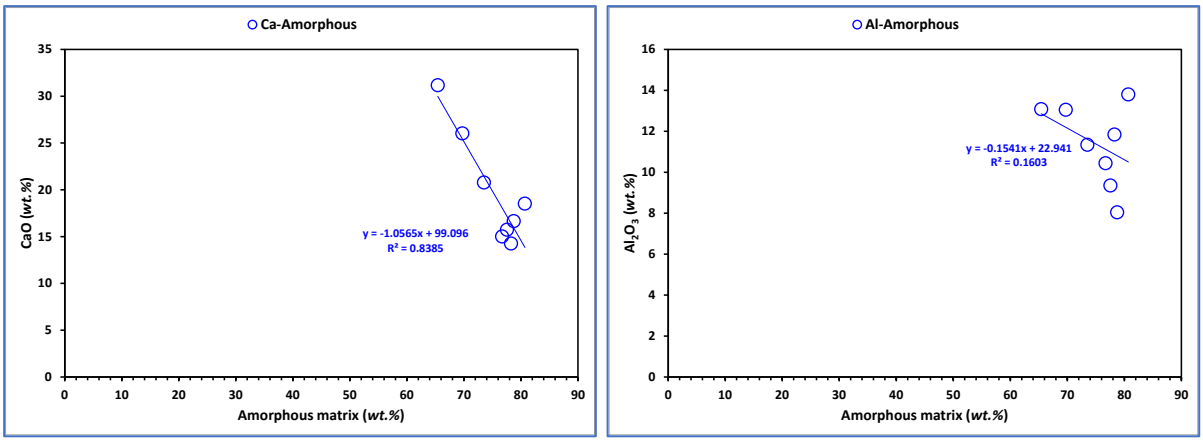

Figure 16: The trendline and the corresponding R^2 value showing the variation of the Ca (left diagram) and Al (right diagram) concentrations (wt.%) along with the amorphous content (*wt.%*) in the HMWI BASH raw sample and its fractions (i.e., +8mm, -8+4mm, -4+2mm, -2+1mm, -1+0.500mm, -0.500+0.250mm and -0.250mm).

Furthermore, other major elements exist in relatively lower concentrations compared to Si, Ca, Al and Na, whereas some of them -such as Fe and Ti- seems to be elevated in the finer fractions (see: right diagram of **Figure 17**). Especially for iron, despite the fact that the no Fe-bearing phase (i.e., fayalite) was detected by QXRD in the finest fractions (see: **Table 4** and **Figure 6**), its concentration found to be inversely proportional to the grain size (see: right diagram of **Figure 17**). On the other hand, the correlation coefficient $R_{(Fe,amorphous)}$ of -0.73 revealed that iron exhibits a strong negative correlation with the amorphous matrix. These findings indicate that -most probably- iron might be incorporated either into other crystalline phases and/or into Fe-containing crystals in (sub)-micro- down to nano-scale, which cannot be detected by PXRD, due to the detection limit of the X-ray diffraction technique. The SEM observations and EDS point analysis (see: **Chapter 3.3** and related figures in the **Appendix**, below) indicate that iron is also associated with fused metals-containing (sub)-micro-sized particles, except for fayalite.

In the case of titanium, it has been observed that the finest fractions contain higher Ti content compared to raw and its coarser fractions (see: right diagram of **Figure 17**), while Ca-Ti-oxide (perovskite) was detected by QXRD in the finest fractions with a grain size of <1 mm (**Table 4**), and also observed by SEM-EDS (see: **Chapter 3.3** and related figures in the **Appendix**, below). This means that titanium is mainly existed in perovskites, but not in amorphous matrix. The latter is in line with the $R_{(Ti,amorphous)}$ value of -0.92 proving that Ti exhibits a strong negative correlation with the amorphous matrix.

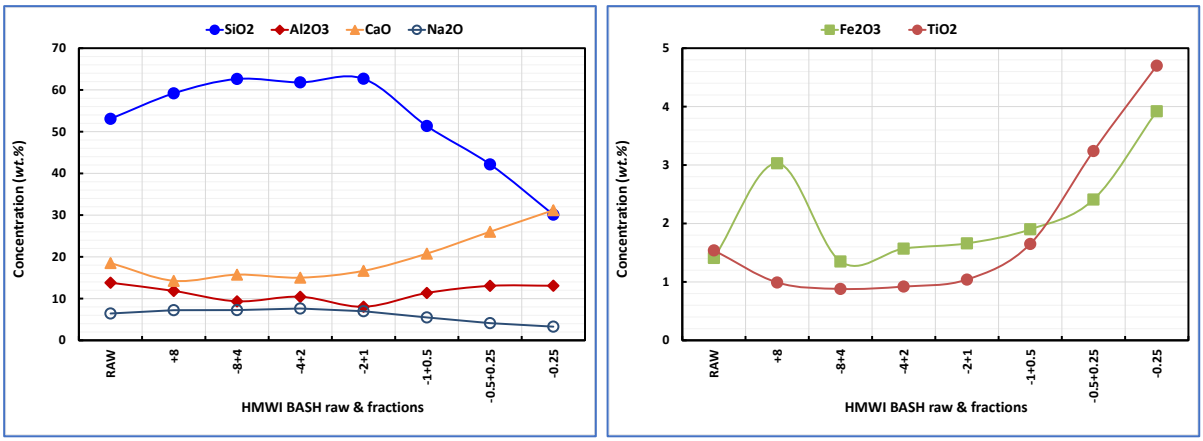

Figure 17: Major elements (Si, Al, Ca, Na: *left diagram*; Fe, Ti: *right diagram*) distribution (*wt.%*) in the HMWI BASH raw sample and its fractions (i.e., +8mm, -8+4mm, -4+2mm, -2+1mm, -1+0.500mm, -0.500+0.250mm and -0.250mm).

Other elements such as magnesium and phosphorus were detected within the amorphous matrix by SEM-EDS, even though they both exhibit a strong negative correlation with the amorphous matrix ($R_{(Mg,amorphous)}$ and $R_{(P,amorphous)}$ values of -0.92 and -0.89, respectively). As long as the QXRD results confirm the absence of distinct P- and Mg-containing crystalline phases in the studied materials, it can be assumed that these elements might be incorporated into (sub)-micro-/nano-crystals that cannot be detected by PXRD. Such crystalline phases were not observed by the conventional SEM-EDS utilized in this thesis.

The LA-ICP-MS analytical spectroscopic technique applied for the identification of the trace elements content of HMWI BASH raw sample and its fractions (**Table 6**), revealed that the studied samples also contain heavy metals and metalloids, some of them being present at relatively elevated concentrations in the finest fractions (e.g., Cr, Cu, Ni, Zn, etc.; see: **Figure 18**), and others being accumulated in smaller quantities, such as Co and Sn (see: left diagram of **Figure 19**), trending to increase their content toward the finer fractions. V and As also exhibit a compositional variation throughout the fractions (see: right diagram of **Figure 19**).

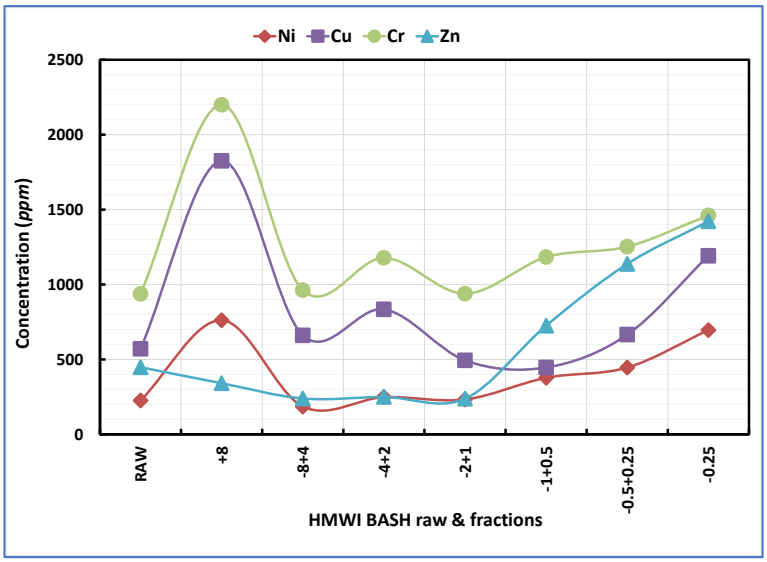

Figure 18: Trace elements (Cr, Cu, Ni and Zn) distribution (*ppm*) in the HMWI BASH raw sample and its fractions (i.e., +8mm, -8+4mm, -4+2mm, -2+1mm, -1+0.500mm, -0.500+0.250mm and -0.250mm).

It can be stated that vanadium has a strong positive correlation with Fe-containing phases ($R_{(V,fayalite)}$ value of 0.94), while its correlation coefficient value implies that weak correlation with the amorphous matrix ($R_{(V,amorphous)}$ of 0.35 is lower than the value of 0.55; e.g., Saravanan & Ramesh, 2024 and references therein). The correlation analysis did not prove any significant interrelationship between chromium and the crystalline compounds detected by QXRD, neither with the obtained amorphous matrix. Moreover, Ni was found to exhibit a strong positive correlation with iron ($R_{(Ni,Fe)}$ of 0.94) as well as with gehlenite ($R_{(Ni,gehlenite)}$ of 0.90) and perovskite ($R_{(Ni,perovskite)}$ of 0.89) crystals. The latter trend stands for zinc ($R_{(Zn,gehlenite)}$ of 0.95 and $R_{(Zn,perovskite)}$ of 0.98) and cobalt ($R_{(Co,gehlenite)}$ of 0.83 and $R_{(Co,perovskite)}$ of 0.85), respectively. This assumption can also be addressed by the high value of correlation coefficient ($R_{(Zn,Ca)}$ = 0.98), implying a strong positive correlation of zinc with calcium. Besides, the value of -0.94 in the case of $R_{(Zn,amorphous)}$ means that zinc is inversely proportional to amorphous matrix. Copper and tin exhibit a medium positive correlation with perovskite ($R_{(Cu,perovskite)}$ of 0.70 and $R_{(Sn,perovskite)}$ of 0.59, respectively), implying that they might be intercorrelated to some extent, while their low R values ($R_{(Cu,amorphous)}$ of -0.15 and $R_{(Sn,amorphous)}$ of -0.23, respectively) most probably indicate no significant relationship of these elements with the amorphous phase. The presence of heavy metals originates from consumables made of stainless steel and other metallic alloys, such as needles, grippers, scalpels, etc. (e.g., Kougemitrou et al., 2011). The SEM/EDS observations revealed (sub)-micro-sized perovskites

embedded into the amorphous matrix carrying heavy elements (see: **Chapter 3.3** and relative figures in the **Appendix**, below) in line with the correlation analysis mentioned above. For the sustainable valorization of HMWI BASH towards building materials, the immobilization of these elements is of major importance.

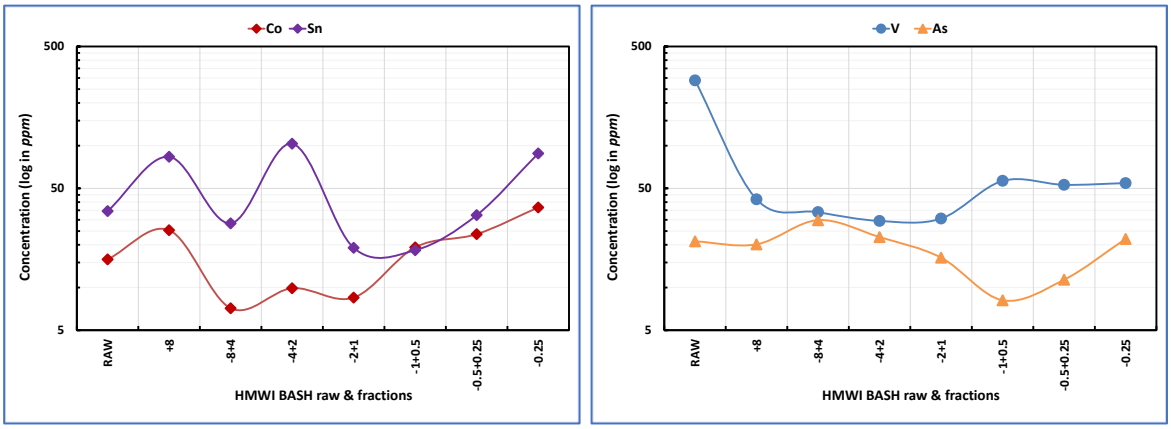

Figure 19: Trace elements (*left diagram*: Co and Sn; *right diagram*: V and As) distribution (*ppm*) in the HMWI BASH raw sample and its fractions (i.e., +8mm, -8+4mm, -4+2mm, -2+1mm, -1+0.500mm, -0.500+0.250mm and -0.250mm).

According to LA-ICP-MS measurements, lead seems to be present in all the studied samples in low concentration (~3-9 ppm), while cadmium has been detected in some of the fraction (~1-3 ppm), only (see: left diagram of **Figure 20**). Indication of a strong positive correlation between Pb and Fe-containing phases is the $R_{(Pb,fayalite)}$ value of 0.92, while the extremely low $R_{(Pb,amorphous)}$ of -0.09 indirectly implies that this heavy metal might not be accumulated into the amorphous matrix. The highest correlation coefficient values of 1,00 that have been estimated for both the intercorrelation of Cd with gehlenite ($R_{(Cd,gehlenite)}$) and perovskite ($R_{(Cd,perovksite)}$) indicate that cadmium might be associated with the aforementioned crystalline compounds. The low-to-medium $R_{(Pb,amorphous)}$ value of -0.42 is an indicator that cadmium has a weak is inversely proportional to amorphous matrix.

As it has been revealed by complementary ICP-OES results, it is noteworthy to mention the presence of gold (Au) in the studied raw material (15 ppm) and in its fractions (8-13 ppm). Gold seems to prefer to be accumulated in the coarser samples, but in finer ones (see: left diagram of **Figure 20**). Apart from the aforementioned noble metal, critical raw materials (CRMs), such as rare earth elements (including 15 lanthanides, Sc and Y; Gambogi, 2013; Zepf, 2013) were detected in the studied samples. It has been revealed that ΣREE content is

significantly increased while the grain size is getting smaller (see: right diagram of **Figure 20**). Gold might be associated with the amorphous phase ($R_{(Au,amorphous)}$ of 0.81) and, perhaps, with Fe-containing crystals ($R_{(Au,fayalite)}$ of 0.85). Its $R_{(Au,perovskite)}$ value of -0.81 indicates that Au and Ca-Ti-oxide crystals exhibit a strong inversely proportional relationship. Besides, radionuclides namely thorium (Th) and uranium (U) were additionally detected in low quantities throughout the fractions. The concentration of these elements seems to be elevated in the finest fractions, compared to those from the coarser fractions, following the ΣREE content (see: right diagram of **Figure 20**).

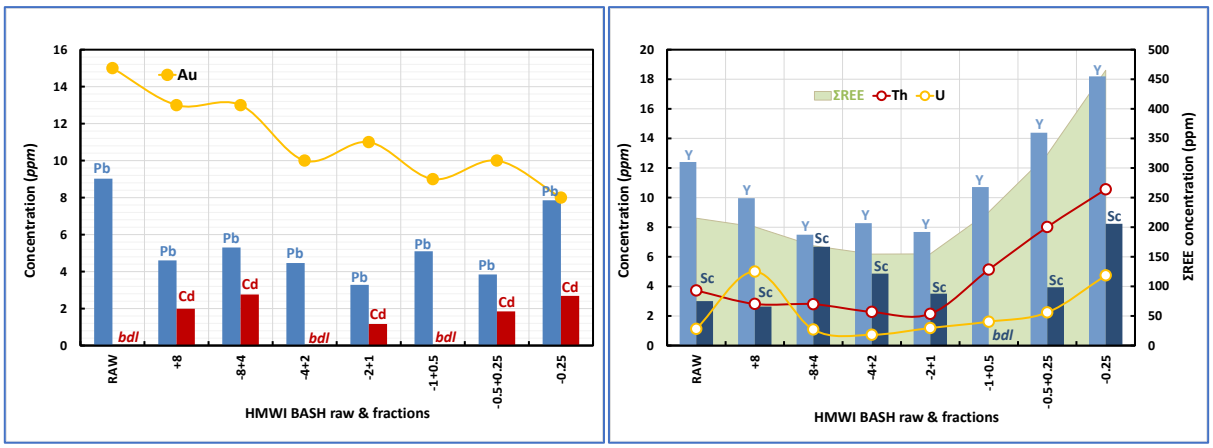

Figure 20: *Left diagram*: trace elements (Pb and Cd) distribution along with Au content (ppm) in the HMWI BASH raw sample and its fractions (i.e., +8mm, -8+4mm, -4+2mm, -2+1mm, -1+0.500mm, -0.500+0.250mm and -0.250mm*). Right diagram*: Rare Earth Elements / REEs (ΣREE) and actinides (namely, Th and U) distribution along with Au content (ppm) in the HMWI BASH raw sample and its. ΣREE stands for the total amount of 15 lanthanides including Sc and Y (Gambogi, 2013; Zepf, 2013).

3.3 Investigation of HMWI BASH samples in microscale

Apart from the crystalline phases detected by PXRD (see: **Chapter 3.2.1** above), the SEM-BSE observations and their corresponding EDS spectral results of the studied HMWI BASH samples at the microscale proved the presence of various metals-containing (sub)-micro-sized particles embedded in a Si-Na-containing amorphous matrix (**Figures 21-22**). The EDS analysis -that is summarized in the **Appendix**- contributed to the understanding of metals partitioning within the amorphous and crystalline phases at microscale. Glassy-like Al-Si-Ca-bearing particles that have been observed in the finest fraction (see: BSE image **a** of **Figure 21**, and the EDS spectra of **spots 1 & 2** in the **Figure A1** in **Appendix**) and Ca-containing Si-particles mostly present in the coarser fractions (see: BSE images **c & d** of **Figure 21**, and the EDS spectra of

spots 2 & 3 in the **Figure A3** and those of **spots 2 & 3** in the **Figure A4** in **Appendix**) have been detected within the amorphous matrix. As it has been confirmed by QXRD, the latter Si-rich particles might be corresponded either to Si-oxides (namely quartz and cristobalite) and/or to pseudo-wollastonite (see: **Chapter 3.2.1**). If they correspond to pseudo-wollastonite, the intense Si peak might be attributed both to $CaSiO_3$ crystal and to the amorphous matrix. In line with the strong positive correlation of silicon and sodium with the amorphous, proved by the statistical approach applied herein, it can be stated that an amount of Si peak and the Na peak both can be attributed to the matrix (see: **Chapter 3.2.3**).

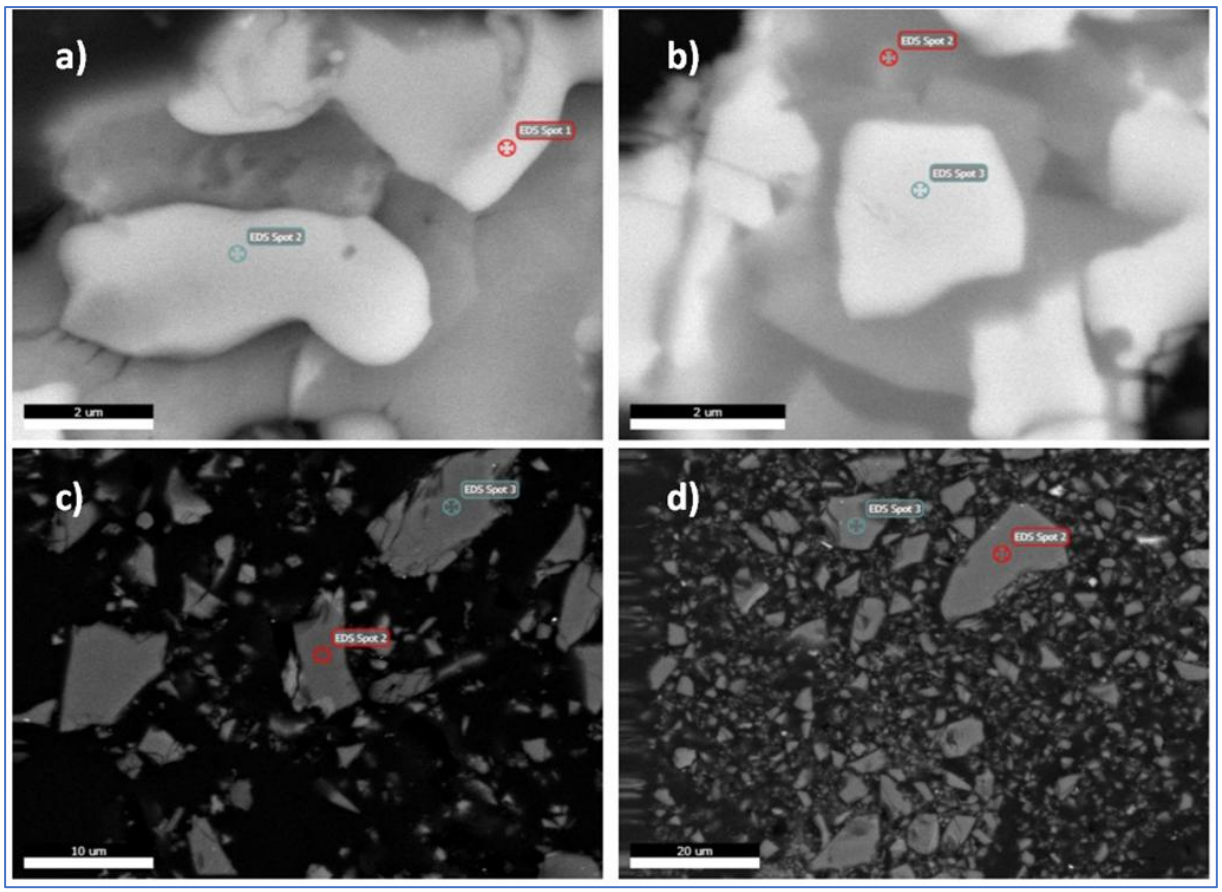

Figure 21: Representative SEM-BSE images of the studied HMWI BASH samples (**a:** sampling fraction of -0.250 mm; **b:** sampling fraction of -1+0.500 mm; **c:** raw sample; **d:** sampling fraction of +8 mm, respectively).

Additionally, the SEM-EDS investigation proved the presence of Fe-Si-particle in the studied material (see: BSE image **c** of **Figure 22**, and the EDS spectrum of **spot 3** in the **Figure A7** in **Appendix**). As it has been proved by QXRD, most probably, it corresponds to fayalite crystalline compound.

Moreover, Cr-Cu-containing rectangular-shaped (sub)-micro-sized Ca-Ti-oxides were also observed (see: BSE image **b** of **Figure 22**, and the EDS spectra of **spots 1 & 2** in the **Figure A6** in **Appendix**; BSE image **d** of **Figure 22**, and the EDS spectrum of **spots 1** in the **Figure A8** in **Appendix**). According to the QXRD data, these particles may correspond to perovskite crystalline compound. The Fe peak can be ascribed to potential Fe-nanoparticles dispersed into the matrix, but not to amorphous. As it has been mentioned above (see: **Chapter 3.2.3**), iron has a strong negative correlation with amorphous matrix.

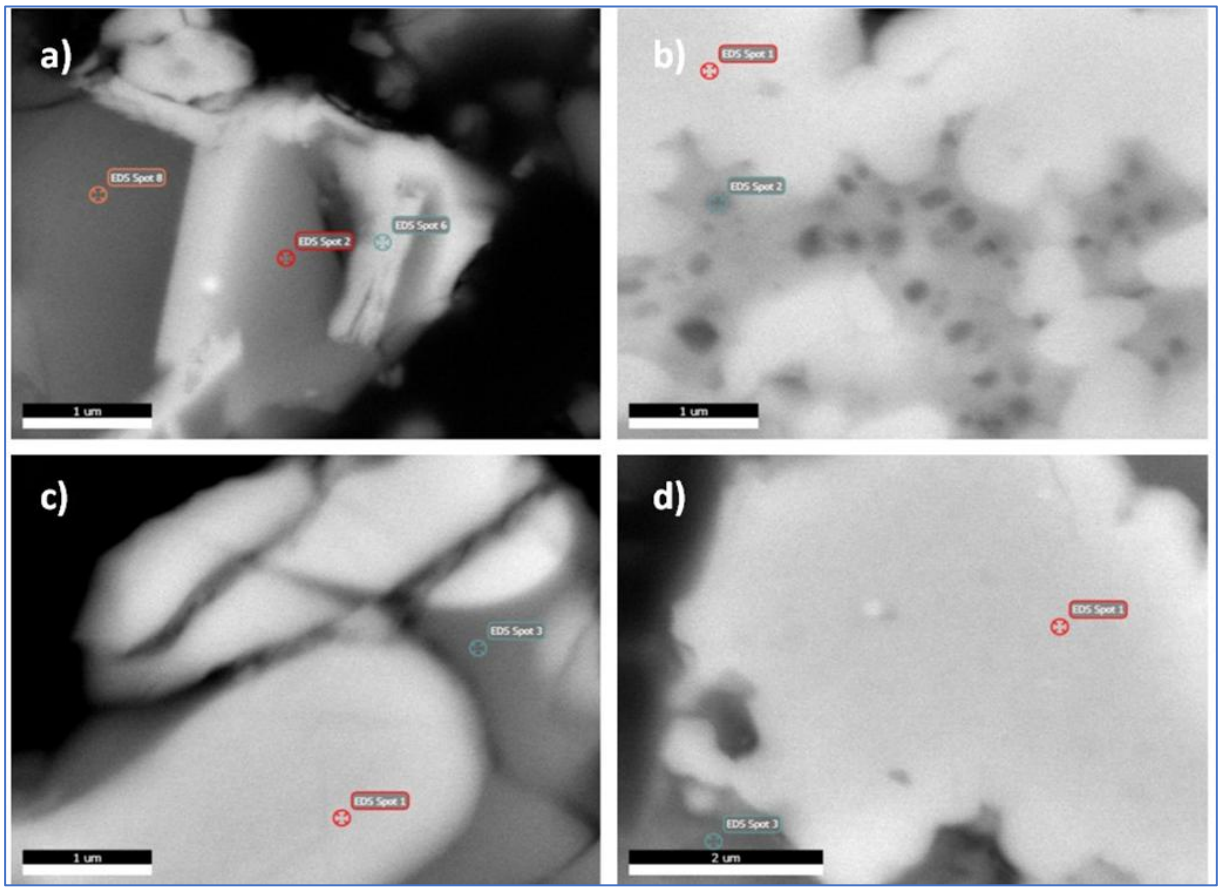

Figure 22: Representative SEM-BSE images of the studied HMWI BASH samples (**a:** sampling fraction of -8+4 mm; **b:** sampling fraction of -2+1 mm; **c:** sampling fraction of -4+2 mm; **d:** sampling fraction of -0.500+0.250 mm, respectively).

Furthermore, the SEM-EDS analysis confirmed the existence of various metals-containing (sub)-micro-sized particles, such as Fe-rich particles (see: BSE image **b** of **Figure 21**, and the EDS spectra of **spot 3** in the **Figure A2** in **Appendix;** BSE image **c** of **Figure 22**, and the EDS spectrum of **spot 1** in the **Figure A7** in **Appendix**) and Cr-containing Si-particles (see: BSE image **a** of **Figure 22**, and the EDS spectra of **spots 2, 6 & 8** in the **Figure A5** in **Appendix**), that might be formed during the incineration process.

It is noteworthy to mention herein, that all the studied microdomains by SEM-BSE observations revealed a similar morphological pattern, i.e., (sub)-micro-sized particles are dispersed into a glassy-like amorphous matrix. Moreover, almost all of the EDS spectra of the probed (sub)-microdomains show a variety of tiny peaks attributed to the presence of specific elements in the studied material. This similarity can be attributed to a relative homogeneous distribution of these metals and metalloids regardless of the size of the HMWI BASH fractions. Such a spectral pattern can be ascribed either to the presence of inclusions and/or to the existence of nano-phases dispersed into the material or, even, due to metal partitioning in the structure of the aforementioned crystals and/or in the matrix. Furthermore, the presence of amorphous and/or poorly crystalline nano-sized phases in the Si-Na-containing amorphous matrix cannot be excluded. Thus, the need for a detailed characterization of the HMWI BASH material at the nanoscale is necessary for understanding the nature of metals that are dispersed into the studied HMWI BASH material throughout its fractions. The e-microscopy of the studied HMWI BASH material, from micro- down to nano-scale, provides insights into the presence of significant heavy metals. However, the applied conventional SEM-EDS did not detect metalloids, so no data exist regarding their specific accumulation. Quantifying the heavy metals and understanding their partitioning are crucial for various valorization pathways. These pathways include utilizing the waste as a supplementary cementitious material (SCM), which must comply with environmental directives concerning leaching properties, or as a secondary source of base and precious metals. For the latter, the distribution of metals is critical for determining the recovery process.

3.4 Milling efficiency & physical properties determination

The studied HMWI BASH raw sample and its specific fractions (-0.500+0.250mm and -0.250mm) were subjected to specific surface area (SSA) measurements using the Blaine test (EN 196-6), particle size distribution (PSD) analysis. Acquired data are crucial in order to control the milling efficiency during mineral processing, when a fineness material used as SCM is desirable for the production of a construction materials (e.g., Khan et al., 2019). The finer the SCM, the better reactivity can be achieved (e.g., Hallet et al., 2020; Elbendari & Ibrahim, 2025). The process of classification, grinding, SSA determination, energy consumption monitoring, and PSD analysis is crucial for comprehensively assessing the physical properties

and homogeneity of the fractions derived from HMWI BASH, facilitating informed decisions regarding their suitability for different applications.

The particle size characteristics of the HMWI BASH raw sample and its corresponding 1:1 mixture of -0.50+0.250mm and -0.250mm fractions, which were used for the production of the autoclaved bricks are presented in the following **Tables 7 & 8**. Milling for 40 minutes in the WIENER 1S ball mill attritor resulted a specific surface area (SSA) of ~8000 cm^2/g in both cases (**Table 7**). The low particle size of both samples is confirmed by the particle size distribution (PSD) measurements, which show that 90% of the material is finer than ~23 μm, 50% is finer than ~7 μm, and 10% is finer than ~1 μm (**Table 8**).

Table 7: Specific surface area (SSA) measurements and the corresponding Blaine test (EN 196-6) results for the HMWI BASH raw sample and its corresponding 1:1 mixture of -0.500+0.250mm and -0.250mm fractions.

Name	Milling time (min)	Material/balls	Energy Consumption (kWh)	Blaine (cm^2/g)
Raw	40	1/6	0.26	7965
Fraction	40	1/6	0.26	8065

The fine particle size and high amorphous content of the studied HMWI BASH samples (see: **Chapter 3.2**) enhance their reactivity, making them suitable as a supplementary cementitious material (SCM) for construction applications. Additionally, the glassy-like structure of the studied HMWI BASH samples promotes energy-efficient milling, achieving fine particle sizes with relatively low milling times, further supporting its potential use in construction materials (e.g., Khan et al., 2019; Whitfield & Mitchell, 2003).

Table 8: Particle size distribution (PSD) results for the HMWI BASH raw sample and its corresponding 1:1 mixture of -0.500+0.250mm and -0.250mm fine fractions.

Name	d10	d50	d90
Raw	1.167	7.446	23.59
Fraction	1.325	7.001	23.76

3.5 Investigation of HMWI BASH-based autoclaved bricks

Two different samples from the studied HMWI BASH material, i.e. the raw sample and the 1:1 mixture of the -0.500+0.250mm and -0.250mm fractions, were utilized toward to the sustainable production of HMWI BASH-based autoclaved bricks ("dense monoliths"). The aforementioned finest fractions were carefully chosen due to their relatively lower amorphous and higher gehlenite content for this purpose. As it has been described in the "Materials and Methods" thoroughly (see: **Chapter 2.9**), particular formulations following three different mix designs were applied for the production of the dense monoliths being cured under certain hydrothermal conditions (**Image 8**) and carbonation (not shown in this thesis). The compressive strength of the autoclaved bricks was measured, while the final products were studied by means of PXRD to investigate the presence of crystalline components affecting their strength. Moreover, according to EN 12457/2 standards, the dense monoliths were subjected to leaching test in order to determine any release of heavy metals to environment (see: **Chapter 2.10**).

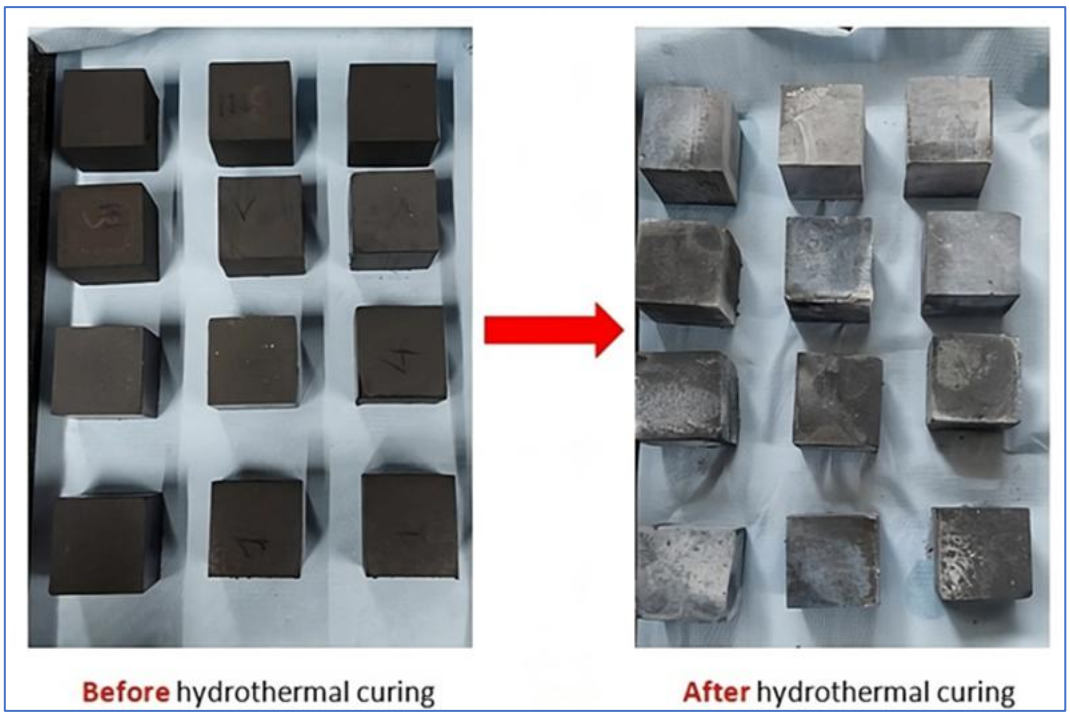

Image 8: Sustainable autoclave bricks before and after hydrothermal curing.

3.5.1 Mechanical properties: Compressive strength test

The compressive strength results of the HMWI BASH-based autoclaved bricks are shown in the **Table 9** and their visualization is presented in the **Figure 23**. Hydrothermal curing proved effective in developing the compressive strength of the monoliths. When the **IP100** and the **IP_MK** mix designs are followed, the dense monoliths that contain the HMWI BASH raw sample ("IP100_R" and "IP_MK_R" formulations, respectively; see: **Figure 23**) demonstrate superior mechanical properties compared to those containing its 1:1 mixture of the finest fractions ("IP100_F" and "IP_MK_F" formulations, respectively; see: **Figure 23**). This is likely due to its higher amorphous content and the presence of more reactive mineral phases such as pseudo-wollastonite and fayalite, whereas the gehlenite content, which is probably inert, was lower (see: **Table 4** and **Figure 6**). Moreover, inorganic polymer (IP) bricks incorporating the raw material exhibit higher strength than those containing OPC ("IP100_R", IP_MK_R", and "BLD_R" formulations, respectively; see: **Figure 23**). Conversely, the IP dense monoliths containing the 1:1 mixture of the HMWI BASH finest fractions ("IP100_F" formulation; see: **Figure 23**) show slightly higher performance compared to the respective blended cement system ("BLD_F" formulation; see: **Figure 23**).

Table 9: The compressive strength (MPa) results of the end products (autoclaved bricks) following specific formulations with respect the utilization of the HMWI BASH raw sample ("RAW") and the 1:1 mixture of its finest fractions ("FRACTION") following the three mix designs (for details see also **Table 2**).

Mix design	Formulation	Maximum Load (MPa)
IP100	IP100_R	74.5
	IP100_F	31.9
IP_MK	IP_MK_R	41.8
	IP_MK_F	19.4
BLD	BLD_R	27.9
	BLD_F	30.3

It seems that the OPC-containing monoliths (BLD mix design) demonstrate significantly lower compressive strength, when they are compared to the IP-based autoclaved bricks. One explanation for the lower strength of BLD-based autoclaved bricks is the insufficient hydration of cement, as the liquid-to-solid (L/S) ratio is limited to 0.175 instead of 0.4-0.5, which is a

typical value for castable mortars. The higher liquid content in castable mortars leads to a paste-like texture that is not suitable for pressing. This reduced hydration results in less formation of hydrated phases such as C-S-H, which are crucial for the mechanical strength of the bricks. Nevertheless, the metakaolin-based dense monoliths containing the 1:1 mixture of the HMWI BASH finest fractions ("IP_MK_F" formulation; see: **Figure 23**) show the lowest compressive strength compared to those from the respective blended cement system ("BLD_F" formulation; see: **Figure 23**).

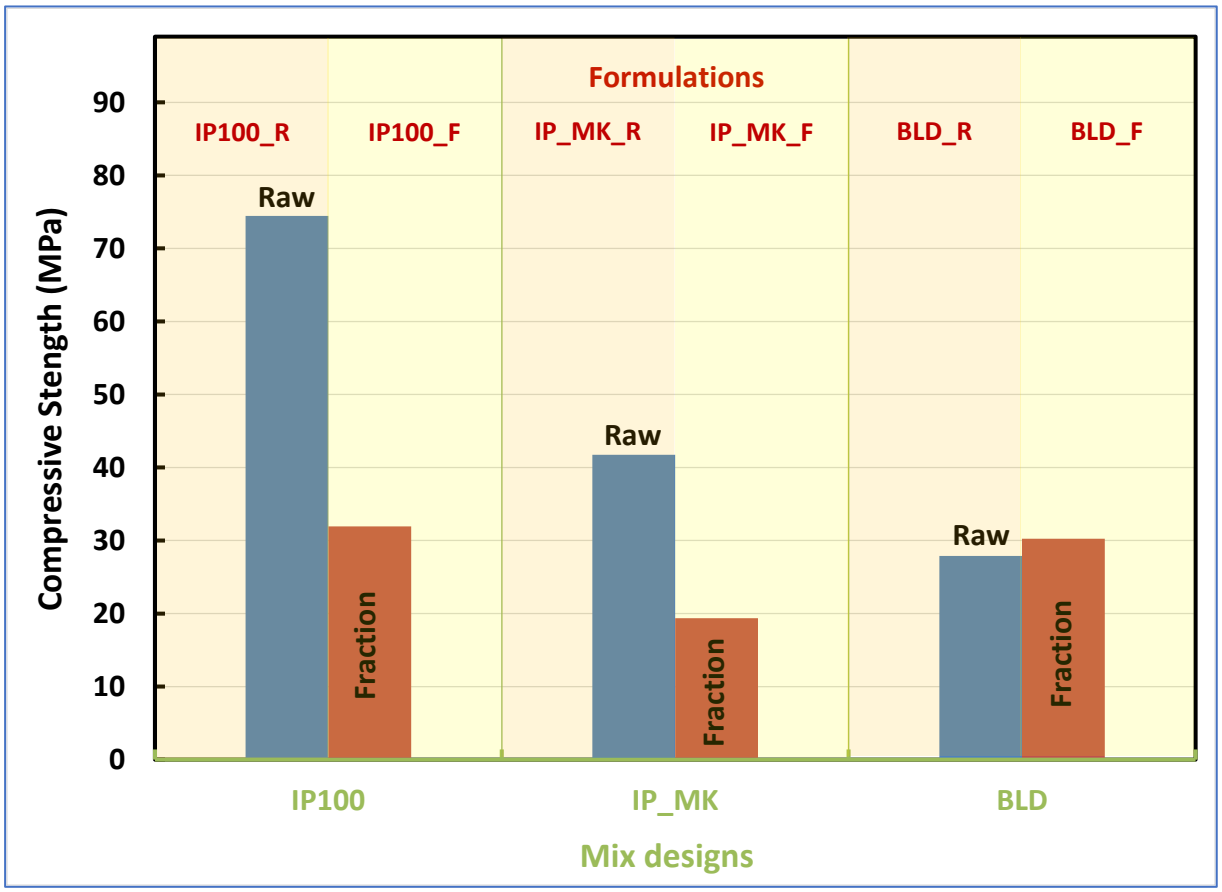

Figure 23: Compressive strength (MPa) of the inorganic polymer (IP) and the blended cement (BLD) mix designs containing the HMWI BASH raw sample ("Raw") and the 1:1 mixture of its finest fractions of -0.500+0.250mm and -0.250mm ("Fraction"). The six formulations used herein are also depicted.

Among the two IP-based recipes (i.e., **IP100** & **IP_MK** mix designs), the addition of metakaolin proved detrimental to the strength of the bricks, making the IP100 mix designs, especially the one corresponding to the IP100_R formulation, the most appropriate choice in terms of both strength and cost as it does not use a commercial product such as the MK. Thus, among the six formulations used in the thesis, the IP100_R have been proved more preferable.

Consequently, the utilization of the finest fractions for the production of autoclaved bricks seems not to be useful. To draw definitive conclusions about the effectiveness of the sieving process and its necessity, the performance of the remaining fractions must be assessed. Furthermore, the addition of the relatively expensive metakaolin (MK) is not recommended in the IP systems, as it compromises strength in both cases. In terms of strength, HMWI BASH incorporated as a sole SCM in an IP system proves more beneficial than adding OPC and MK, leading to a cost-effective and straightforward valorization process.

3.5.2 Characterization of the autoclaved bricks

The investigation of the produced dense monoliths by means of PXRD (see: **Table 10** and **Figures 24-26**) provides insights into the formation of distinct crystalline components between the inorganic polymer (IP) and blended cement (BLD) systems.

Table 10: PXRD results of the end products. The autoclaved bricks have been produced by applying six specific formulations following the three mix designs mentioned above (for details, see also **Table 2**).

Crystalline Compound (%)	Theoretical Chemical Formula	Abbr*[4]	Studied Autoclaved Bricks based on the following formulations:					
			IP100_R	IP100_F	IP_MK_R	IP_MK_F	BLD_R	BLD_F
Quartz *[1]	SiO_2	Q	☑	☑	☑	☑	☑	☑
Calcite *[1]	$CaCO_3$	C	☒	☑	☒	☑	☑	☑
Microcline *[1]	$KAlSi_3O_8$	M	☒	☒	☒	☒	☒	☑
Gehlenite *[1]	$Ca_2Al(AlSi)O_7$	G	☑	☑	☑	☑	☑	☑
ANA-type zeolite *[2]	$NaAlSi_2O_6•H2O$	An	☑	☑	☑	☑	☒	☒
GIS-type zeolite *[3]	$Na_6Si_6Al_{10}O_{32}•12H_2O$	NP	☑	☑	☑	☑	☒	☒
Perovksite *[1]	$CaTiO_3$	P	☒	☑	☒	☑	☒	☑
Tobermorite *[1]	$Ca_5Si_6(O,OH)_{18}•5H_2O$	T	☒	☒	☒	☒	☑	☑

Comments
*[1]: https://rruff.geo.arizona.edu/AMS/amcsd.php
*[2]: corresponding to analcime (Ferraris et al., 1972)
*[3]: corresponding to gismondine-type NaP zeolite (Mimura & Akiba, 1993; Um et al., 2009)
*[4]: Abbreviations

According to PXRD patterns, the two IP systems promoted the formation of sodium aluminum silicate hydrate (N-A-S-H) crystalline compounds corresponding to ANA-type zeolite (analcime / $NaAlSi_2O_6•H_2O$; Ferraris et al., 1972 and references therein; Baerlocher et al. 2016; see: left image of **Figure 24**) and to GIS-type zeolite (zeolite-P) [$(Na_2O,CaO)•Al_2O_3•2SiO_2•4H_2O$; Atkins et al., 1995; Baerlocher et al., 2016; see: right image of **Figure 24**]. According to Atkins et al. (1995), zeolite-P [$(Na_2O,CaO)•Al_2O_3•2SiO_2•4H_2O$)] is the synthetic counterpart of the naturally occurring calcium zeolite, namely gismondine

($Ca_2Al_4Si_4O_{16}•9H_2O$; Fischer, 1963). In line with the literature (e.g., Mimura & Akiba, 1993; Atkins et al., 1995; Um et al., 2009; Hong & Um, 2021 and references therein), it can be assumed that the detected zeolite-P in the IP-based dense monoliths under the hydrothermal curing conditions, can be defined as the high crystalline gismondine-type sodium zeolite P (NaP zeolite / $Na_6Al_6Si_{10}O_{32}•12H_2O$; Mimura & Akiba, 1993; Um et al., 2009). To the best of our knowledge, gismondine-type NaP zeolite has been found in autoclaved bricks by hospital/medical waste incinerated bottom ash, for the first time in the literature. Even though, this synthetic crystalline phase has also been formed during the hydrothermal treatment of coal bottom ash (Um et al., 2009), and additionally been synthesized towards the utilization of coal fly ash (Zhang et al., 2021).

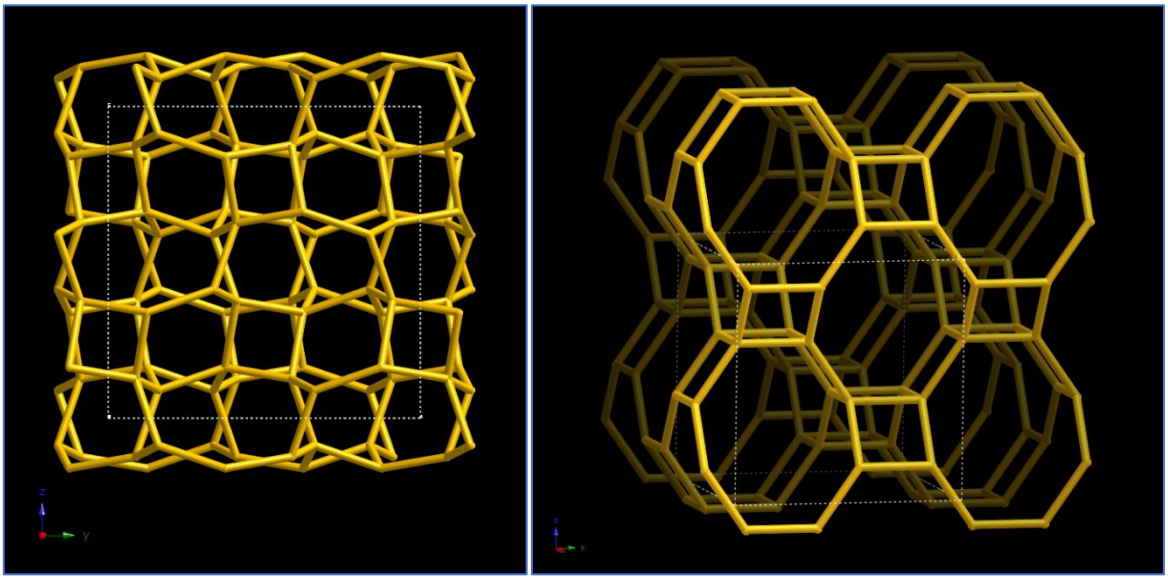

Figure 24: Framework images (viewing direction along [100]) of ANA-type zeolite (*left image*) and GIS-type zeolite (*right image*) by the database that have been approved by the Structure Commission of the International Zeolite Association / IZA-SC (Baerlocher et al. 2016: https://www.iza-structure.org/databases).

The formations of N-A-S-H crystalline compounds might be attributed to the Na-silicate solution used through the applied mix designs (see: **Table 2** above) and the high Si-Al-Na content of the HMWI BASH material (see: **Table 6** above). Moreover, the addition of metakaolin (MK) should act as an additional source of Si and Al, most probably driving to a further crystallization of N-A-S-H phases. As a result, the compressive strength of the IP_MK-based autoclaved bricks should be elevated. On the other hand, the observation of white-colored agglomerates immediately after the addition of MK in the EIRICH EL1 mixer during the mixing process, may indicate insufficient homogeneity of the metakaolin in the final

compressible wet powder (blend), going to be used for the production of the IP_MK-based autoclaved bricks. On these grounds, one can argue that the reduction in the strength in the latter monoliths compared to the IP100-based one (see: **Figure 23**) is a logical consequence of the aforementioned issue, in spite of their identical mineralogy (**Table 10** and **Figs. 25 & 26**).

For the sake of the discussion, it should be stated that zeolites can be both beneficial and detrimental for building materials. On the one hand, zeolites store water in their structures, which is released at later stages of hydration, enhancing the mechanical properties of building materials (e.g., Sezemanas et al., 2013). They can also function as molecular sieves, immobilizing certain potentially hazardous elements (e.g., Erdem et al., 2004). On the other hand, zeolites have low density and high porosity, which is detrimental to compressive strength (e.g., Vogiatzis et al., 2012). Zeolite-type phases were not detected by PXRD in the BLD-based bricks due to the substitution of the alkaline activator with water. Thus, in our case, it seems that N-A-S-H phases plays a constructive role in the compressive strength, especially in the case of the IP100-based dense monoliths that have been made of HMWI BASH raw sample, along with C-A-S-H phases, namely gehlenite.

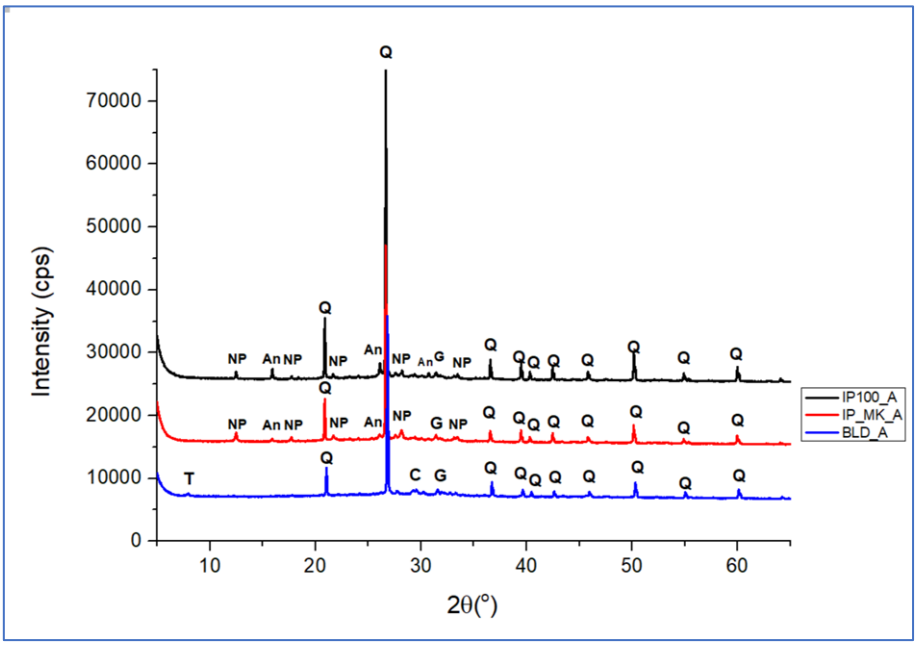

Figure 25: PXRD diagram of the end products (autoclave bricks) based on specific formulations (IP100-based stands for the black PXRD pattern; IP_MK-based bricks stands for the red PXRD pattern; BLD-based bricks stands for the blue PXRD pattern) following the three mix designs (for details see also **Table 2**). The PXRD patterns show the strongest reflections of quartz, calcite, analcime, gehlenite, gismondine-type Na-zeolite P and tobermorite (for the abbreviations, see: **Table 10** above).

Gehlenite and quartz crystalline phases have been detected in all the IP-based and BLD-based dense monoliths, while other crystalline compounds were found in the IP-based bricks, such as perovskite. Quartz is originated from the aggregates (i.e., sand). Gehlenite did not react under hydrothermal conditions, while perovskite was detected by PXRD only in the bricks made of classificated HMWI BASH. Fayalite, pseudo-wollastonite, and corundum were not detected too, implying their reactivity under hydrothermal conditions.

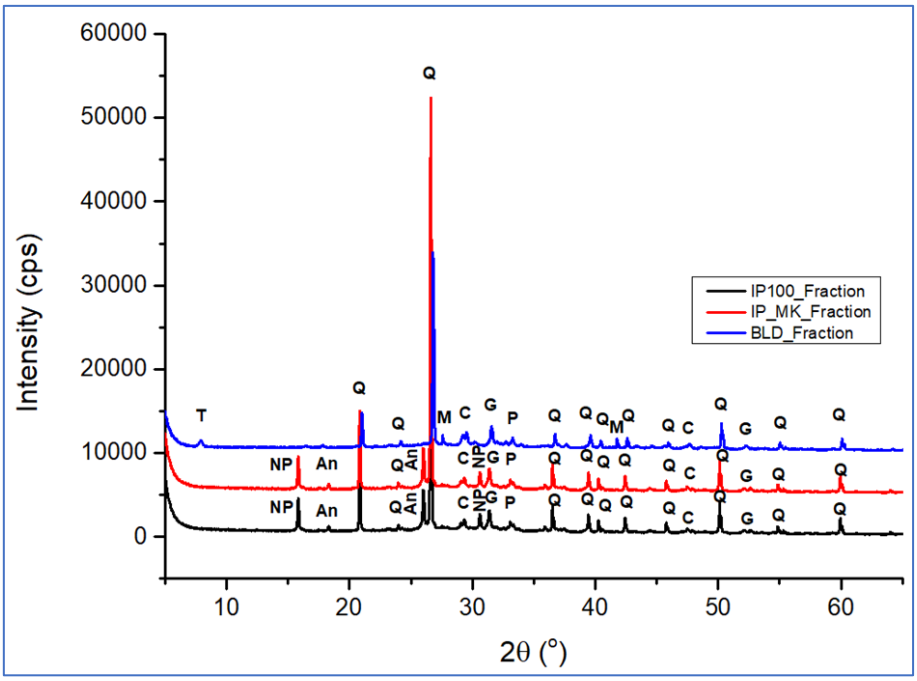

Figure 26: PXRD diagram of the autoclave bricks being produced using the 1:1 mixture of the finest fractions, based on specific formulations (IP100-based stands for the black PXRD pattern; IP_MK-based bricks stands for the red PXRD pattern; BLD-based bricks stands for the blue PXRD pattern) following the three mix designs (for details see also **Table 2**). The PXRD patterns show the strongest reflections of quartz, calcite, analcime, gehlenite, gismondine-type Na-zeolite P, tobermorite and perovskite (for the abbreviations, see: **Table 10** above).

The blended cement monoliths (BLD mix design; see: **Table 2** & **Figure 23**) represent a completely different system compared to inorganic polymers (IP100 and IP_MK mix designs; see: **Table 2** & **Figure 23**). The reaction mechanisms in BLD-based monoliths do not rely on the dissolution of HMWI BASH material through an alkaline activator. Instead, hydration reactions occur among the crystalline phases of ordinary Portland cement (OPC) and water, creating an alkaline environment that leads to the dissolution of the bottom ash (e.g., Arora et al., 2016). Eventually, with the contribution of hydrothermal conditions, calcium silicate hydrate (C-S-H) phases, such as tobermorite ($Ca_5Si_6(O,OH)_{18}•5H_2O$), are formed, expecting to enhance the mechanical properties of these brick (e.g., Chen et al., 2004). Along with the absence of N-A-

S-H phases, the formation of C-S-H phase in the BLD-based bricks only, are both mirrored in the corresponding PXRD patterns (**Figures 25 & 26**). Tobermorite and microcline phases were created after hydrothermal curing and are not found in the IP-based bricks. From the mineralogical point of view, these findings are the main differences between the IP-based and the BLD-based bricks. On these grounds, it can be assumed that the lower strength in the BLD-based bricks can be attributed to absence of zeolites and the presence of tobermorite in the BLD-based bricks. Details in the two blue-colored PXRD patterns of the BLD-based bricks (see blue PXRD patterns in the **Figs. 25 & 26**) revealed a higher relative intensity peak of tobermorite that has been formed in the BLD-based bricks made of HMWI BASH 1:1 mixture of the finest fractions. This indicates an intense crystallinity of that crystalline phase in these kinds of bricks. Possibly the better crystallinity of C-S-H phases influences the properties of the dense monoliths, and thus, enhances their compressive strength as it has been illustrated in the **Figure 23** (e.g., Zhang et al., 2022; Pan et al., 2023). It is well known that tobermorite is a calcium silicate hydrate (C-S-H) binding agent that enhances the compressive strength of various building materials (e.g., Shen et al., 2023 and references therein; Liu et al., 2025 and references therein).

3.5.3 Leachability of autoclaved bricks

According to the EN 12457/2 standards and pH measurements of the leachates, the results of the leaching tests on the autoclaved bricks are shown in the **Tables 11** and **12**, respectively. The limits correspond to hazardous materials that can be discarded in landfills for a non-hazardous waste, making them the strictest available. In spite of the heavy metals and the metalloids contents of the feeding material (see: **Table 6** above) used for the production of the dense monoliths, all the studied autoclaved bricks -that contain both the HMWI BASH raw and its classificated samples- comply with all the leaching limits, except for the bricks that have been made following the IP100_R and IP100_F formulations (see: **Table 2** above). The latter dense monoliths contain antimony and arsenic that both exceed the EN 12457/2 limits by 14% (Sb: 0.8 mg/kg) and 15% (As: 2.3 mg/kg), respectively.

Table 11: The ICP-OES results (in *mg/L*) of the leaching test (EN 12457/2) of the autoclaved bricks.

Analyte Unit	Limits for hazardous waste (EN 12457/2)	Autoclaved Bricks made of HMWI BASH					
		RAW			FRACTION		
		IP100_R	IP_MK_R	BLD_R	IP100_F	IP_MK_F	BLD_F
mg/kg							
Al	-	1.3	3.6	1.4	3.8	1.2	1.0
As	2	1.6	1.4	0.2	2.3	1.5	0.2
Ba	100	8.6	9.0	7.8	9.0	8.4	8.7
Ca	-	2.8	8.2	22.0	12.0	11.0	33.0
Cd	1	*bdl*	*bdl*	*bdl*	*bdl*	*bdl*	*bdl*
Co	-	0.0	0.0	*bdl*	*bdl*	*bdl*	0.1
Cr	10	1.9	1.5	0.5	1.4	0.5	0.8
Cu	50	0.1	0.2	*bdl*	0.1	*bdl*	*bdl*
Fe	-	2.0	4.0	*bdl*	2.0	*bdl*	*bdl*
K	-	1.0	1.3	8.4	3.6	8.2	11.0
Mg	-	5.0	5.2	8.8	5.1	5.6	6.7
Mn	-	*bdl*	*bdl*	*bdl*	*bdl*	*bdl*	*bdl*
Mo	10	1.0	1.3	2.3	1.4	0.4	0.4
Na	-	95.0	75.0	88.0	102.0	67.0	78.0
Ni	10	*bdl*	*bdl*	*bdl*	*bdl*	*bdl*	*bdl*
P	-	11.0	12.0	0.6	8.5	3.6	0.3
Pb	10	*bdl*	*bdl*	*bdl*	*bdl*	*bdl*	*bdl*
S	-	11.0	16.0	47.0	20.0	15.0	31.0
Sb	0.7	0.8	0.3	0.1	0.4	0.5	0.3
Sc	-	*bdl*	*bdl*	*bdl*	*bdl*	*bdl*	*bdl*
Se	0.5	*bdl*	*bdl*	*bdl*	*bdl*	*bdl*	*bdl*
Si	-	97.0	110.0	80.0	100.0	71.0	67.0
Ti	-	0.9	1.2	*bdl*	1.1	*bdl*	*bdl*
V	-	0.3	0.4	0.5	0.7	0.5	0.7
Zn	50	0.3	0.1	*bdl*	0.3	0.0	*bdl*

Note:

*[1]: "*bdl*": below detection limit.

*[2]: **Black** colored text: according to EN 12457/2 the corresponding element has no a significant limit.

*[3]: **Green** colored text: the EN 12457/2 standard recommends a significant limit for particular element(s); the leachate contains the corresponding element(s) below this limit.

*[4]: **Red** colored text: the EN 12457/2 standard recommends a significant limit for particular element(s); the leachate contains the corresponding element(s) above this limit.

The leachates demonstrate a neutral-to-alkaline environment slightly above the EN 12457/2 limit of 6; see: **Table 12**). Such pH may influence the mobilization of heavy metals and the leachability of metalloids, such as Sb and As, that are effectively mobile in acidic environments (e.g., Kiventerä et al. 2018; Cristelo et al. 2020). Heavy metals are effectively immobilized by both the IP-based and the BLD-based formulations. Despite its lower

mechanical performance, the blended cement system is generally more effective at solidifying the included heavy metals. The IP-based formulations may require optimization to be suitable for industrial and commercial applications.

Table 12: The pH results of the leaching test (EN 12457/2) of the autoclaved bricks. Green values stand for the pH values higher than the limit.

pH of leachates	Autoclaved Bricks made of HMWI BASH					
	RAW			FRACTION		
	IP100_R	IP_MK_R	BLD_R	IP100_F	IP_MK_F	BLD_F
1	7.95	7.86	8.8	7.13	7.59	7.11
2	8.01	7.95	8.90	7.22	7.66	6.98
3	8.04	7.76	8.96	7.17	7.70	6.91
Average	8.00	7.85	8.88	7.16	7.65	7.00
Limit (EN 12457/2)	**6.00**	**6.00**	**6.00**	**6.00**	**6.00**	**6.00**

Hydrothermal curing is known for its contribution to the immobilization of heavy metals through zeolitization and formation of C-S-H minerals (e.g., Atkins et al., 1995; Li et al., 2007; Bao et al., 2018; Manickam et al. 2024). The hydrothermal curing of inorganic polymers has been proved beneficial for the stabilization of heavy metals (Luna-Galliano et al., 2011). In this case, hydrothermal curing of both IP100-based and IP_MK-based monoliths proved to be very effective in immobilizing various heavy metals showing high selectivity to Pb, Ni, Cr, Zn and Cu, which are present in high concentrations in the HMWI BASH raw sample. It is known that Ca-Ti-oxides -namely perovskites- may contain a variety of toxic and radionuclide elements (e.g., Gamaletsos et al. 2016), probably contributing to the low leaching of the monoliths. On the other hand, metalloids such as As and Sb are not as effectively immobilized, with As being close or above to the permissible limit for all the IP formulations incorporating the raw and fractionated bottom ash. Antimony follows the same trend with arsenic. Same inferior adsorption capacity of metalloids in IPs was also observed by El-Eswed (2018) and references therein. Heavy metals-rich materials that undergo high temperature processing (e.g., HMWI BASH, metallurgical slags, etc.) tend to form polymetallic structures which are highly leachable. In such a case, the formation of N-A-S-H and C-S-H crystalline phases in IPs adsorb and envelop heavy metals in their crystalline structures, respectively. This might be a

reasonable ground on the assumption that the zeolite-type crystalline compounds trap the aforementioned toxic elements avoiding their intense leakage to environment.

The BLD-based dense monoliths show the best performance in immobilizing potentially toxic elements. Solidification of hazardous waste with OPC is a well-studied technique (Kougemitrou et al., 2011; Anastasiadou et al., 2012; Tsakalou et al., 2018; Suryawan et al., 2019), which proves to be very effective in this case by immobilizing both heavy metals and metalloids (e.g. Paria & Yuer, 2006 and references therein; Niu et al., 2018). Hydrothermal curing of OPC-containing materials leads to the formation of C-S-H phases, such as tobermorite (see: **Table 10**), which envelop heavy metals in their structure, decreasing their leaching capability (e.g., El-Eswed, 2018 and references therein). In this thesis, no N-A-S-H phases -namely zeolite- have been formed (see: **Table 10**), and therefore the adsorption of toxic elements are limited, which is confirmed by the leaching values of the heavy metal and metalloid measurements.

In conclusion, **Table 13** provides a brief summary of the leaching properties of certain materials utilizes HMWI BASH from the literature. The most common approach for solidification and stabilization involves adding high amounts of ordinary Portland cement (OPC), which leads to CO_2 emissions and increases valorization costs. A promising alternative, proposed by Tsakalou et al. (2018), is the co-vitrification of HMWI BASH with silica waste at very high temperatures, though this method results in high energy consumption. Geopolymeric materials could also be used for heavy metal immobilization, but this is effective only for low HMWI BASH content (Tzanakos et al., 2014), otherwise excessive leaching may occur in some cases (Mierzwiński et al., 2018). Comparing the leaching properties of the materials developed in this study, it was found that the heavy metals and metalloids were successfully immobilized in most cases. This was achieved while utilizing limited quantities of OPC and other SCMs for both cementitious and geopolymeric formulations minimizing the production cost.

Table 13: Overview of leaching properties in HMWI-BASH-based materials.

Literature	Application	Processing of HMWI BASH	HMWI BASH content *(wt.%)*	Compliance with leaching test protocols
Cementitious materials incorporating HMWI BASH				
Kougemitrou et al. (2011)	S/S* of HMWI-BA briquettes in cementitious matrices	-	-	Yes (TCLP 1311, EN 12457-01)
Anastasiadou et al. (2012)	Blended cement mortars for S/S*	-	40	Yes (TCLP 1311)
Tsakalou et al. (2018)	Vitrification of HMWI-BA with silica scrap for S/S*	Vitrification at 1300 ^{o}C for 1 h	80	Yes (TCLP 1311, EN 12457-2)
Suryawan et al. (2019)	Blended cement binders for S/S*	-	25	Yes (TCLP 1311)
Geopolymers incorporating HMWI BASH				
Tzanakos et al. (2014)	Geopolymeric matrices for S/S*	Dry milling	≈17 (in the total binder)	Yes (TCLP 1311)
Mierzwiński et al. (2018)	Geopolymeric matrices for S/S*	-	50	High Mo^{2+}, Cl^{-} and SO_4^{2-} mobility (EN 12457-4, EN 15216)

4 CONCLUSIONS

This BSc thesis provides an in-depth approach of the potential valorisation of Hospital Medical Waste Incineration (HMWI) Bottom Ash (BASH) for producing sustainable high-strength autoclaved bricks. The study evaluates the HMWI BASH raw sample and the 1:1 mixture of its finest fractions (-0.500+0.250mm and -0.250mm) as supplementary cementitious materials (SCMs) in brick manufacturing, exploring recipes based on geopolymerization and cementitious systems.

The characterization of the studied HMWI BASH material revealed a high content of a Si-Na-containing amorphous matrix, which decreases in its finer fractions. The QXRD analysis further detected high-temperature phases such as cristobalite (SiO_2), corundum (Al_2O_3), pseudo-wollastonite ($CaSiO_3$), perovskite ($CaTiO_3$) and fayalite ($Fe_2^{2+}SiO_4$). The finer fractions were found to include mainly gehlenite and perovskite, both of which exhibit limited reactivity. Iron-containing crystalline components such as fayalite were not detected in the finest fractions. The LA-ICP-MS along with ICP-OES measurements also indicated high concentrations of several heavy metals (e.g., Cr, Cu, Pb, V, As, etc.), which could pose a potential environmental risk, unless they are immobilized within the monoliths. The SEM-EDS observations revealed the presence of various metals-containing (sub)-micro-sized particles - also containing heavy metals such as Cr and Cu- embedded in a Si-Na-containing amorphous matrix, such as Ca-Ti-oxides (perovskites according to PXRD) and Fe-Si-particles (namely fayalite based on PXRD results), as well as Fe-bearing particles, Cr-containing Si-particles, etc. The presence of amorphous and/or poorly crystalline nano-sized phases in the Si-Na-containing amorphous matrix cannot be excluded. Geochemical interpretation and statistical approach showed that the finest fractions contain elevated Ca, Al, Fe and Ti contents and less Si and Na compared with the raw and the coarser fractions. A strong positive correlation of Si and Na with the amorphous component of the studied samples were revealed, while Ca and Al are inversely proportional to the amorphous. An elevated concentration of metals, such as Ni, Cr, Zn and Cu, have been observed especially in the coarsest and the finest fractions of the HMWI BASH material. Of special interest for future study might be gold. This noble metal have been found to accumulated mostly in the raw and the coarsest fraction, while its

concentration is getting lower towards the finest fractions of the studied material. Finally, the ΣREE content is increased while the grain size is getting smaller.

The valorisation of the studied HMWI BASH material has been performed by applying six (6) formulations following three (3) mix design toward to the production of sustainable pressed autoclaved bricks. The mix designs tested for brick manufacturing were: two different inorganic polymers (IP100 and IP_MK) and one blended cement (BLD). The IP100 mix design incorporated HMWI BASH only and quartz sand as aggregates, and the IP_MK mix design additionally included 10 wt.% of metakaolin, while in the BLD mixture 10 wt.% of OPC was added as binder along with the HMWI BASH. According to the aforementioned formulations a different sample from the HMWI BASH was utilized each time (i.e., the raw sample and the 1:1 mixture of its finest fractions of -0.500+0.250mm and -0.250mm).

Hydrothermal curing led to the dissolution of fayalite, while gehlenite and calcite remained detectable. For the IP-based formulations, sodium aluminum silicate hydrate (N-A-S-H) phases, such as analcime and gismondine-type NaP zeolite were formed, while no calcium silicate hydrate (C-S-H) phases were detected. It is noteworthy to mention that, according to the best to our knowledge, gismondine-type N-A-S-H phase has been observed in autoclaved bricks by HMWI bottom ash, for the first time in the literature. On the other hand, along with the absence of N-A-S-H phases, the formation of C-S-H phase -namely tobermorite- in the BLD-based bricks was observed. Gehlenite was the only calcium aluminum silicate hydrate (C-A-S-H) crystalline compound that was detected in all the studied autoclaved bricks.

In spite of the presence of C-S-H phases, such as tobermorite, in the BLD-based bricks, the mechanical performance of the IP-based monoliths surpassed that of the blended cement recipe, likely due to the insufficient hydration of the OPC, a consequence of the low L/S ratio required for monolith production. Furthermore, the addition of metakaolin in the IP_MK formulation reduced the compressive strength of the IP-based bricks. This could be attributed to potential homogeneity issues in the final blend during the mixing process, explained by the observation of white-colored agglomerates immediately after the addition of metakaolin during the mixing process. Among all the mix designs, the IP-based dense monoliths made of HMWI BASH raw sample were developed an impressive compressive strength of 74.5 MPa. On this ground only, it can be stated that the HMWI BASH raw sample can serve as a viable SCM for brick manufacturing without additional additives. It seems that the presence of N-A-

S-H and C-A-S-H phases dictate the compressive strength. Moreover, the mechanical properties of the bricks that followed the IP_MK_R formulation were notable (compressive strength value of 41.8 MPa). The autoclaved bricks incorporated the mixture of the finest fractions seems to develop a lower compressive strength compared to the IP-based monoliths. This finding drives to the conclusion that the utilization of the finest fractions for the production of autoclaved bricks may not be useful.

The immobilization of potentially heavy metals and metalloids was generally effective, except for the IP100 mix design. The dense monoliths following the IP100_R and IP100_F formulations were found to contain antimony and arsenic that both exceed the EN 12457/2 limits by 14% (Sb: 0.8 mg/kg) and 15% (As: 2.3 mg/kg), respectively. In contrast, the BLD-based bricks showed the best performance in immobilizing potentially toxic elements as the amount of heavy metals and metalloids is ranged within the EN 12457/2 limits. The latter might be attributed to the solidification facilitated by the OPC.

The autoclaved dense monoliths evaluated in this BSc thesis show a potential for construction applications. However, durability tests are necessary to ensure that their mechanical performance remains intact under exposure to natural phenomena and chemically harsh environments. Although the BLD-based monoliths displayed slightly lower strength than their IP-based counterparts, they excelled in immobilizing heavy elements, making them the most promising candidates for construction applications. While IP-based bricks also have a promising potential for construction, a possibility of a leakage of heavy elements requires careful monitoring. Additionally, the zeolites content in the IP-based monoliths, suggests that they could be utilized as purification materials for wastewater and flue gas filtration. Further experimental work is needed to assess their adsorption capacity and suitability for such applications.

5 REFERENCES

Agioutanti, E., Keleş, Ç., Sarver, E. (2019). A thermogravimetric analysis application to determine coal, carbonate, and non-carbonate minerals mass fractions in respirable mine dust. *Journal of Occupational and Environmental Hygiene*, **17(2-3)**, 47-58. DOI: 10.1080/15459624.2019.1695057

Aldawsari, S., Kampmann, R., Harnisch, J., Rohde, C. (2022). Setting time, microstructure, and durability properties of low calcium fly ash/slag geopolymer: a review. *Materials*, **15(3)**, 876. DOI: 10.3390/ma15030876

Ali, A. H., Jalaluddin, N.A., Zulkiflee, N. (2020). The effect of dry mix sodium hydroxide onto workability and compressive strength of geopolymer paste. *International Journal of Integrated Engineering*, **12(9)**, 114-120. DOI: 10.30880/ijie.2020.12.09.014

Alvim-Ferraz, M., Afonso, S.A.V. (2005). Incineration of healthcare wastes: management of atmospheric emissions through waste segregation. *Waste Management*, **25(6)**, 638-648. DOI: 10.1016/j.wasman.2004.07.017

Anastasiadou, K., Christopoulos, K., Mousios, E., Gidarakos, E. (2012). Solidification/stabilization of fly and bottom ash from medical waste incineration facility. *Journal of Hazardous Materials*, **207-208**, 165-170. DOI: 10.1016/j.jhazmat.2011.05.027

Aretxabaleta, X.M., López-Zorrilla, J., Etxebarria, I., Manzano, H. (2023). Multi-step nucleation pathway of c-s-h during cement hydration from atomistic simulations. *Nature Communications*, **14(1)**, 7979. DOI: 10.1038/s41467-023-43500-y

Arora, A., Sant, G., Neithalath, N. (2016). Ternary blends containing slag and interground/blended limestone: Hydration, strength, and pore structure. *Construction and Building Materials*, **102 (1)**, 113-124. DOI: 10.1016/j.conbuildmat.2015.10.179

Atkins, M., Glasser, F.P., Jack, J. (1995). Zeolite p in cements: its potential for immobilizing toxic and radioactive waste species. *Waste Management*, **15(2)**, 127-135. DOI: 10.1016/0956-053X(95)00015-R

Baerlocher, Ch., Brouwer, D., Marler, B., McCusker, L.B. (2016). Database of Zeolite Structures. *https://www.iza-structure.org/databases*

Bakkali, M.E., Bahri, M., Gmouh, S., Jaddi, H., Bakkali, M., Laglaoui, A., Mzibri, M.E. (2013). Characterization of bottom ash from two hospital waste incinerators in rabat, morocco. *Waste Management & Research: The Journal for a Sustainable Circular Economy*, **31(12)**, 1228-1236. DOI: 10.1177/0734242x13507308

Bao, M., Guo, X., Shi, H., Wu, K., Zhang, X. (2018). Utilizing municipal solid waste incineration (MSWI) fly ash as a calcium source to prepare al-substituted tobermorite. *ce/papers*, **2**, 451-456. DOI: 10.1002/cepa.870

Bdour, A., Altrabsheh, B., Hadadin, N., Al-Shareif, M. (2007). Assessment of medical wastes management practice: a case study of the northern part of Jordan. *Waste Management*, **27(6)**, 746-759. DOI: 10.1016/j.wasman.2006.03.004

Berodier, E., Scrivener, K. (2015). Evolution of pore structure in blended systems. *Cement and Concrete Research*, **73**, 25-35. DOI: 10.1016/j.cemconres.2015.02.025

Boesch, M.E., Hellweg, S. (2010). Identifying improvement potentials in cement production with life cycle assessment. *Environmental Science & Technology*, **44(23)**, 9143-9149. DOI: 10.1021/es100771k

Borno, I.B., Haque, M.I., Ashraf, W. (2023). Crystallization of C-S-H and C-A-S-H in artificial seawater at ambient temperature. *Cement and Concrete Research*, **173**, 107292. DOI: 10.1016/j.cemconres.2023.107292

Cai, Q., Li, P., Luo, J., Feng, J., Wu, K., Xu, L. (2023) Production of green autoclaved bricks from waste quarry sludge: Mechanical and microstructural aspects. *Construction and Building Materials*, **401**, 132874. DOI: 10.1016/j.conbuildmat.2023.132874

Chen, J.J., Thomas, J.J., Taylor, H.F.W., Jennings, H.M. (2004). Solubility and structure of calcium silicate hydrate. *Cement and Concrete Research*, **34**, 1499-1519. DOI: 10.1016/j.cemconres.2004.04.034

Çiçek, T., Tanriverdi, M. (2007). Lime based steam autoclaved fly ash bricks. *Construction and Building Materials*, **21(6)**, 1295-1300. DOI: 10.1016/j.conbuildmat.2006.01.005

Cristelo, N., Coelho, J., Oliveira, M., Consoli, N.C., Palomo, A., Fernández-Jiménez, A. (2020). Recycling and application of mine tailings in alkali-activated cements and mortars—strength development and environmental assessment. *Applied Sciences*, **10(6)**, 2084. DOI: 10.3390/app10062084

Djobo, J.N.Y., Tome, S., (2024). Insights into alkali and acid-activated volcanic ash-based materials: A review. *Cement and Concrete Composites*, **152**, 105660. DOI: 10.1016/j.cemconcomp.2024.105660

Doan, D.T., Ghaffarianhoseini, A., Naismith, N., Zhang, T., Tookey, J. (2017). A critical comparison of green building rating systems. *Building and Environment*, **123**, 243-260. DOI: 10.1016/j.buildenv.2017.07.007

Dolenec, M., Šter, K., Borštnar, M., Nagode, K., Ipavec, A., Žibret, L. (2020). Effect of the cooling regime on the mineralogy and reactivity of belite-sulfoaluminate clinkers. *Minerals*, **10(10)**, 910. DOI: 10.3390/min10100910

El-Eswed, B. (2018). Solidification versus adsorption for immobilization of pollutants in geopolymeric materials: A review, in: Ares A.E. (Ed.), Solidification, IntechOpen Limited, London, UK, pp. 77-110, ISBN: 978-953-51-3906-5, eBook ISBN: 978-953-51-4058-0, DOI: 10.5772/intechopen.72299

Erdem, E., Karapınar, N., Donat, R. (2004). The removal of heavy metal cations by natural zeolites. *Journal of Colloid and Interface Science*, **280(2)**, 309-314. DOI: 10.1016/j.jcis.2004.08.028

Elbendari, A.M., Ibrahim, S.S. (2025). Optimizing key parameters for grinding energy efficiency and modeling of particle size distribution in a stirred ball mill. *Scientific Reports*, **15**, 3374. DOI: 10.1038/s41598-025-87229-8

Essam, Y., El-Faramawy, N., Ramadan, W., Ramadan, M. (2023). From dangerous wastes to green construction materials, as thermally stable-radiation blocker, in presence of meso-

porous magnesia and alumina. *Journal of Building Engineering*, **66**, 105896. DOI: 10.1016/j.jobe.2023.105896

European Commission: Directorate-General for Environment. (2020). *2020 Circular Economy Action Plan: international aspects*. Publications Office of the European Union. https://data.europa.eu/doi/10.2779/085517.

Faddegon, B., Ramos-Méndez, J., Schümann, J., McNamara, A., Shin, J., Perl, J., Paganetti, H. (2020). The TOPAS Tool for Particle Simulation, a Monte Carlo Simulation Tool for Physics, Biology and Clinical Research. *Physica Medica*, **72**, 114-121. DOI: 10.1016/j.ejmp.2020.03.019

Galvánková, L., Másilko, J., Solný, T., Štěpánková, E. (2016). Tobermorite synthesis under hydrothermal conditions. *Procedia Engineering*, **151**, 100-107. DOI: 10.1016/j.proeng.2016.07.394

Gamaletsos, P.N., Godelitsas, A., Kasama, T., Kuzmin, A., Lagos, M., Mertzimekis, T.J., Göttlicher, J., Steininger, R., Xanthos, S., Pontikes, Y., Angelopoulos, G.N., Zarkadas, C., Komelkov, A., Tzamos, E., Filippidis, A. (2016). The role of nano-perovskite in the negligible thorium release in seawater from greek bauxite residue (red mud). *Scientific Reports*, **6(1)**, 21737. DOI: 10.1038/srep21737

Gambogi, J. (2013). Rare Earths. USGS Minerals Yearbook – 2011, U.S. Department of the Interior, *U.S. Geological Survey*: Washington, DC, 2013; pp 60.1-60.12.

Gartner, E., Maruyama, I., Chen, J. (2017). A new model for the C-S-H phase formed during the hydration of Portland cements. *Cement and Concrete Research*, **97**, 95-106. DOI: 10.1016/j.cemconres.2017.03.001

Gidarakos, E., Petrantonaki, M., Anastasiadou, K., Schramm, K. (2009). Characterization and hazard evaluation of bottom ash produced from incinerated hospital waste. *Journal of Hazardous Materials*, **172(2-3)**, 935-942. DOI: 10.1016/j.jhazmat.2009.07.080

Griffin, W.L., Powell, W.J., Pearson, N.J., O'Reilly, S.Y. (2008). GLITTER: data reduction software for laser ablation ICP-MS, in Sylvester P, ed., Laser Ablation ICPMS in the Earth Sciences: current Practices and Outstanding Issues, Mineralogical Association of Canada. Short Course Series 40, 308-311.

Guerrieri, M., Sanjayan, J. (2010). Behavior of combined fly ash/slag-based geopolymers when exposed to high temperatures. *Fire and Materials*, **34(4)**, 163-175. DOI: 10.1002/fam.1014

Hallet, V., De Belie, N., Pontikes, Y. (2020). The impact of slag fineness on the reactivity of blended cements with high-volume non-ferrous metallurgy slag. *Construction and Building Materials*, **257**, 119400. DOI: 10.1016/j.conbuildmat.2020.119400

Hanehara, S., Tomosawa, F., Kobayakawa, M., Hwang, K. (2001). Effects of water/powder ratio, mixing ratio of fly ash, and curing temperature on pozzolanic reaction of fly ash in cement paste. *Cement and Concrete Research*, **31(1)**, 31-39. DOI: 10.1016/s0008-8846(00)00441-5

Hartmann, A., Schulenberg, D., Buhl, J. (2015). Investigation of the transition reaction of tobermorite to xonotlite under influence of additives. *Advances in Chemical Engineering and Science*, **05(02)**, 197-214. DOI: 10.4236/aces.2015.52022

He, W., Zhao, J., Yang, G. (2021). Investigation on the role of steel slag powder in blended cement based on quartz powder as reference. *Advances in Civil Engineering*, **2021**, 5547744, DOI: 10.1155/2021/5547744

Hejny, C., Armbruster, T., (2001). Polytypism in xonotlite $Ca_6Si_6O_{17}(OH)_2$. *Zeitschrift fur Kristallographie*, **216**, 396-408. DOI: 10.1524/zkri.216.7.396.20363

Hertel, T., Pontikes, Y. (2020). Geopolymers, inorganic polymers, alkali-activated materials and hybrid binders from bauxite residue (red mud) – putting things in perspective. *Journal of Cleaner Production*, **258**, 120610. DOI: 10.1016/j.jclepro.2020.120610

Hong, S., Um, W. (2021). Top-down synthesis of NaP zeolite from natural zeolite for the higher removal efficiency of Cs, Sr, and Ni. *Minerals*, **11(3)**, 252. DOI: 10.3390/min11030252

Hoornweg, D., Bhada-Tata, P., Kennedy, C. (2013). Environment: Waste production must peak this century. *Nature*, **502**, 615. DOI: 10.1038/502615a

Huijgen, W., Witkamp, G., Comans, R. (2006). Mechanisms of aqueous wollastonite carbonation as a possible CO_2 sequestration process. *Chemical Engineering Science*, **61(13)**, 4242-4251. DOI: 10.1016/j.ces.2006.01.048

Jacobsen, J.C., Rodrigues, M.S., Telling, M.T.F., Beraldo, A.L., Santos, S.F., Aldridge, L.P., Bordallo, H.N. (2013). Nano-scale hydrogen-bond network improves the durability of greener cements. *Scientific Reports*, **3**. 2667. DOI: 10.1038/srep02667

Jasińska, I., Dachowski, R., Jaworska-Wędzińska, M. (2021). Thermal conductivity of sand-lime products modified with foam glass granulate. *Materials*, **14(19)**, 5678. DOI: 10.3390/ma14195678

Javaid, S., Dey, M., Matzke, C., Gupta, S. (2022). Synthesis and characterization of engineered peek-based composites for enhanced tribological and mechanical performance. *Journal of Applied Polymer Science*, **139**. e52886. DOI: 10.1002/app.52886

Jochum, K.P., Nohl, U., Herwig, K., Lammel, E., Stoll, B., Hofmann, A.W., (2007). GeoReM: A New Geochemical Database for Reference Materials and Isotopic Standards. *Geostandards and Research Geoanalytical*, **29(3)**, 333-338. DOI: 10.1111/j.1751-908X.2005.tb00904.x

Karunadasa, K.S.P., Manoratne, C.H., Pitawala, H.M.T.G.A., Rajapakse, R.M.G. (2019). Thermal decomposition of calcium carbonate (calcite polymorph) as examined by in-situ high-temperature X-ray powder diffraction. *Journal of Physics and Chemistry of Solids*, **134**, 21-28. DOI: 10.1016/j.jpcs.2019.05.023

Khan, K., Amin, M.N., Saleem, M.U., Qureshi, H.J., Al-Faiad, M.A., Qadir, M.G. (2019). Effect of fineness of basaltic volcanic ash on pozzolanic reactivity, asr expansion and drying shrinkage of blended cement mortars. *Materials*, **12(16)**, 2603. DOI: 10.3390/ma12162603

Kirchherr, J., Yang, N.N., Schulze-Spüntrup, F., Heerink, M.J., Hartley, K. (2023). Conceptualizing the circular economy (revisited): an analysis of 221 definitions. *Resources, Conservation and Recycling*, **194**, 107001. DOI: 10.1016/j.resconrec.2023.107001

Kiventerä, J., Sreenivasan, H., Cheeseman, C., Kinnunen, P., Illikainen, M. (2018). Immobilization of sulfates and heavy metals in gold mine tailings by sodium silicate and hydrated lime. *Journal of Environmental Chemical Engineering*, **6(5)**, 6530-6536. DOI: 10.1016/j.jece.2018.10.012

Kostrzewa, P., Stępień, A. (2017). Autoclaved sand-lime products with a polypropylene mesh. *IOP Conference Series: Materials Science and Engineering*, **245**, 022069. DOI: 10.1088/1757-899x/245/2/022069

Kougemitrou, I., (2008). Environmental characteristics of ash produced in hospital wastes incinerator. Unpublished BSc Thesis, National & Kapodistrian University of Athens, Athens, Greece, 96 pp. (In Greek)

Kougemitrou, I., Godelitsas, A., Tsabaris, C., Stathopoulos, V., Papandreou, A., Gamaletsos, P., Economou, G., Papadopoulos, D.N. (2011). Characterisation and management of ash produced in the hospital waste incinerator of Athens, Greece. *Journal of Hazardous Materials*, **187(1-3)**, 421-432. DOI: 10.1016/j.jhazmat.2011.01.045

Kriven, W.M., Leonelli, C., Provis, J.L., Boccaccini, A.R., Attwell, C., Ducman, V.S., Ferone, C., Rossignol, S., Luukkonen, T., Van Deventer, J.S.J., Emiliano, J.V., Lombardi, J.E. (2024). Why geopolymers and alkali-activated materials are key components of a sustainable world: a perspective contribution. *Journal of the American Ceramic Society*, **107(8)**, 5159-5177. DOI: 10.1111/jace.19828

Król, M., Rożek, P. (2018). The effect of calcination temperature on metakaolin structure for the synthesis of zeolites. *Clay Minerals*, **53(4)**, 657-663. DOI: 10.1180/clm.2018.49

Kurosawa, M., Shima, K., Ishii, S., Sasa, K. (2017). Trace element analysis of fused whole-rock glasses by Laser Ablation-ICP-MS and PIXE. *Geostandards and Research Geoanalytical*, **30(1)**, 17-30. DOI: 10.1111/j.1751-908X.2006.tb00908.x

Li, F., Li, Q., Zhai, J., Sheng, G. (2007). Effect of zeolitization of CFBC fly ash on immobilization of Cu^{2+}, Pb^{2+}, and Cr^{3+}. *Industrial & Engineering Chemistry Research*, **46(22)**, 7087-7095. DOI: 10.1021/ie070218v

Liu, H., Sun, Z., Rong, J., Wang, J., Ding, Z. (2025). The influence of defects on the mechanical behaviors of tobermorite and C-S-H—A comparative study. *Case Studied in Construction Materials*, **22**, e04417. DOI: 10.1016/j.cscm.2025.e04417

Lu, C., Wang, S., Wang, K., Gao, Y., Zhang, R. (2020). Uncovering the benefits of integrating industrial symbiosis and urban symbiosis targeting a resource-dependent city: A case study of Yongcheng, China. *Journal of Cleaner Production*, **255**, 120210. DOI: 10.1016/j.jclepro.2020.120210

Lu, Y., Li, M. (2019). Solidification of heavy metals in waste incineration fly ashes with silica alumina composite. *Annales De Chimie - Science Des Matériaux*, **43(5)**, 293-298. DOI: 10.18280/acsm.430503

Luhar, S., Cheng, T.-W., Nicolaides, D., Luhar, I., Panias, D., Sakkas, K. (2019). Valorisation of glass waste for development of Geopolymer composites – Mechanical properties and rheological characteristics: A review. *Construction and Building Materials*, **220**, 547-564. DOI: 10.1016/j.conbuildmat.2019.06.041

Luna-Galiano, Y., Fernández-Pereira, C., Vale, J. (2011). Stabilization/solidification of a municipal solid waste incineration residue using fly ash-based geopolymers. *Journal of Hazardous Materials*, **185(1)**, 373-381. DOI: 10.1016/j.jhazmat.2010.08.127

MacArthur, E., Zumwinkel, K., Stuchtey, M.R. (2015). Growth within: A circular economy vision for a competitive Europe, Ellen MacArthur Foundation. Available online: https://www.ellenmacarthurfoundation.org/growth-within-a-circular-economy-vision-for-a-competitive-europe

MacArthur, E. (2014). Towards the circular economy: accelerating the scale-up across global supply chains. Technical Report. World Economic Forum. Available online: https://www.weforum.org/publications/towards-circular-economy-accelerating-scale-across-global-supply-chains

Manickam, C., Chuwongwittaya, A., Jaideekard, M., Thala, M., Kumprom, C., Setthaya, N., Juengsuwattananon, K., Wattanachai, P., Murayama, M., Chindaprasirt, P., Siyasukh, A., Pimraksa, K. (2024). Geopolymer/zeolite-P materials prepared from high-CaO fly ash, biomass ash, and metakaolin using geopolymerization with a hydrothermal process for environmental clean-up. *Construction and Building Materials*, **456**, 139255. DOI: 10.1016/j.conbuildmat.2024.139255

Marchon, D., Flatt, R.J. (2016). Mechanisms of cement hydration. *Science and Technology of Concrete Admixtures*, 129-145. DOI: 10.1016/b978-0-08-100693-1.00008-4

Mariano, A.N., Mariano, A.Jr. (2012). Rare earth mining and exploration in North America. *Elements*, **8**, 369-376. DOI: 10.2113/gselements.8.5.369

Marinkovic, S.R., Trifunović, P., Tokalic, R., Rade Tokalic Matijasevic, S., Kostic-Pulek, A. (2009). DTA/TGA studies of bottom ash from the "Nikola Tesla" power plant from Serbia for the purpose of its utilization in road construction. In: Proceedings of the 36th International Confenence of Slovak Society of Chemical Engineering (SSCHE), 25-29 May 2009, Tatranské Matliare, Slovakia, pp. 094-1–094-8.

Matsimbe, J., Dinka, M., Olukanni, D., Musonda, I. (2022). Geopolymer: a systematic review of methodologies. *Materials*, **15(19)**, 6852. DOI: 10.3390/ma15196852

Ferraris, G., Jones, D.W., Yerkess, J. (1972). A neutron-diffraction study of the crystal structure of analcime, $NaAlSi_2O_6sH_2O$. *Zeitschrift für Kristallographie*, **135**, 240-252. DOI: 10.1524/zkri.1972.135.3-4.240

Merlino, S., Bonaccorsi, E., Armbruster, T. (1999). Tobermorites: Their real structure and order-disorder (OD) character, *American Mineralogist*, **84**, 1613-1621. DOI: 10.2138/am-1999-1015

Merodio-Perea, R.G., Lado-Touriño, I., Páez-Pavón, A., Talayero, C., Galán-Salazar, A., Aït-Salem, O. (2022). Mechanical properties of cement reinforced with pristine and functionalized carbon nanotubes: simulation studies. *Materials*, **15(21)**, 7734. DOI: 10.3390/ma15217734

Miao, J., Zhang, Y., Liang, Y.J., Ran, X., Cheng, M., Jing, Z. (2022). Hydrothermal conversion of model polluted soil into zeolite p to in-situ immobilize heavy metals via zeolitization and its microstructure behavior. *Materials Research Express*, **9(11)**, 115502. DOI: 10.1088/2053-1591/ac9c89

Mierzwiński, D., Łach, M., Mikuła, J., Gołу, M. (2018). Stabilization of ash and slag from combustion of medical waste in the geopolymers matrix. *E3S Web of Conferences*, **44**, 00110. DOI: 10.1051/e3sconf/20184400110

Mimura, H., Akiba, K. (1993). Adsorption Behavior of Cesium and Strontium on Synthetic Zeolite P. *Journal of Nuclear Science and Technology*, **30(5)**, 436-443. DOI: 10.1080/18811248.1993.9734500

Mollaei, S., Ghazijahani, R.B., Farsangi, E.N., Jahani, D. (2022). Investigation of behavior of masonry walls constructed with autoclaved aerated concrete blocks under blast loading. *Applied Sciences*, **12(17)**, 8725. DOI: 10.3390/app12178725

Napp, T.A. Gambhir, A., Hills, T.P., Florin, N., Fennell, P.S. (2014). A review of the technologies, economics and policy instruments for decarbonising energy-intensive manufacturing industries. *Renewable and Sustainable Energy Reviews*, **30**, 616-640. DOI: 10.1016/j.rser.2013.10.036

Narayanan, N., Ramamurthy, K. (2000). Structure and properties of aerated concrete: a review. *Cement and Concrete Composites*, **22(5)**, 321-329. DOI: 10.1016/s0958-9465(00)00016-0

Nedyalkova, L., Lothenbach, B., Geng, G., Mäder, U., Tits, J. (2020). Uptake of iodide by calcium aluminate phases (AFm phases). *Applied Geochemistry*, **116**, 104559. DOI: 10.1016/j.apgeochem.2020.104559

Niu, M., Li, G., Wang, Y., Li, Q., Han, L., Song, Z. (2018). Comparative study of immobilization and mechanical properties of sulfoaluminate cement and ordinary Portland cement with different heavy metals. *Construction and Building Materials*, **193**, 332-343. DOI: 10.1016/j.conbuildmat.2018.10.206

Onisei, S., Lesage, K., Blanpain, B., Pontikes, Y. (2015). Early age microstructural transformations of an inorganic polymer made of fayalite slag. *Journal of the American Ceramic Society*, **98(7)**, 2269-2277. DOI: 10.1111/jace.13548

Owsiak, Z., Kostrzewa, P. (2017). Effects of bentonite additives on autoclaved sand-lime product properties. IOP Conference Series: *Materials Science and Engineering*, **251**, 012021. DOI: 10.1088/1757-899x/251/1/012021

Paixão, G.B., Santos, G.S., Marotta, L.I.M., dos Santos, R.C.V., de Oliveira, C.R., de Oliveira, I.R.B., de Souza, G.S., Soares, P.A. (2023). Ecological bricks: The revolution in sustainable construction. In book: Harmony of Knowledge: Exploring Interdisciplinary Synergie. DOI: 10.56238/sevened2023.006-010

Pan, Y., Jiang, Y., Liu, Z., Xiang, Q., Gao, C., (2023). Effect of Crystallinity on Properties of Autoclaved Aerated Concrete Matrix Materials. *Journal of Physics: Conference Series*, **2437**, 012040. DOI: 10.1088/1742-6596/2437/1/012040

Paria, S., Yuet, P.K. (2006). Solidification-stabilization of organic and inorganic contaminants using Portland cement: a literature review. *Environmental Reviews*, **14(4)**, 217-255. DOI: 10.1139/a06-004

Pontikes, Y., Angelopoulos, G. (2013). Bauxite residue in cement and cementitious applications: current status and a possible way forward. *Resources, Conservation and Recycling*, **73**, 53-63. DOI: 10.1016/j.resconrec.2013.01.005

Provis, J.L., Lukey, G.C., Deventer, J.V. (2005). Do geopolymers actually contain nanocrystalline zeolites? A reexamination of existing results. *Chemistry of Materials*, **17(12)**, 3075-3085. DOI: 10.1021/cm050230i3

Rakhimbaev, S.M., Logvinenko, A., Logvinenko, M. (2020). Mechanism of interaction between concrete cement matrix and mineral additive particles. *Materials Science Forum*, **992**, 98-103. DOI: 10.4028/www.scientific.net/MSF.992.98

Ramadan, M., Habib, A.O., Hazem, M.M., Amin, M.S., Mohsen, A. (2023). Synergetic effects of hydrothermal treatment on the behavior of toxic sludge-modified geopolymer: Immobilization of cerium and lead, textural characteristics, and mechanical efficiency. *Construction and Building Materials*, **367**, 130249. DOI: 10.1016/j.conbuildmat.2022.130249

Ranjbar, N., Kashefi, A., Ye, G., Mehrali, M. (2020). Effects of heat and pressure on hot-pressed geopolymer. *Construction and Building Materials*, **231**, 117106. DOI: 10.1016/j.conbuildmat.2019.117106

Rathore, H.S. (2018). Comparative study of AAC block and brick fully infill buildings and buildings having soft storey at different floor subjected to earthquake: a review. *International Journal for Research in Applied Science and Engineering Technology*, **6(3)**, 1857-1862. DOI: 10.22214/ijraset.2018.3284

Ray, A. (2002). Hydrothermally treated cement-based building materials. past, present, and future. *Pure and Applied Chemistry*, **74(11)**, 2131-2135. DOI: 10.1351/pac200274112131

Rocca, S., Van Zomeren, A., Costa, G., Dijkstra, J.J., Comans, R.N.J., Lombardi F. (2013). Mechanisms contributing to the thermal analysis of waste incineration bottom ash and quantification of different carbon species. *Waste Management*, **33(2)**, 373-381. DOI: 10.1016/j.wasman.2012.11.004

Rossi, L., de Lima, L.M., Sun, Y., Dehn, F., Provis, J., Ye, G., de Schutter, G. (2022). Future perspectives for alkali-activated materials: from existing standards to structural applications. *RILEM Technical Letters*, **7**, 159-177. DOI: 10.21809/rilemtechlett.2022.160

Różycka, A., Kotwica, Ł. (2022). Waste originating from the cleaning of flue gases from the combustion of industrial wastes as a lime partial replacement in autoclaved aerated concrete. *Materials*, **15(7)**, 2576. DOI: 10.3390/ma15072576

Saravanan, G., Ramesh, S.T. (2024). Statistical analysis of seasonal variation in the characteristics of soil like material and refuse derived fuel recovered from landfill mining. *Stochastic Environmental Research and Risk Assessment*, **38**, 127-146. DOI: 10.1007/s00477-023-02569-z

Saravanan, J., Rao, P.V. (2023). Past investigations on development of sustainable bricks – A comprehensive review. *Sustainable Chemistry for the Environment*, **3(23)**, 100030. DOI: 10.1016/j.scenv.2023.100030

Sauvé, S., Bernard, S., Sloan, P. (2016). Environmental sciences, sustainable development and circular economy: alternative concepts for trans-disciplinary research. *Environmental Development*, **17**, 48-56. DOI: 10.1016/j.envdev.2015.09.002

Sezemanas, G., Sinica, M., Zacharčenko, P., Pivenj, N., Mikulskis, D. Kligys, M. (2013). Influence of zeolite additive on the properties of plaster used for external walls from autoclaved aerated concrete. *Materials Science*, **19(2)**, 222-229. DOI: 10.5755/j01.ms.19.2.4441

Shatat, M. A., Ali, G.A.M., Gouda, G.A. (2016). Effect of hydrothermal curing on hydration characteristics of metakaolin–ckd pastes at different temperatures in a closed system. *Beni-Suef University Journal of Basic and Applied Sciences*, **5(4)**, 299-305. DOI: 10.1016/j.bjbas.2016.09.002

Shen, X., Pan, F., Zhang, Q., Lu, J., Liu, X., Ma, Y., Jin, P.,Wang, W., Ran, Q., Hong, J. (2023). Toward the formation mechanism of synthetic calcium silicate hydrate (C-S-H) – pH and kinetic considerations. *Cement and Concrete Research*, **172**, 107248. DOI: 10.1016/j.cemconres.2023.107248

Shi, C., Hu, S., (2003). Cementitious properties of ladle slag fines under autoclave curing conditions. *Cement and Concrete Research*, **33**, 1851-1856. DOI: 10.1016/S0008-8846(03)00211-4

Silva, A., John, M., Stocker, L., Gorissen, L. (2017). From waste to sustainable materials management: three case studies of the transition journey. *Waste Management*, **61**, 547-557. DOI: 10.1016/j.wasman.2016.11.038

Silva, R.V., de Brito, J., Lynn, C.J., Dhir, R.K. (2019). Environmental impacts of the use of bottom ashes from municipal solid waste incineration: A review. *Resources, Conservation & Recycling*, **140**, 23-35. DOI: 10.1016/j.resconrec.2018.09.011

Skibsted, J., Snellings, R. (2019). Reactivity of supplementary cementitious materials (SCMs) in cement blends. *Cement and Concrete Research*, **124**, 105799. DOI: 10.1016/j.cemconres.2019.105799

Sourmelis, S., Pontikes, Y., Myers, R.J., Tennant, M. (2024). Business models for symbiosis between the alumina and cement industries. *Resources, Conservation and Recycling*, **205**, 107560. DOI: 10.1016/j.resconrec.2024.107560

Suryawan, I.W.K., Prajati, G., Afifah, A.S. (2019). Bottom and fly ash treatment of medical waste incinerator from community health centres with solidification/stabilization. In: Proceedings of the 5th International Conference on Engineering, Technology, and Industrial Application (ICETIA) 2018, 12-13 December 2018, Surakarta, Indonesia, AIP Conf. Proc. 2114, 050023. DOI: 10.1063/1.5112467

Tautorat, P., Lalin, B., Schmidt, T.S., Steffen, B. (2023). Directions of innovation for the decarbonization of cement and steel production – a topic modeling-based analysis. *Journal of Cleaner Production*, **407**, 137055. DOI: 10.1016/j.jclepro.2023.137055

Taylor, C. D., Gully, B., Sánchez, A. N., Rode, E., Agarwal, A. (2016). Towards materials sustainability through materials stewardship. *Sustainability***, 8(10)**, 1001. DOI: 10.3390/su8101001

Tsakalou, C., Papamarkou, S., Tsakiridis, P., Bartzas, G., Tsakalakis, K. (2018). Characterization and leachability evaluation of medical wastes incineration fly and bottom ashes and their vitrification outgrowths. *Journal of Environmental Chemical Engineering*, **6(1)**, 367-376. DOI: 10.1016/j.jece.2017.12.012

Tzanakos, K., Mimilidou, A., Anastasiadou, K., Stratakis, A., Gidarakos, E. (2014). Solidification/stabilization of ash from medical waste incineration into geopolymers. *Waste Management*, **34(10)**, 1823-1828. DOI: 10.1016/j.wasman.2014.03.021

Van Achterbergh, E., Ryan, C.G., Jackson, S.E., Griffin, W.L. (2001). Data reduction software for LA-ICP-MS: appendix. In: Sylvester, P.J. (Ed.), Laser Ablation-ICP Mass Spectrometry in the Earth Sciences: Principles and Applications, vol. 29, Ottawa: Mineralogical Association of Canada (MAC) Short Course Series, pp. 239-243.

Vichan, S., Rachan, R., Horpibulsuk, S. (2013). Strength and microstructure development in Bangkok clay stabilized with calcium carbide residue and biomass ash. *ScienceAsia*, **39(2)**, 186. DOI: 10.2306/scienceasia1513-1874.2013.39.186

Vogiatzis, D., Kantiranis, N., Filippidis, A., Tzamos, E., Sikalidis, C. (2012). Hellenic natural zeolite as a replacement of sand in mortar: mineralogy monitoring and evaluation of its influence on mechanical properties. *Geosciences*, **2(4)**, 298-307. DOI: 10.3390/geosciences2040298

Wan-En, O., Yun-Ming, L., Yong, H.C., Li-Ngee, H., Al Bakri Abdullah, M.M., Shee-Ween, O., Sandu, A.V. (2021). Effect of sodium aluminate on the fresh and hardened properties of fly ash-based one-part geopolymer. *Archives of Metallurgy and Materials*, **67(2)**, 441-445. DOI: 10.24425/amm.2022.137775

Walczak, P. (2023). AAC life cycle: How long can autoclaved aerated concrete buildings be used. Ce/Papers, 6(2), 41-45. DOI: 10.1002/cepa.2095

Wang, S., Peng, X., Tang, L., Zeng, L., Lan, C. (2018). Influence of hydrothermal synthesis conditions on the formation of calcium silicate hydrates: from amorphous to crystalline phases. *Journal of Wuhan University of Technology – Materials Science Edition*, **33(5)**, 1150-1158. DOI: 10.1007/s11595-018-1947-0

Wang, Y., Zhu, W., Cheng, J., Zheng, J. (2024). Preparation process and performance study of desert sand autoclaved bricks. *Case Studies in Construction Materials*, **20**, e02838. DOI: 10.1016/j.cscm.2023.e02838

Whitfield, P.S., Mitchell, L. (2003). Quantitative Rietveld analysis of the amorphous content in cements and clinkers. *Journal of Materials Science*, **38(21)**, 4415-4421. DOI: 10.1023/a:1026363906432

Winnefeld, F., Läng, F., Leemann, A. (2023). Pozzolanic reaction of carbonated wollastonite clinker. *Journal of Advanced Concrete Technology*, **21(8)**, 631-642. DOI: 10.3151/jact.21.631

Xiong, X., Yang, Z., Yan, X., Zhang, Y., Dong, S., Li, K., Briseghella, B., Marano, G.C. (2023). Mechanical properties and microstructure of engineered cementitious composites with high volume steel slag and GGBFS. *Construction and Building Materials*, **398**, 132512. DOI: 10.1016/j.conbuildmat.2023.132512

Yadav, S., Mehra, A. (2019). Mathematical modelling and experimental study of carbonation of wollastonite in the aqueous media. *Journal of CO_2 Utilization*, **31**, 181-191. DOI: 10.1016/j.jcou.2019.03.013

Um, N., Han, Gi-C., You, K-S., Ahn, Ji-W. (2009). Immobilization of Pb, Cd and Cr by Synthetic NaP1 Zeolites from Coal Bottom Ash Treated by Density Separation. *Resources Processing*, **56**, 130-137. DOI: https://doi.org/10.4144/RPSJ.56.130

Zepf, V. (2013). Rare earth elements: What and where they are. In Rare Earth Elements: A new approach to the nexus of supply, demand, and use: Exemplified along the use of Neodymium in permanent magnets; Zepf, V., Ed.; Springer Theses; Springer-Verlag, Berlin-Heidelberg, Germany, pp. 11-39.

Zhang, X., Guo, S., Liu, J., Zhang, Z., Song, K., Li, H. (2019). A study on the removal of copper (ii) from aqueous solution using lime sand bricks. *Applied Sciences*, **9(4)**, 670. DOI: 10.3390/app9040670

Zhang, Y., Han, H., Wang, X., Zhang, M., Chen, Y., Zhai, C., Song, H., Deng, J., Sun, J., Zhang, C. (2021). Utilization of NaP zeolite synthesized with different silicon species and $NaAlO_2$ from coal fly ash for the adsorption of Rhodamine B. *Journal of Hazardous Materials*, **415**, 125627. DOI: 10.1016/j.jhazmat.2021.125627

Zhang, Z., Yan, Y., Qu, Z., Geng, G. (2022). Endowing strength to calcium silicate hydrate (C-S-H) powder by high pressure mechanical compaction. *Cement and Concrete Research*, **159**, 106858. DOI: 10.1016/j.cemconres.2022.106858

6 APPENDIX

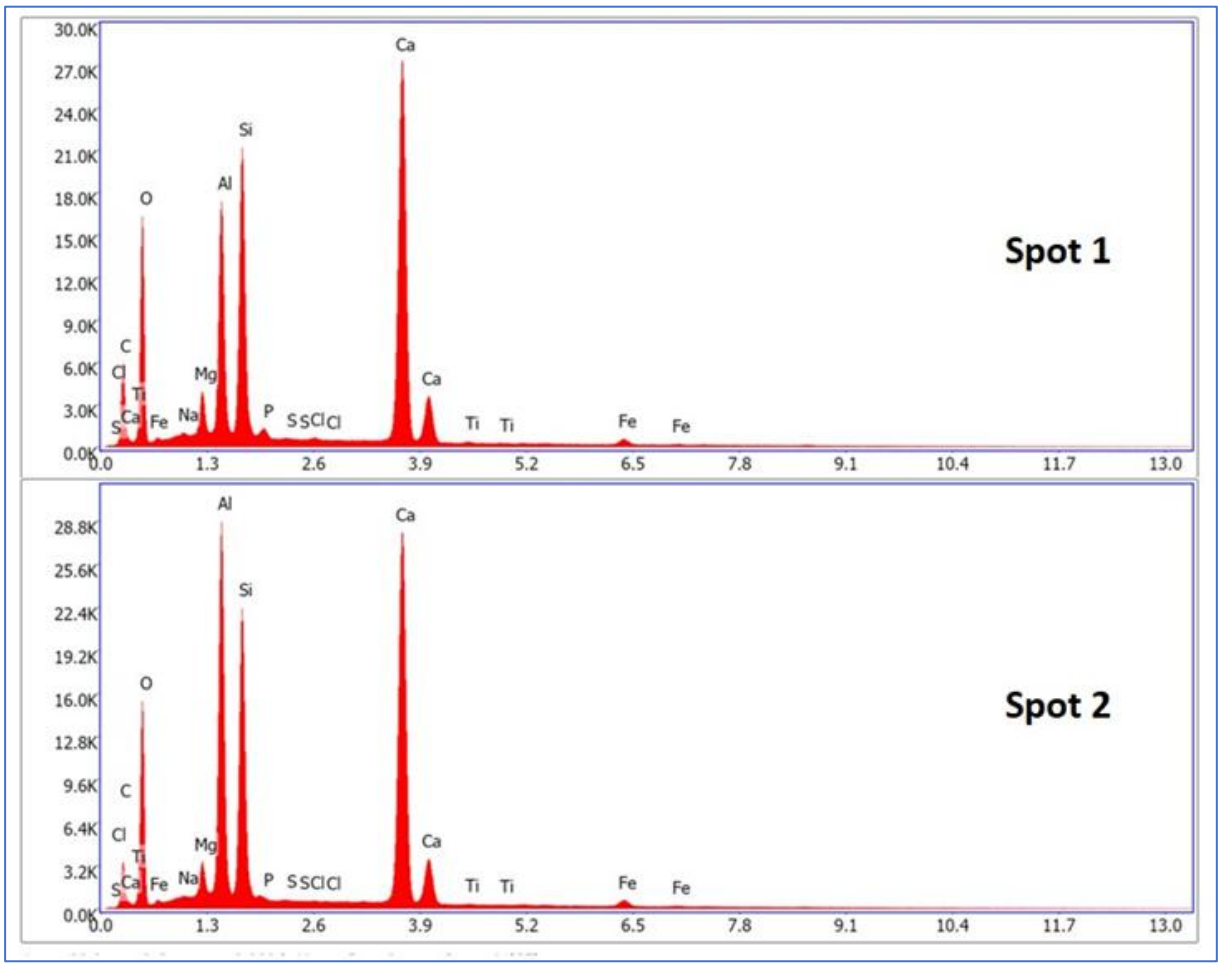

Figure A 1: The EDS spectral results of the -0.250mm fraction (see: BSE image **a** of **Figure 21**).

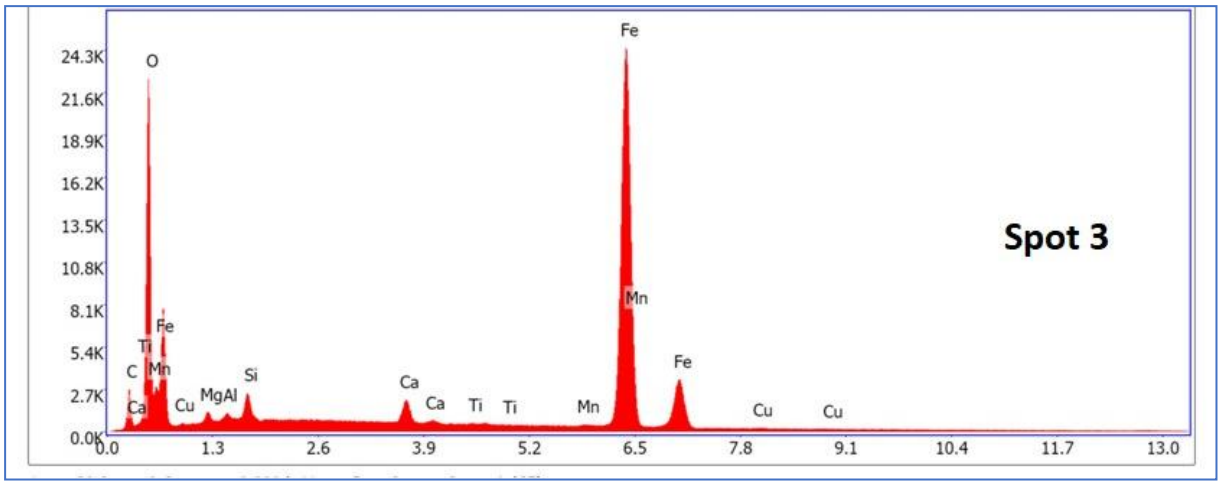

Figure A 2: The EDS spectral result of the -1+0.500mm fraction (see: BSE image **b** of **Figure 21**).

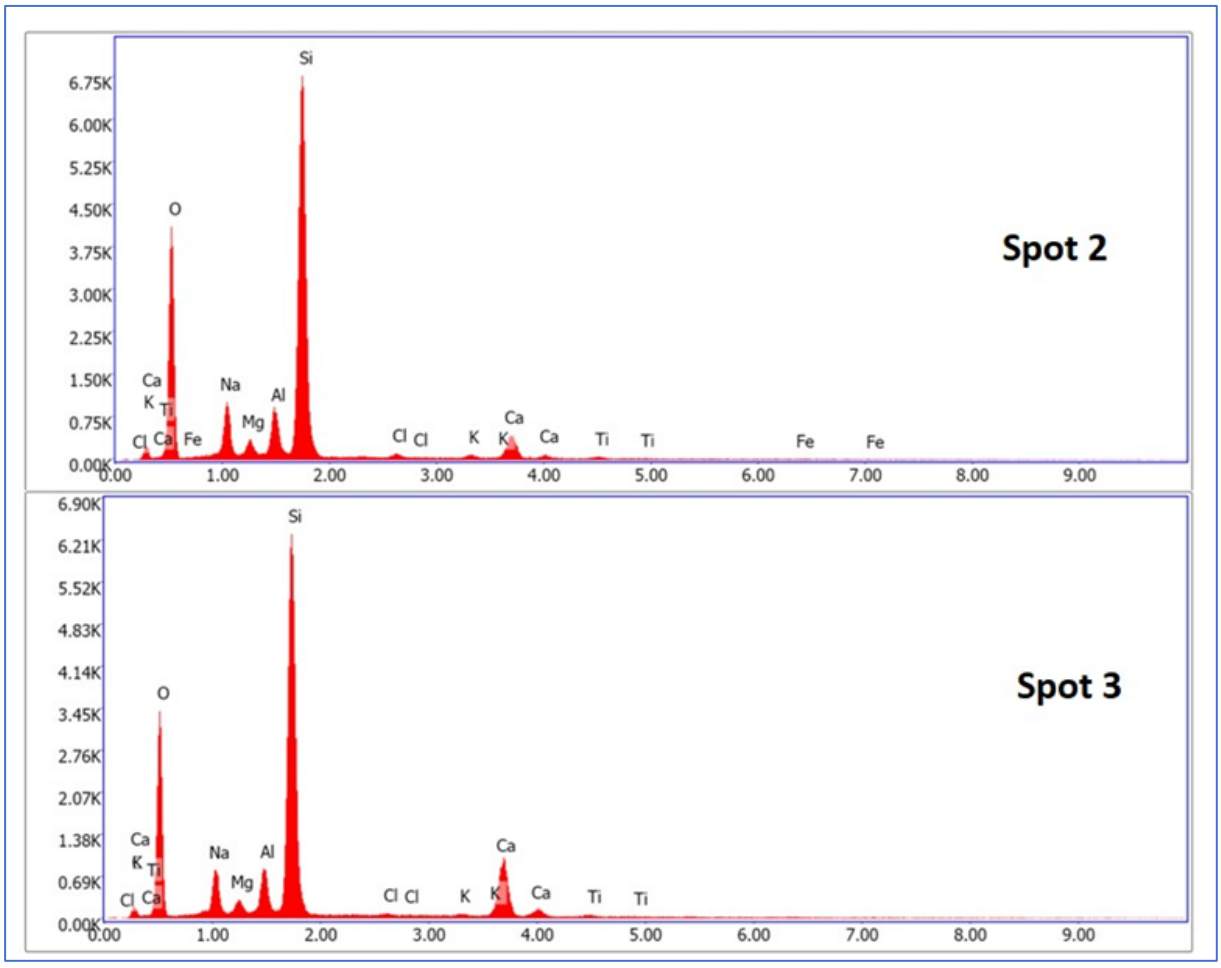

Figure A 3: The EDS spectral results of the raw sample (see: BSE image **c** of **Figure 21**).

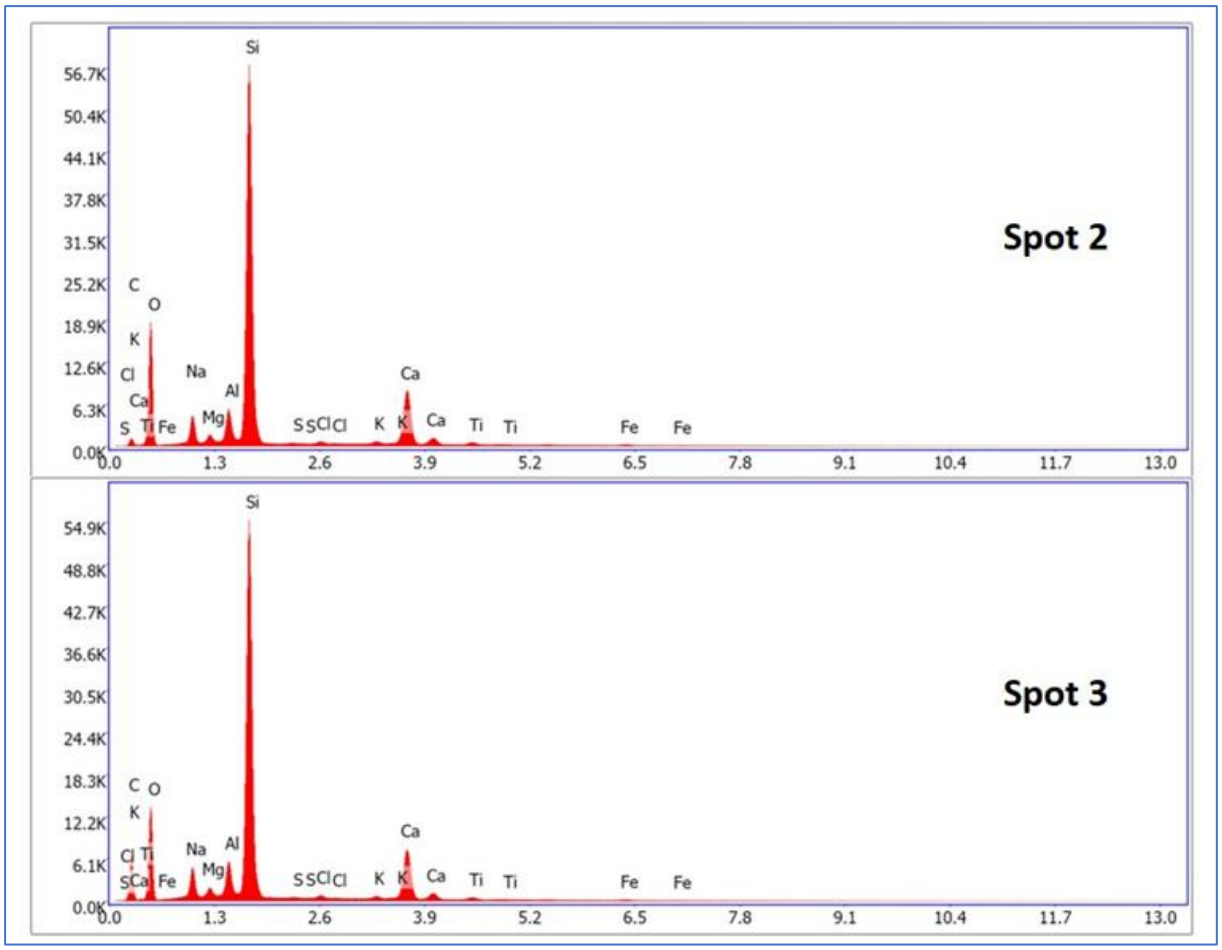

Figure A 4: The EDS spectral results of the +8mm fraction (see: BSE image **d** of **Figure 21**).

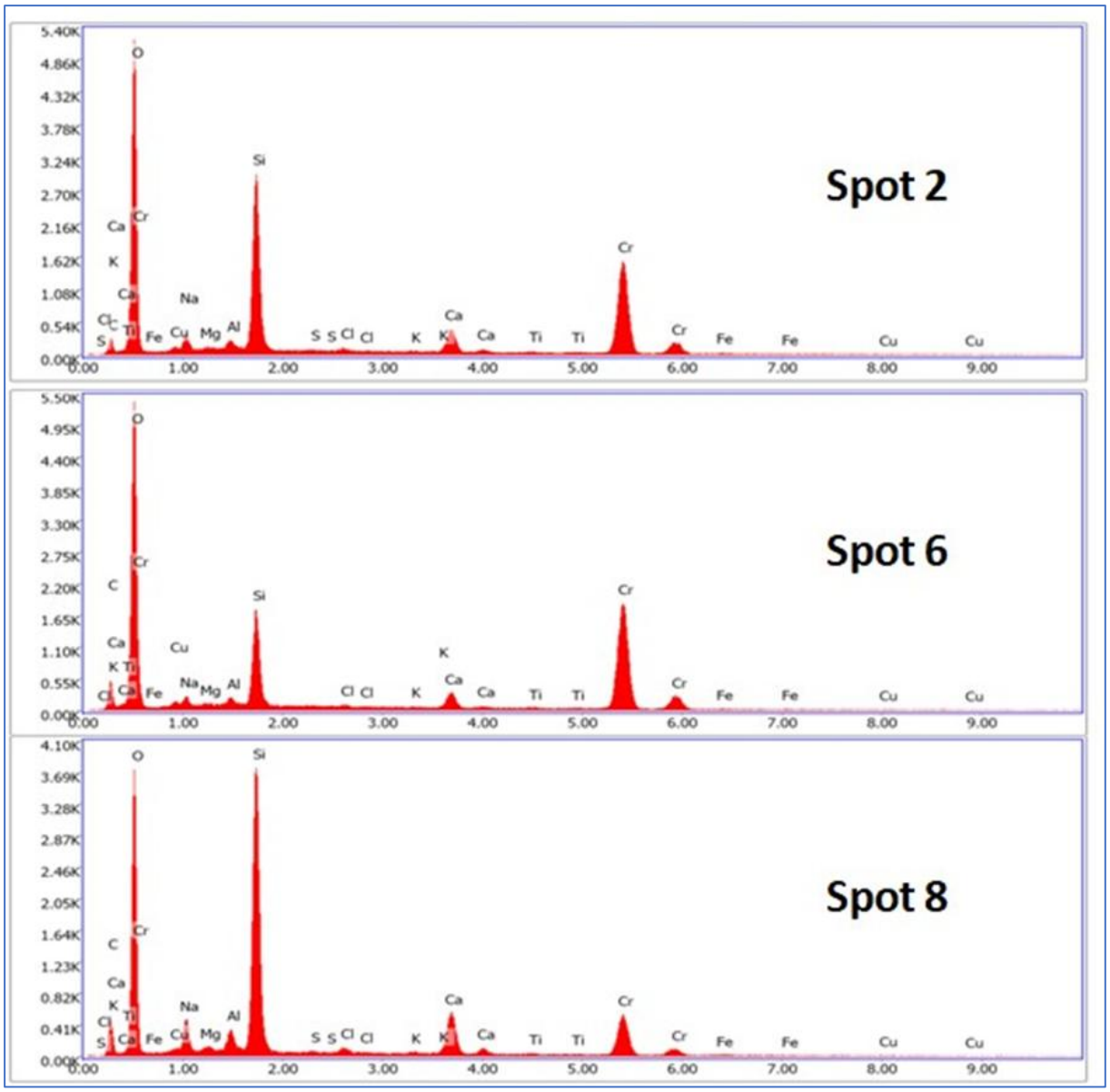

Figure A 5: The EDS spectral results of the -8+4mm fraction (see: BSE image **a** of **Figure 22**).

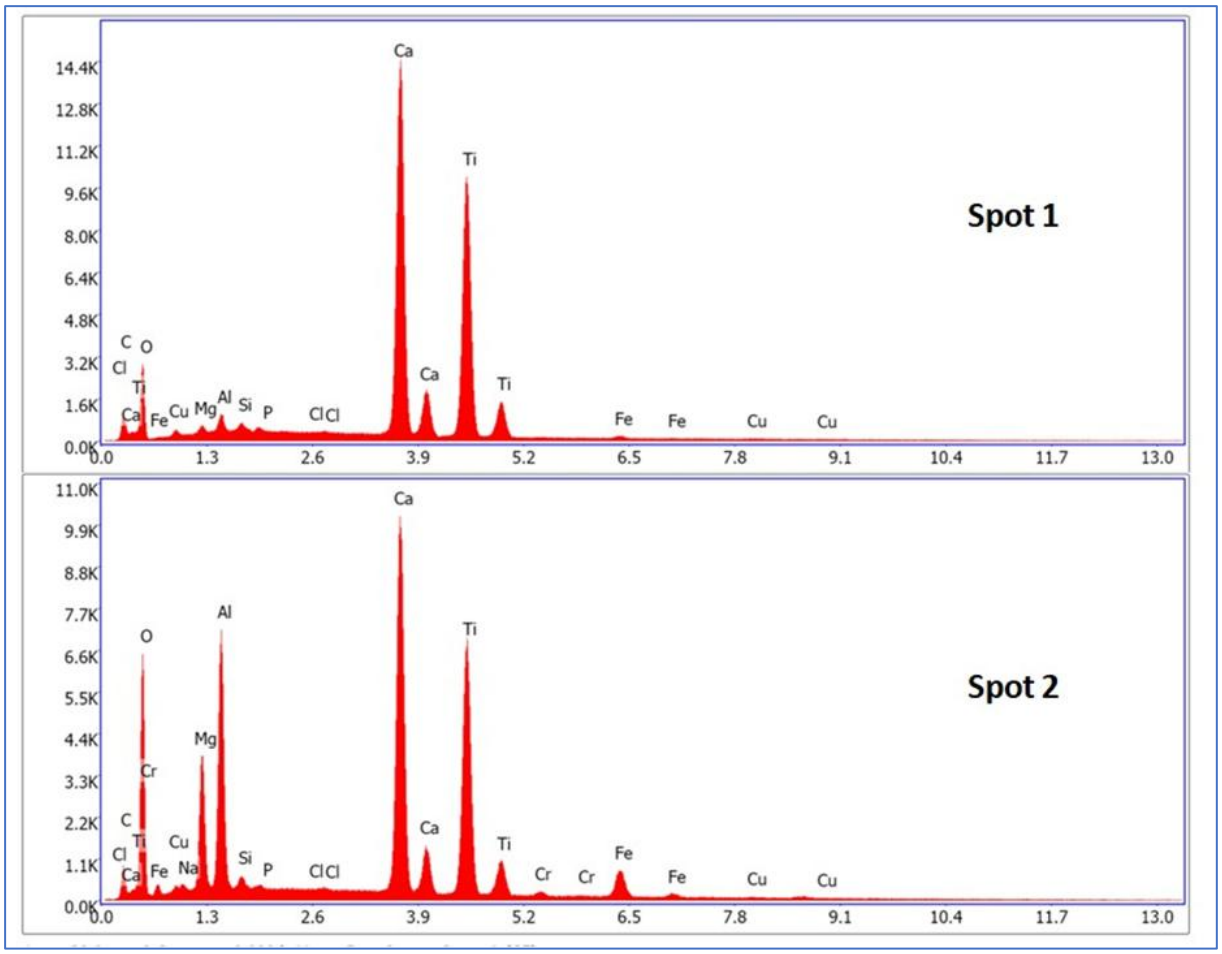

Figure A 6: The EDS spectral results of the -2+1mm fraction (see: BSE image **b** of **Figure 22**)

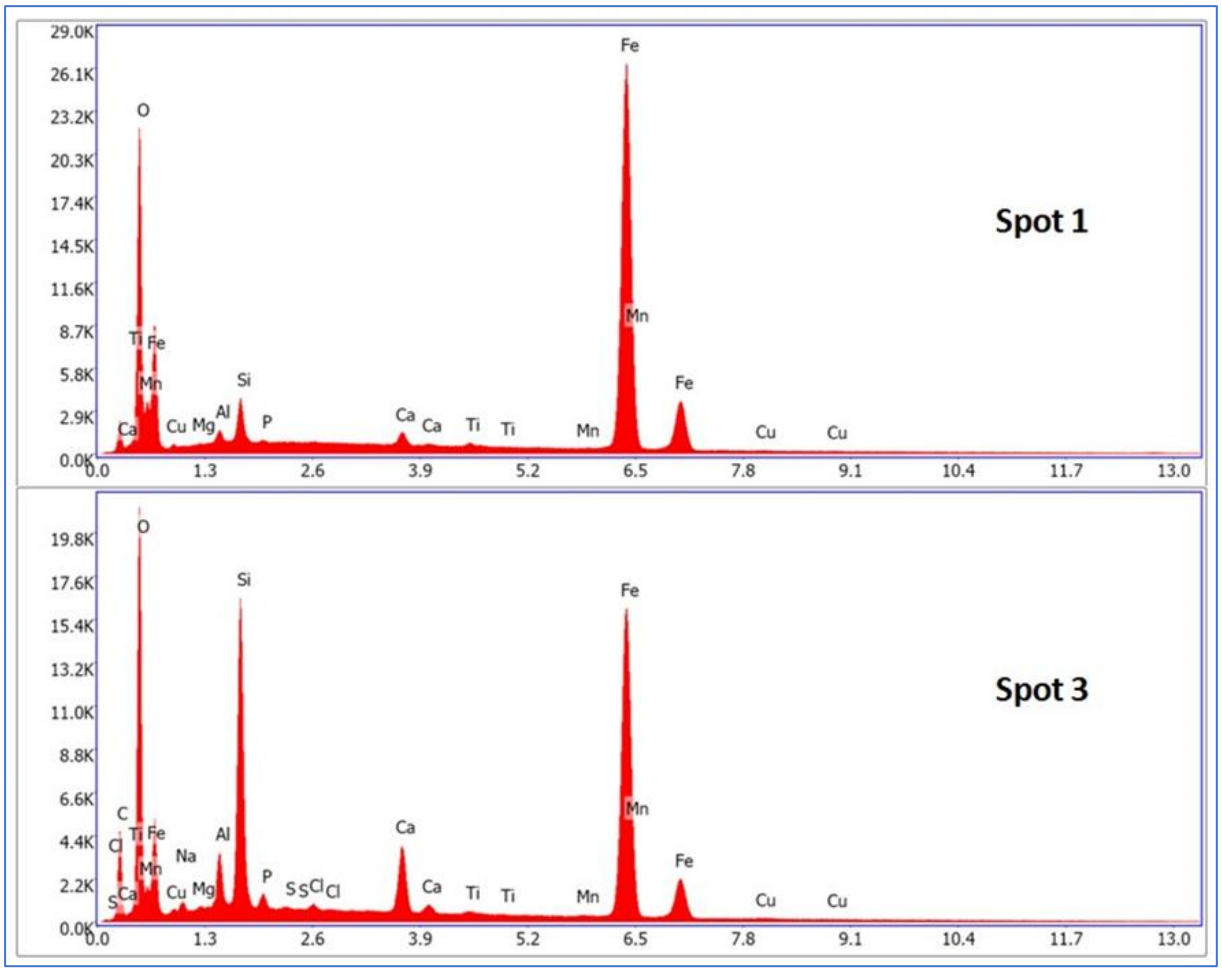

Figure A 7: The EDS spectral results of the -4+2mm fraction (see: BSE image **c** of **Figure 22**).

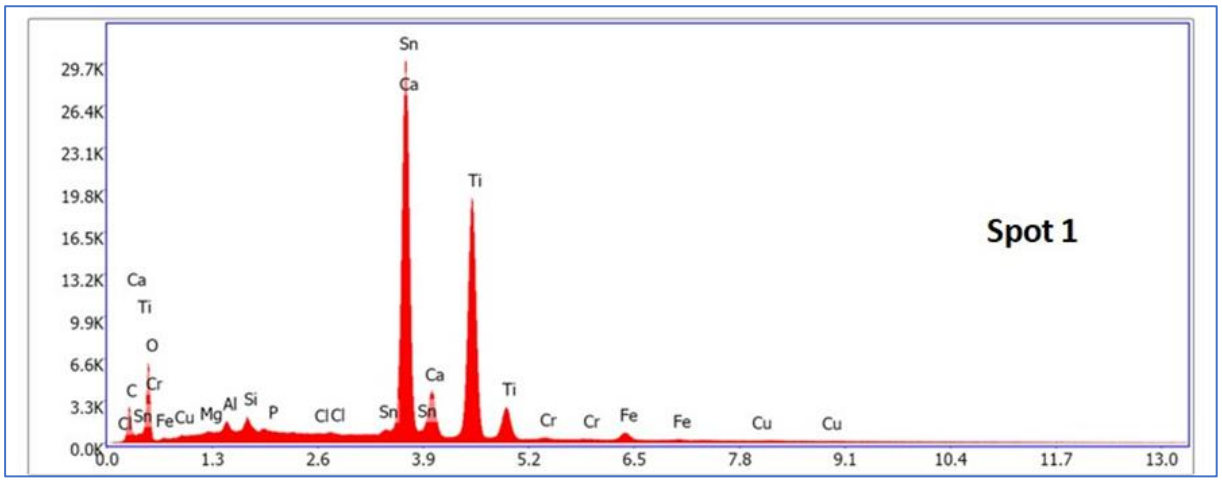

Figure A 8: The EDS spectral result of the -0.500+0.250mm fraction (see: BSE image **d** of **Figure 22**).